The Redistribution of Soil Organic Carbon in Low-gradient Systems Resulting from the Interplay of Aggregate Dynamics and Erosion

A Dissertation Presented for the
Doctor of Philosophy
Degree
The University of Tennessee, Knoxville

Shengnan Zhou
May 2021

DEDICATION

To my parents, Zuxi Zhou and Huilin Song, for your endless love and support!

ACKNOWLEDGEMENTS

I want to express my sincere gratitude to my advisor Prof. Jon Hathaway, for his unconditional support, help, and mentorship at the late stage of my Ph.D. journey. Dr. Hathaway has always been a source of enthusiasm, motivation, and immense knowledge. I would like to thank my former advisor, Dr. Thanos Papanicolaou, for his deep insights, supervision, and guidance that inspired this final product. I would like to thank Dr. Christopher Wilson for his valuable instruction and constant help since the first day I came to UT. I would also like to thank Prof. John Schwartz, Prof. Jie Zhuang, and Prof. Bruce Rhoads for serving on my dissertation committee.

I would like to acknowledge my colleagues Dr. Benjamin Abban, Christos Giannopoulos, Micah Wyssmann, and Matthew Weathers for their help and support with data collection and scholarly discussions related to my research. I would like to thank research undergraduates Andrew Tsay and Matthew Montgomery for assisting with acid digestion. I would like to thank Dr. Andrew Stumpf for his help and support during my field experiments in Goose Creek, Illinois.

I would like to express a special thank you to my parents and my sister for their constant love and support.

Finally, this dissertation was made possible by funding from the CSC China-UT EcoPartnership Scholar program, the NSF Critical Zone Observatory for Intensively Managed Landscape (IMLCZO) program, and the USDA-NRCS Rapid Carbon Assessment (RaCA) program. Any findings, opinions, conclusions, and recommendations expressed in this dissertation are those of the authors and do not necessarily reflect the views of the funding agencies.

ABSTRACT

Soil organic carbon (SOC) is a central indicator of soil quality. SOC spatial distribution is controlled by aggregate breakdown and transport under effects of soil characteristics, rainfall patterns, topography, and management. Capturing the interplay of aggregate dynamics and erosion requires a novel and holistic approach that explores breakdown, formation, and transport mechanisms across scales. The Intensively Managed Landscape Critical Zone Observatory (IMLCZO) in the US Midwest was designed for studies to understand critical zone processes considering glacial and management legacies. Few studies have examined the influence of glacial-remnant topography on aggregate dynamics, which has unknowingly hindered our understanding of SOC redistribution and advancement of soil management.

This study was conducted in two IMLCZO sites to examine SOC variability concerning aggregate turnover and transport influenced by topographies. The SOC variability was compared between Clear Creek (IA), a hilly and well-connected system, and the Upper Sangamon River (IL), a low-relief and poorly-connected system. Focusing on the Upper Sangamon, aggregate turnover following raindrop impact and wetting-drying cycles were tracked using rare earth elements (REE). This was followed by simulated rainfall studies of interrill erosion in field plots with different residues. Finally, aggregate transport distances after rain events were quantified by coupling REE measurements with transport models.

The SOC exhibited low variability in high-gradient landscapes due to enhanced mobilization and mixing under high runoff. The SOC showed high variability in low-gradient landscapes due to local depressions trapping of sediments and suppressed carbon decomposition under anoxic conditions. Aggregate breakdown dominated in early growing seasons due to raindrop impact. After a drying-wetting cycle, more aggregates were formed because of reduced rain power by plants, clay shrinkage upon drying, and microbial flushes upon rewetting. Fine particles accounted for 97% of lost soil and SOC enrichment increased with decreasing soil loss. No-till with high corn residue was most effective in reducing erosion and removing residue from no-till systems caused high soil loss. Small macroaggregates traveled the longest distances (1.33-117 cm) and extra-large macroaggregates traveled the shortest distances (0.97-36 cm). This research expanded knowledge of aggregate breakdown, formation, and transport in agricultural settings and how these processes vary based on local topography, climate, and management.

TABLE OF CONTENTS

LIST OF TABLES

LIST OF FIGURES

LIST OF ACRONYMS

ASI	Aggregate Stability Index
BD	Bulk Density
CCW	Clear Creek Watershed
CV	Coefficient of Variation
DMWD	Dry Mean Weight Diameter
ER_{SOC}	Enrichment Ratio of SOC
ESP	Exchangeable Sodium Percentage
GWC	Gravimetric Water Content
HG	Hillslope Gradient
IDW	Inverse Distance Weighting
IML	Intensively Managed Landscape
PCA	Principal Component Analysis
pdf	Probability Density Function
PLSR	Partial Least Squares Regression
REE	Rare Earth Elements
RPD	Residual Predictive Deviation
SOC	Soil Organic Carbon
USRB	Upper Sangamon River Basin
Vis-NIR	Visible and Near-infrared Spectroscopy

CHAPTER ONE

GENERAL INTRODUCTION

Motivation

In intensively managed landscapes (IMLs), the abundance and distribution of soil organic carbon (SOC) serve as central indicators of soil quality, with implications to crop productivity and agriculture sustainability (Karlen and Stott, 1994). SOC can exhibit high spatial variability across the landscape (Meersmans et al., 2008; VandenBygaart et al., 2007; Xin et al., 2016). Understanding the degree of SOC spatial variability and its driving mechanisms can provide valuable insight for local soil management (e.g., fertilizer application, tillage, irrigation) to sustain soil productivity (Lal, 2006; Vieira and Paz Gonzalez, 2003).

Soil erosion and deposition are key mechanisms that can redistribute large amounts of SOC across landscapes both horizontally and vertically, especially in IMLs (Wilson et al., 2016). These process can result in different degrees of SOC spatial variability (Berhe et al., 2008; Berhe et al., 2007; Fiener et al., 2015). Topography, aggregate dynamics, transport distances, and management dictate the levels of soil erosion and deposition and hence SOC variability.

Topography regulates overland flow processes (Fissore et al., 2017; Stevens et al., 2014) through hillslope gradient (Schwanghart and Jarmer, 2011) and the presence of small depressions (Passalacqua et al., 2015). The hillslope gradient affects the stream power and transport capacity of runoff (Shih and Yang, 2009), translating to variable SOC enrichment. In steep landscapes (i.e., high-energy environments), the stream power and transport capacity are high enough for general movement of all soil size fractions resulting in essentially no SOC enrichment of the eroded sediments compared to the source soil (Liu et al., 2019). In flat landscapes (i.e., low-energy environments), the limited stream power and transport capacity of shallow sheet flow lead to higher SOC enrichment in eroded sediments, and a higher disparity in SOC concentrations in eroded areas versus deposition areas. Geographically isolated depressions that are more prominent in the low-gradient landscapes are sinks of water, fine sediments, and SOC (Cohen et al., 2016). The depressions trap and accumulate SOC and thus can enhance its spatial heterogeneity. Few studies have explored the driving mechanisms behind the different degrees of SOC spatial variability in low-gradient landscapes with topographic depressions and high-gradient landscapes.

Soil aggregates encapsulate and protect varying concentrations and combinations of organic material (Six et al., 2004). In natural environments, soil aggregates are seldom static but continually breakdown and reaggregate. The breakdown of aggregates by raindrop impact (Hogarth et al., 2004; Serio et al., 2019; Shi et al., 2017) or through slacking by runoff liberates SOC that is physically protected within aggregates, making it more susceptible to movement with runoff (Wacha et al., 2018). The subsequent reaggregation of soil fragments due to wetting-drying cycles can conversely stabilize SOC within aggregates (Staricka and Benoit, 1995).

The susceptibility of aggregates to breakdown by raindrop and runoff is usually evaluated through aggregate stability tests (Kemper and Rosenau, 1986). Aggregate stability is an integral property of soil structure that affects not only soil erodibility (Le Bissonnais and Arrouays, 1997; Nciizah and Wakindiki, 2015) but also air diffusivity (Sexstone et al., 1985), water permeability, and carbon storage (Six et al., 2000b). Current studies on aggregate stability focus on steep regions (Hou et al., 2018; Wacha et al., 2018; Wang et al., 2015), where soil erosion by concentrated flow is more pronounced. However, soil erosion can occur even on sufficiently low slopes where rainsplash detachment and shallow flow wash are more prevalent (Proffitt et al., 1991). The effect of rainsplash detachment and shallow sheet flow on SOC redistribution in low-gradient landscapes is far less straightforward. Moreover, few studies have investigated the back-and-forth interactions of aggregate breakdown and reaggregation.

The transport distance of eroded aggregates is another critical variable dictating SOC redistribution over the landscape (Wainwright et al., 2008). Most previous SOC movement studies focus on the bulk soil without investigating the contribution of differently-sized aggregate fractions (Matisoff et al., 2001; Polyakov and Nearing, 2004; Zhang et al., 2018), thus limiting the understanding of SOC redistribution processes over the landscape. Aggregate transport is size-selective due to hydrodynamic sorting of water (Bianchi et al., 2007). High proportions of organic-rich fine materials (e.g., microaggregates) are preferentially removed, with coarser materials (e.g., large aggregates) left behind, resulting in high SOC enrichment in eroded sediments. Therefore, tracking the transport of different aggregate size fractions across the landscape is imperative to fully understand the processes that shape the spatial variability of SOC.

Scope of the Dissertation

This dissertation details a series of studies that characterize the role of topography (i.e., slope gradient and depressions), aggregate dynamics (i.e., breakdown and formation), aggregate transport, and management practices on SOC spatial variability, especially in low-gradient environments. First, the SOC spatial variability in a low-gradient system with topographic depressions (Upper Sangamon River, IL) is examined relative to a steeper system with rolling hills (Clear Creek, IA). Both IMLs are in the glaciated Midwest, and the different glacial histories are what define their topographical make-up. This study uses visible and near-infrared spectroscopy (Vis-NIR) for examining nearly 200 samples in the two systems to identify the effects of hillslope gradient and local depressions on vertical and lateral patterns of SOC. To understand better this variability, we explored the importance of aggregate turnover and subsequent transport (e.g., size-selective transport and transport distance) on SOC redistribution over the low-gradient landscape. Three field experimental studies will then be discussed regarding the breakdown and transport of aggregates in the Upper Sangamon. These sections include the following: (1) tracking aggregate breakdown and reaggregation processes under raindrop impacts and wetting-drying cycles using rare earth elements (REE) tracers in the field conditions assisted with aggregate stability test using simulated rainfall, (2) rainfall simulation experiments for investigating aggregate transport characteristics by surface runoff in terms of particle size selection and SOC enrichment in eroded sediments under different tillage and residue cover treatments, and (3) sediment tracing experiment using REE-labeled aggregates for determining the transport distances of graded aggregate size classes in response to a series of rain events.

This research aims to characterize the role of hillslope gradient and topographic depressions on SOC spatial variability and examine the processes of aggregate turnover and transport to understand better the driving mechanisms of SOC spatial variability. The overarching hypothesis is that soil erosion processes in the low-gradient landscape are dominated by raindrop detachment and shallow flow (low energy) transport, which preferentially remove SOC-enriched finer soil particles at surface and lead to enhanced spatial heterogeneity of SOC across the landscape. Additionally, topographic depressions in the low-gradient landscape could also increase the degree of SOC spatial variability by functioning as sinks of sediment retention and SOC accumulation. We also propose that aggregate breakdown and reformation in field conditions are influenced by rainfall patterns and associated microbial responses to soil moisture variations. Finally, we propose that the nature of transport selectivity could result in variable transport distances for aggregate size classes after rain events.

Literature Review

This chapter provides background material for understanding the trajectory of this research. First, the erosional redistribution of SOC and explanatory factors are explored as an introduction to this research. The importance of topography in soil transport and SOC spatial distribution is then evaluated with particular attention towards low-gradient landscapes with topographic depressions. Third, the hierarchical structure of soil aggregates is presented, followed by a description of aggregate dynamics, including aggregation and breakdown. Finally, the transport of aggregates is discussed, focusing on particle size selectivity of transport, SOC enrichment ratio in eroded sediments, and tracing of sediment movement. In each section, the respective knowledge gaps based on previous studies are identified. In conclusion, the contributions of this research to these knowledge gaps are presented.

SOC Redistribution with Erosion and Deposition

Erosion and deposition redistribute large amounts of soil and associated SOC in agricultural landscapes with cascading effects on system functions (de Nijs and Cammeraat, 2020; Doetterl et al., 2016; Fiener et al., 2015; Kirkels et al., 2014). Rainfall-driven erosion is a three-step process involving detachment, transport, and deposition. Detachment by raindrop impact liberates SOC that is physically protected within soil aggregates (Feller and Beare, 1997). Then, finer and less dense soil particles are preferentially transported by overland flow from eroding areas to depositional areas (Papanicolaou et al., 2015). It is estimated that 70% of eroded topsoil is stored on the landscape in various adjacent depositional topographies, such as floodplains and local depressions (Stallard, 1998). The increased wetness and reduced oxygen in these depositional areas inhibit microbial decomposition of SOC (Berhe, 2006).

Interrill and rill erosion are two significant erosion mechanisms within IMLs (Flanagan and Nearing, 2000; Zachar, 2011). Interrill erosion occurs through soil detachment by raindrop impact, transportation by shallow sheet flow, and delivery to rills (Foster et al., 1985). Low-density SOC is preferentially removed with fine soil particles by low-energy flow, resulting in an enrichment of SOC in the transported sediments (Schiettecatte et al., 2008). Rill erosion removes soil by concentrated flow running through small, ephemeral streamlets or headcuts that function as both sediment source and sediment delivery systems (Govers, 1985; Schiettecatte et al., 2008). The general movement of all size fractions of soil and SOC by rill flow with high energy decreases SOC enrichment in eroded sediments (Wang et al., 2013a).

Factors controlling soil erosion include climate (e.g., rainfall intensity), topography (e.g., slope), soil structure (i.e., soil aggregates), vegetation cover, and human activities (Renard et al., 1991). Topography and soil aggregates play central roles in governing erosional redistribution of SOC. Topography influences flow direction, runoff erosivity, stream power, and soil moisture conditions (Flanagan et al., 2001; Le Bissonnais et al., 2002; Mathier and Roy, 1993) by way of local and integrated hillslope gradients (Roering et al., 2001), landscape positions (Gabbard et al., 1998; Huang et al., 2002), and surface morphologic features such as topographic depressions (Roering et al., 1999). These parameters strongly dictate transport distances of aggregates and the spatial variability of SOC (Chaplot et al., 2009; Yoo et al., 2005). As SOC is embedded within soil aggregates (Six et al., 2001; Six et al., 2000b), the breakdown and transport of aggregates directly control SOC transport and spatial distribution (Liu et al., 2019). In the following sections, the roles of topography, aggregate dynamics, and aggregate transport in SOC redistribution processes are further discussed.

Role of Topography in SOC Redistribution

<u>*Slope Gradient and Curvature*</u>

Slope gradient and curvature (i.e., concave, convex, linear) define the geometry or morphology of hillslopes (Wysocki et al., 2000). The gradient is a proxy of the potential energy that drives mass movement and erosive forces of surface runoff on the slope (Wysocki et al., 2000). Slope shape mainly determines if overland flow is convergent as under concave slopes, divergent as under convex slopes, or straight as under uniform slopes (Agnese et al., 2007).

Ruhe (1960) divided a hillslope profile into five sequential segments, i.e., summit, shoulder, backslope, footslope, and toeslope, which have become standard definitions for guiding landscape segmentation and defining soil/SOC toposequences (Miller and Schaetzl, 2015). The five hillslope positions vary in slope gradient and shape, leading to different degrees of SOC movement (Figure 1-1). The relatively level summit is usually dominated by rainsplash detachment with limited erosional transport. The shoulder has a convex shape and increases in gradient moving down the slope before transitioning to the linear backslope. The shoulder and backslope experience large amounts of soil and SOC loss as the erosive forces of runoff increase. The footslope and toeslope have decreasing slope gradients, reduced transport, and increased deposition of SOC. The SOC distribution across these slope positions has been extensively studied over the past two decades with reported lower SOC at the upper-to-middle slopes and higher SOC at the lower slopes (Berhe et al., 2012; Chaplot et al., 2009; Doetterl et al., 2012; Fiener et al., 2015; Foufoula-Georgiou et al., 2010; Yoo et al., 2005).

Depressions

Topographic depressions are low areas or micro-lows with slopes less than 1%, surrounded by slight rises on all sides, i.e., micro-highs with slopes of 1% to 3% (Wysocki et al., 2000). Thus, they have no natural outlets for surface drainage (Figure 1-2). Depressions are common terrain features present on nearly level to gently sloping landscapes, such as the Upper Sangamon region of Illinois, where the localized depressions are in “saucer” shapes with sizes of 0.2 - 2 acres (USDA, 2004). These depressions function as micro-basins for trapping runoff, eroded sediments, and SOC from surrounding elevated areas (Bertassello et al., 2018; Cohen et al., 2016; Reddy and Patrick, 1975). By increasing surface roughness heterogeneity, these depressions inhibit runoff, thus promoting infiltration and increasing soil moisture (Thompson et al., 2010) leading to regulation of biogeochemical cycles of carbon (Le and Kumar, 2017; Le and Kumar, 2014). Specifically, the elevated wetness induces anoxic conditions that suppress the microbial metabolism of carbon in the depressions (Cohen et al., 2016). As a result, these local pocketed depressions generally contain higher SOC concentration than the surrounding rises.

Knowledge Gaps

Numerous studies have shown the importance of hillslope gradient and slope position on the spatial variability of SOC in moderately to highly sloping landscapes, where rill erosion and SOC transport are enhanced (Papanicolaou et al., 2015; Tu et al., 2018; Xin et al., 2016; Yoo et al., 2006). However, studies of SOC heterogeneity over low-energy landscapes with depressions are scant. Though erosional transport of SOC by concentrated flow is limited in very low-gradient landscapes, SOC transport by rainsplash and shallow sheet flow does occur (Hogarth et al., 2004; Huang et al., 1983; Legout et al., 2005). Moreover, the effect of local depressions on landscape-scale SOC variability has not fully been discussed. Therefore, examining the spatial variability of SOC on low-gradient landscapes with topographic depressions can provide valuable information for improving site-specific soil management that is usually neglected.

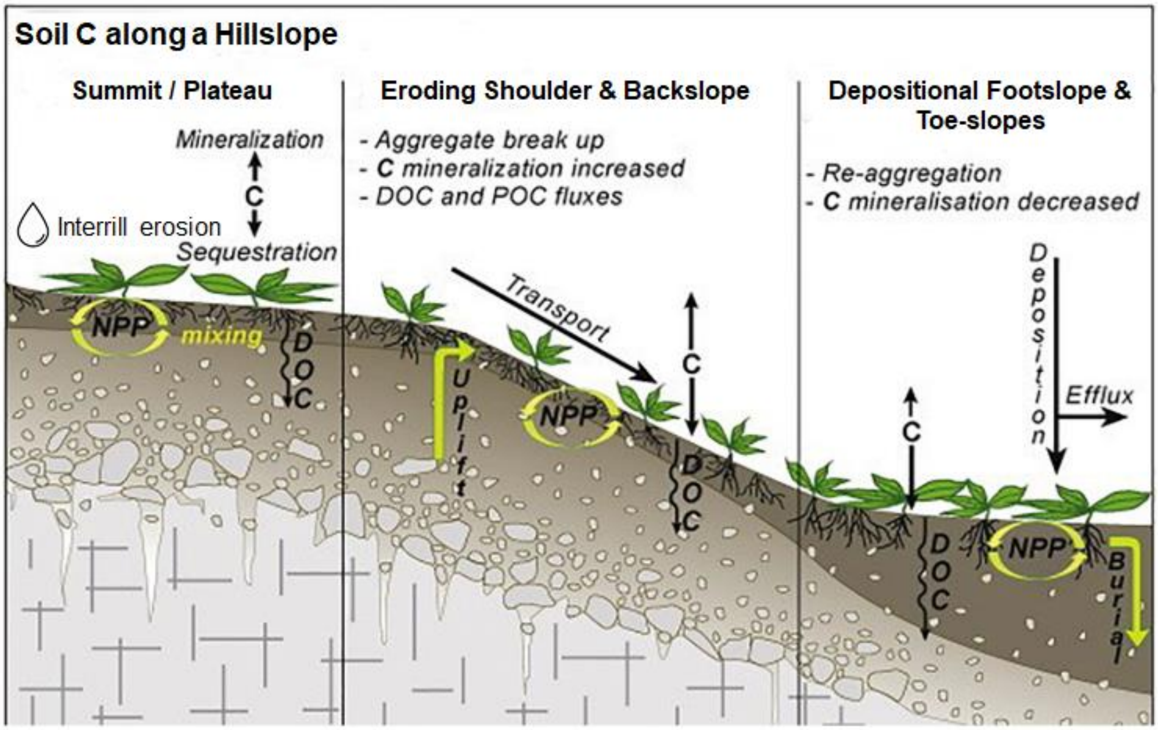

Figure 1-1. Soil C redistribution along a hillslope profile. Detachment, transport, and deposition can occur anywhere along the hillslope, but they are predominantly found at specific hillslope positions (Doetterl et al., 2016).

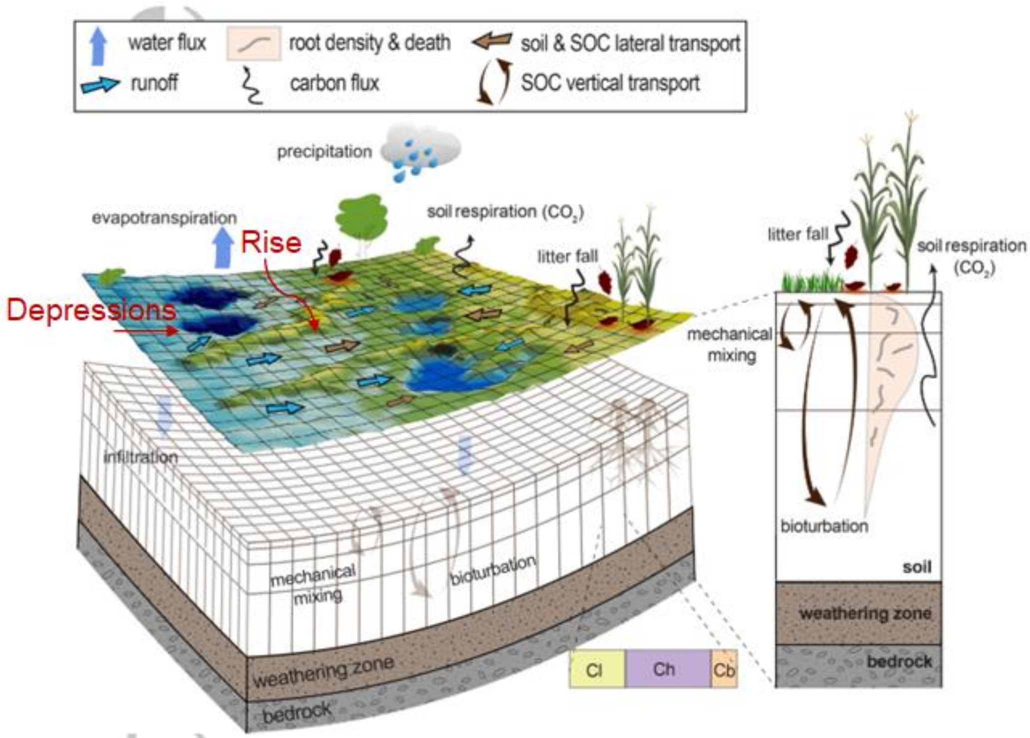

Figure 1-2. SOC dynamics of geomorphological transport and biogeochemical cycles in low-gradient landscapes with topographic depressions. Runoff and eroded sediments are trapped in the local depressions to create SOC hot spots on the land surface (Yan et al., 2019).

Knowledge Gaps

Numerous studies have shown the importance of hillslope gradient and slope position on the spatial variability of SOC in moderately to highly sloping landscapes, where rill erosion and SOC transport are enhanced (Papanicolaou et al., 2015; Tu et al., 2018; Xin et al., 2016; Yoo et al., 2006). However, studies of SOC heterogeneity over low-energy landscapes with depressions are scant. Though erosional transport of SOC by concentrated flow is limited in very low-gradient landscapes, SOC transport by rainsplash and shallow sheet flow does occur (Hogarth et al., 2004; Huang et al., 1983; Legout et al., 2005). Moreover, the effect of local depressions on the landscape-scale SOC variability has not fully been discussed. Therefore, examining the spatial variability of SOC on low-gradient landscapes with topographic depressions can provide valuable information for improving site-specific soil management that is usually neglected.

Aggregate Dynamics

Aggregate Structure

Aggregates are architectural organizations of primary soil particles (i.e., sand, silt, clay) glued together by organic and inorganic cementing agents (Blanco-Canqui and Lal, 2004; Figure 1-3). The bonding forces between the primary particles and cementing agents (e.g., cohesion, cation exchange) are functions of soil mineralogy and origin of the cementing material (e.g., plant, microbe, fauna). They regulate the stability of aggregates against erosive actions of rainfall and runoff and the destructive stress of tillage.

Soil aggregates are usually classified based on their sizes (Tisdall and Oades, 1982). Microaggregates generally range from 0.053-0.250 mm, small macroaggregates are from 0.250-2.00 mm, and large macroaggregates are greater than 2.00 mm. This classification system is widely used in soil science (De Gryze et al., 2006; Márquez et al., 2004; Peng et al., 2017; Six et al., 2000b; Tisdall and Oades, 1982) and is typical for the fertile soils of the Mississippi River Basin, such as Alfisols and Mollisols (Six et al., 2000b; Tisdall, 1991). Within this aggregate hierarchy, microaggregates tend to be more enriched in carbon and more stable to rainfall, runoff, and agricultural practices than macroaggregates (Tisdall and Oades, 1982). Of the macroaggregates classes, small macroaggregates tend to have higher carbon content and stability than large macroaggregates (Hou et al., 2018; Márquez et al., 2004; Six et al., 2000b).

Soil aggregates not only physically protect SOC but also limit air diffusion (e.g., oxygen), regulate water and solute transport, and influence seed germination and plant growth (Braunack and Dexter, 1989a; Braunack and Dexter, 1989b; Dexter, 1988; Horn et al., 1994; Liang et al., 2019; Sexstone et al., 1985). All these properties have profound effects on agroecosystem functions. Thus, aggregate abundance is often used as a metric of soil health (Karlen and Stott, 1994).

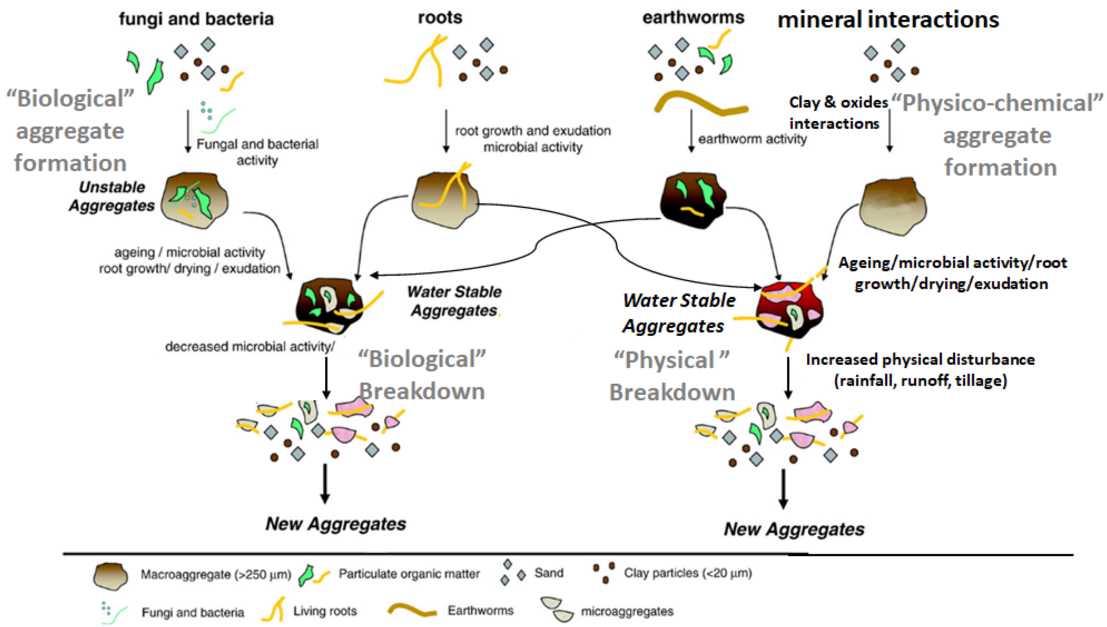

Figure 1-3. Mechanisms of soil aggregation and aggregate breakdown (modified from Barrios, 2007).

Aggregation

Despite their importance to soil health, soil aggregates in natural environments are seldom stable but continuously changing. Aggregate dynamics include aggregation, breakdown, and interactions among different aggregate size classes (Figure 1-3). Understanding these dynamics and their interactions is essential to quantify SOC redistribution and, ultimately, sequestration.

Soil aggregation consists of multiple sequential stages with different binding agents and mechanisms dominating each stage. The aggregation model proposed by Tisdall and Oades (1982) is believed to be the most substantial theoretical framework for understanding aggregation processes. This framework states that primary soil particles, namely free clay and silt (<0.053 mm), are bound together into microaggregates by persistent binding agents, such as resistant aromatic components, polyvalent metal cations (Fe, Al, Ca), and strong organo-metal complexes. The stable microaggregates are further bound together into macroaggregates by transient binding agents, such as microbial- and plant-derived polysaccharides, and by temporal binding agents, such as roots and fungal hyphae. Oades (1984) later postulated that microaggregates could form within macroaggregates when coarse materials are tied together by roots and hyphae. The major factors influencing soil aggregation include soil fauna (e.g., earthworms), soil microorganisms, roots, inorganic binding agents, and environmental variables (Figure 1-3), which are succinctly described by Six et al. (2004). It is evident from the above review that biological-based aggregate formation has been thoroughly studied and well understood. However, physical-based aggregate formation due to freezing-thawing and wetting-drying cycles is largely missing from the literature (Chaney and Swift, 1986; Díaz-Zorita et al., 2002).

Aggregate Breakdown

Aggregate breakdown occurs naturally due to rainsplash and runoff. The general agreement is that rainfall is the dominant contributor to aggregate structure disintegration (Douglas, 1985; Loch and Foley, 1994; Nearing and Bradford, 1985; Nearing et al., 1987). In agriculture fields, tillage is also responsible for aggregate breakdown. However, since tillage breakdown is well studied and relatively straightforward (Álvaro-Fuentes et al., 2008; Elliott, 1986; Zhao et al., 2018), this section will focus on rainfall and runoff breakdown.

When hit by raindrops, soil aggregates experience multiple physical and physiochemical mechanisms before breaking apart (Elliott, 1986; Oades and Waters, 1991; Tisdall and Oades, 1982). There are four main mechanisms (Le Bissonnais, 1996): (1) air slaking during fast wetting; (2) differential swelling and shrinking during wetting-drying cycles; (3) physiochemical dispersion of clay particles while wetting; and (4) mechanical breakdown by raindrop impact (Table 1-1).

Air-slaking refers to the miniature “explosion” in aggregates caused by compression of entrapped air during fast wetting. Air-slaking depends on the volume of trapped air,

Table 1-1. Characteristics of the main mechanisms of aggregate breakdown (Le Bissonnais, 1996).

Mechanism	Slaking	Swelling	Raindrop impact	Dispersion
Type of forces involved	Internal pressure by air during wetting	Internal pressure by clay differential swelling	External pressure by raindrop impact	Internal attractive forces between colloidal particles
Soil properties controlling the mechanism	Porosity, wettability, internal cohesion	Swelling potential, wetting conditions, cohesion	Wet cohesion (clay, organic matter, oxides)	Ionic status, clay mineralogy
Resulting fragments	Microaggregates	Macro and microaggregates	Elementary particles	Elementary particles
Intensity of the disaggregation	Large	Limited	Cumulative	Total

which is in function of aggregate porosity and antecedent moisture content. Coarser aggregates slake easier than finer aggregates because of big pore sizes and more entrapped air during rapid wetting (Sutherland et al., 1996b). Increased antecedent moisture content decreases air slaking because of reduced air and matric potential as the pores are filled with water (Gerard, 1987; Truman et al., 1990). Differential swelling and shrinking during wetting-drying cycles cause microfractures of aggregates. The degree of swelling depends on clay mineralogy & content and wetting rate (Bronswijk, 1991; Tang and Shi, 2011). People are often confused with swelling and slaking, especially when it comes to their interactions with clay. The significant difference between the two is that swelling is positively correlated with clay content while slaking is negatively correlated with clay content (Le Bissonnais, 1996). The dispersion of clay occurs when the cohesive forces between colloidal particles are reduced by water. The dispersion of clay depends on the exchangeable sodium percentage (ESP) of the soil. In fields with high clay content, clay dispersion induces rapid crusting, low hydraulic conductivity, and high particle mobility by water (Ben-Hur et al., 1992). For raindrop breakdown, the raindrop kinetic energy peels off the outer layer of aggregates and produces a high proportion of fine particles that are enriched with SOC.

A notable difference between the four mechanisms is that the former three are driven by internal pressures leading to disintegration from the interior of aggregates. In contrast, the raindrop breakdown is driven by external forces resulting in fragmentation from the exterior of aggregates. Slaking and raindrop peeling are the primary mechanisms responsible for aggregate breakdown. Slaking dominates the aggregate breakdown in relatively dry soil (i.e., the beginning of rainfall) and is particularly strong under high rainfall intensity until field capacity is reached. Afterwards, raindrop impact becomes more prevalent to fragment the prewetted aggregates (Bielders and Grymonprez, 2010; Shi et al., 2017). Swelling and clay dispersion usually have minor effects on aggregate disintegration (Xiao et al., 2018).

The last mechanism for aggregate disintegration is overland flow. It is often considered marginal and presented in a few studies, such as the flume experiments conducted by Wang et al. (2012) and Wang et al. (2013a). During these studies, coarser aggregates rolled as bedload and were rapidly abraded and broken down into smaller fragments. The small pieces were weakly abraded with a reduction in weight and their shape became less angular. Clay particles and smaller aggregates were less impacted by running flow as they traveled as suspended load.

Factors influencing aggregate breakdown include soil properties (Skidmore and Layton, 1992), topographical positions (Pierson and Mulla, 1990), and agricultural management practices (Bronick and Lal, 2005). The soil properties most relevant to aggregate breakdown are texture, clay mineralogy, electrolyte and cations, $CaCO_3$ and gypsum, Fe and Al oxides, organic matter, and water content (Amezketa, 1999). Different combinations of these properties can lead to contradictory results (Le Bissonnais, 1996).

Among these factors, organic matter abundance is frequently reported to be the most crucial predictor of aggregate stability because of its strong capability of holding primary minerals together and ability to hold water, which reduces runoff, aggregate slaking, and dispersion (Annabi et al., 2017; Chappell et al., 1999; Elliott, 1986; Pulleman et al., 2005; Six et al., 2000a; Tisdall and Oades, 1982). Topography affects aggregate stability by regulating overland flow and aggregate transport. Le Bissonnais et al. (2002) and Martz (1992) reported lower aggregate stability in upper slope positions (i.e., eroding zone) and higher aggregate stability in lower slope positions (i.e., depositional zone). However, Wacha et al. (2018) found that aggregate stability decreased downslope along the flowpath. It is well known that conservation tillage or no-till practices confer significant improvements to soil structure, aggregate stability, and SOC storage compared to conventional tillage, which mechanically disintegrates aggregates and causes pore-clogging and SOC loss (Boogar et al., 2014; Cambardella and Elliott, 1994; Sarker et al., 2018; Six et al., 1998; Song et al., 2019; Zhang et al., 2012; Zheng et al., 2018). Wickings et al. (2016) stressed that it is vital to account for topographical heterogeneity when assessing the impact of management practices on aggregate functions as aggregate stability is an outcome of the interactions of these factors and their combined effects should be considered (Annabi et al., 2017; Hoyos and Comerford, 2005; Martz, 1992; Wickings et al., 2016).

Aggregate Stability Measurement

The most widely used method to measure aggregate stability is wet sieving (Wang et al., 2015; Whalen and Chang, 2002). Wet sieving is limited to evaluating aggregate breakdown by slaking and clay dispersion. Another method of analysis involves simulated rainfall to break aggregates (Farres, 1987; Hou et al., 2018; Li et al., 2013; Wacha et al., 2018), which mimics more closely the natural processes of raindrop impact and runoff entrainment seen in IMLs and thus providing more accurate assessments of soil stability and erodibility (Nouwakpo et al., 2018). However, the use of rainfall simulators is not widespread because they are expensive and more labor-intensive when compared to wet sieving.

Breakdown and Aggregation Cycles

The studies presented above have advanced our knowledge regarding aggregate stability. However, they have done little to understand the cyclical interactions (i.e., turnover) of soil aggregation and breakdown. Aggregate turnover regulates the mass transfer between larger aggregates and smaller aggregates. Knowledge about aggregate transfers is essential to further our understanding of SOC mobilization and redistribution over the landscape. Over the past three decades, direct quantification of aggregate structure dynamics has been slowly gaining momentum. De Gryze et al. (2005) added wheat residue to crushed soils followed by short-term incubations. They found that the formation of large water-stable macroaggregates (>2 mm) increased linearly with increasing amounts of residue and respiration rates. Staricka et al. (1992) and Plante et al. (1999) applied inert tracer particles, such as 1-3 mm dysprosium-labeled ceramic spheres, to natural soils and proved that the tracers are robust for practical use to study soil aggregate dynamics. These studies are a step in the right direction of using tracers to track aggregate dynamics, but they are limited since they do not examine the two processes of disruption and formation concomitantly.

The combined tracer and modeling approach proposed by Plante et al. (2002) consisted of a four-pool compartment model where all aggregate size classes were connected through the material flows into and out of the aggregates. The amounts of soil into and out of each aggregate class were determined using a first-order kinetics model. De Gryze et al. (2006) built on this work by mixing rare earth element (REE) powders homogeneously with crushed soil and recombining the soils during incubation periods. A transfer matrix model based on mass conservation was used by De Gryze et al. (2006), improving the first-order linear model by Plante and McGill (2002) to quantify aggregate transfer between any two size classes. Peng et al. (2017) modified De Gryze et al. (2006)'s labeling methods by tagging each aggregate size class with a different type of REE before recombining. Furthermore, Peng et al. (2017) expanded the transfer matrix model for directly enumerating the change in the proportion of aggregates during the breakdown and buildup processes.

Knowledge Gaps

These studies of aggregate dynamics, achieved through incubation experiments, are predicated on assumptions that (1) biological processes (e.g., microbes) are the only factors driving aggregate breakdown and buildup, and (2) soil aggregates do not move across space. However, this is not the case in nature as (1) the physical forces of raindrop impact and runoff also cause aggregate breakdown and aggregation over a short time scale, resulting in mass transfer physically between larger aggregates and smaller aggregates, and (2) soil aggregates could be translocated by rainsplash and runoff. Quantification of the physical turnover of aggregates under natural conditions is a leap to fill in the research gaps.

Aggregate Transport

Selective Enrichment of SOC

The aggregate size distribution of eroded sediments has been widely observed to be finer than in-situ soil due to the selective removal of smaller aggregates and silt/clay by raindrops and runoff (Liu et al., 2019; Massey and Jackson, 1952). Moreover, the transport of loose aggregates is usually associated with sediment sorting, where coarse particles deposit first due to higher settling velocity and finer particles travel further owing to lower settling velocity (Flanagan and Nearing, 2000). Sediment selectivity and sorting contribute to the heterogeneous pockets of different soil and SOC amounts along the downslope. In recent years, research on sediment selectivity and sorting have improved the modeling of SOC redistribution by considering the contribution of individual aggregate size classes (Chartier et al., 2013; Fu et al., 2016; Wang and Shi, 2015; Wang et al., 2014; Wang et al., 2013b).

The transport selectivity on SOC is usually expressed as an enrichment ratio (ER), calculated as the SOC component in the eroded soil to that of the source soil (Massey and Jackson, 1952). It is commonly believed that interrill erosion is more selective while rill erosion is less selective and even non-selective under general movement (Foster et al., 1985; Govers, 1985; Proffitt and Rose, 1991; Schiettecatte et al., 2008; Shi et al., 2012). During interrill erosion, silt/clay particles and finer aggregates, mostly 0.1~0.2 mm fractions (Van Dijk et al., 2002) are either peeled off from larger aggregates or ejected by raindrop impact and then selectively entrained by shallow sheet flow, resulting in high ER values of SOC (Palis et al., 1997; Schiettecatte et al., 2008; Wang et al., 2013b). Sutherland et al. (1996a) reported that the <0.063 mm and 0.05-0.1 mm fractions were preferentially transported by rainsplash and sheet flow, and the ER values were greater than 1. During rill erosion, ER values of SOC decrease close to 1 as high flow velocity dominates and tends to mobilize all size fractions (Papanicolaou et al., 2015; Schiettecatte et al., 2008). In other words, the eroded sediments have same aggregate size distribution and SOC concentration as the source soil because the shear stress of rill flow is sufficiently enough to mobilize all size fractions.

Selective transport of soil aggregates and labile SOC fractions not only occur in those specific erosion processes (rainsplash vs. rill erosion) but also vary based on specific environmental conditions, such as slope geometry, soil texture, rainfall intensity, and runoff. Slope gradient and rainfall intensity have been found to play essential roles in the selective enrichment of SOC by controlling stream power (Flanagan and Nearing, 2000). When the slope (e.g., <5°) or rainfall intensity (e.g., <45 mm h^{-1}) was sufficiently low, high ER values in each aggregate size class were observed due to selective transport of finer material by rainsplash and shallow flow (Liu et al., 2019; Papanicolaou et al., 2015). SOC enrichment also varies depending on the hillslope position. Papanicolaou et al. (2015) reported higher average ER values (~1.5) in the upslope than in the downslope (~1), which highlights the importance of rainsplash in the selective transport of finer fractions in the upslope.

Soil and SOC Movement Tracing

The use of sediment tracers as a tool to better understand erosion and deposition has increased due to additional information they provide, such as sediment source identification (Abban et al., 2016; Fox and Papanicolaou, 2008; Papanicolaou et al., 2003; Wilson et al., 2008), tracking of sediment movement across various spatial scales (Polyakov et al., 2009; Wilson, 2003; Wilson et al., 2005; Zhang et al., 2018), and estimation of soil erosion and deposition rates (Li et al., 2010; Olson et al., 2013). Guzmán et al. (2013) reviewed four commonly used tracers: REE, fallout radionuclides, stable isotopes, and magnetic substances. Since Zhang et al. (2001) first showed the reliability of REE to trace soil erosion, the use of REE has become more popular due to their small size (<5 μm), low background concentration, high affinity to aggregates, and noninterference with aggregate movement.

REE has been used to trace sediment movement across artificial hillslopes (Michaelides et al., 2010; Polyakov and Nearing, 2004) and catchments (Liu et al., 2016; Zhang et al., 2018) through simulated rainfall. Polyakov et al. (2004) and Polyakov et al. (2009) expanded the application of REE to a small natural watershed following storm events. In their study, all morphological zones were marked with distinct REE before rainfall, and traditional sediment fluxes and erosion rates were determined after rainfall with measured REE concentrations. Using REE as tracers, Matisoff et al. (2001) measured the transport distances of sediments after thunderstorms, which ranged from 3-73 cm. Overall, these studies indicate that REE tracing is a reliable approach to track soil particle movement across the landscape.

Knowledge Gaps

There are still numerous advances necessary to understand landscape sediment transport processes. For instance, the sediment transport distance reported by Matisoff et al. (2001) was for the bulk soil under the assumption that all soil particles traveled the same lengths, which is not the case. It is clear that smaller aggregates travel longer distances than coarser aggregates due to sediment selectivity and sorting. Determining transport distance for individual aggregate size fractions is critical to accurately visualize soil and SOC redistribution over the landscape and scale erosion rates.

Research Contributions

The knowledge gaps gleaned in this review must be addressed with targeted efforts to fully understand the spatial variability and SOC redistribution in intensively managed landscapes, particularly those that are low gradient. Thus, to inform these knowledge gaps, this research aims to accomplish the following objectives:

(1) Examine the roles of hillslope gradient and topographic depressions on the spatial variability of SOC in both high- and low-gradient agricultural landscapes and differentiate the dominant processes that control the SOC heterogeneity in the two environments with distinct topographies.
(2) Quantify the mass transfer between different aggregate size classes during breakdown and reaggregation cycles under natural rainfall using rare earth elements (REE) as tracers and examine dominant environment factors that control the mass transfer.
(3) Investigate the surface runoff and soil loss characteristics in field plots with different residue cover and tillage treatments using simulated rainfall and examine the aggregate transport selectivity and SOC enrichment ratio in the eroded sediments.
(4) Investigate the differences in transport distances of REE-tagged aggregate size classes at various slope positions in response to a series of rainfall events and examine their impacts on SOC redistribution over the landscape.

Dissertation Outline

The dissertation consists of six chapters: Chapter 1 is a general introduction. Chapter 2 presents a comparison study on the influence of topography on SOC spatial variability in high- and low-gradient agricultural landscapes. Chapter 3 presents a field study where aggregate turnover is tracked under raindrop impact and wetting-drying cycles using REE tracers. Chapter 4 presents a simulated rainfall study of soil erosion and SOC enrichment ratio by surface runoff in field plots with different tillage and residue cover treatments. Chapter 5 presents a field study for quantifying aggregate transport distances after rainfall events to understand SOC redistribution using REE tracers. Chapter 6 highlights the major conclusions from this dissertation and gives recommendations for future research.

References

Abban, B., Thanos Papanicolaou, A.N., Cowles, M.K., Wilson, C.G., Abaci, O., Wacha, K., Schilling, K., Schnoebelen, D., 2016. An enhanced Bayesian fingerprinting framework for studying sediment source dynamics in intensively managed landscapes. Water Resources Research 52(6), 4646-4673.

Agnese, C., Baiamonte, G., Corrao, C., 2007. Overland flow generation on hillslopes of complex topography: analytical solutions. Hydrological processes 21(10), 1308-1317.

Álvaro-Fuentes, J., Arrúe, J.L., Cantero-Martínez, C., López, M., 2008. Aggregate breakdown during tillage in a Mediterranean loamy soil. Soil tillage Research 101(1-2), 62-68.

Amezketa, E., 1999. Soil aggregate stability: a review. Journal of sustainable agriculture 14(2-3), 83-151.

Annabi, M., Raclot, D., Bahri, H., Bailly, J.S., Gomez, C., Le Bissonnais, Y., 2017. Spatial variability of soil aggregate stability at the scale of an agricultural region in Tunisia. CATENA 153, 157-167.

Barrios, E., 2007. Soil biota, ecosystem services and land productivity. Ecological Economics 64(2), 269-285.

Ben-Hur, M., Shainberg, I., Stern, R., van der Merwe, A., 1992. Slope and gypsum effects on infiltration and erodibility of dispersive and nondispersive soils. Soil Science Society of America Journal 56(5), 1571-1576.

Berhe, A.A., 2006. Storage, replacement, stabilization, and destabilization of soil organic carbon in eroding and depositional settings, University of California, Berkeley.

Berhe, A.A., Harden, J.W., Torn, M.S., Harte, J., 2008. Linking soil organic matter dynamics and erosion-induced terrestrial carbon sequestration at different landform positions. Journal of Geophysical Research: Biogeosciences 113(G4).

Berhe, A.A., Harden, J.W., Torn, M.S., Kleber, M., Burton, S.D., Harte, J., 2012. Persistence of soil organic matter in eroding versus depositional landform positions. Journal of Geophysical Research: Biogeosciences 117(G2).

Berhe, A.A., Harte, J., Harden, J.W., Torn, M.S., 2007. The significance of the erosion-induced terrestrial carbon sink. BioScience 57(4), 337-346.

Bertassello, L.E., Rao, P.S.C., Jawitz, J.W., Botter, G., Le, P.V.V., Kumar, P., Aubeneau, A.F., 2018. Wetlandscape Fractal Topography. 45(14), 6983-6991.

Bianchi, T.S., Galler, J.J., Allison, M.A., 2007. Hydrodynamic sorting and transport of terrestrially derived organic carbon in sediments of the Mississippi and Atchafalaya Rivers. Estuarine, Coastal and Shelf Science 73(1), 211-222.

Bielders, C.L., Grymonprez, B., 2010. Raindrop Impact: A Neglected but Potentially Major Contributor to Particle Mobilization in Soils. 74(5), 1446-1456.

Blanco-Canqui, H., Lal, R., 2004. Mechanisms of carbon sequestration in soil aggregates. Critical reviews in plant sciences 23(6), 481-504.

Boogar, A.M., Jahansouz, M.R., Reza, M., 2014. Soil aggregate size distribution and stability following conventional-till, minimum-till and no-till systems. Int J Farming Allied Sci 3, 512-517.

Braunack, M., Dexter, A., 1989a. Soil aggregation in the seedbed: a review II. Effect of aggregate sizes on plant growth. Soil Tillage Research 14(3), 281-298.

Braunack, M., Dexter, A., 1989b. Soil aggregation in the seedbed: a review. I. Properties of aggregates and beds of aggregates. Soil Tillage Research 14(3), 259-279.

Bronick, C.J., Lal, R., 2005. Soil structure and management: a review. Geoderma 124(1), 3-22.

Bronswijk, J.J.B., 1991. Magnitude, modeling and significance of swelling and shrinkage processes in clay soils, Bronswijk.

Cambardella, C., Elliott, E., 1994. Carbon and nitrogen dynamics of soil organic matter fractions from cultivated grassland soils. Soil Science Society of America Journal 58(1), 123-130.

Chaney, K., Swift, R.S., 1986. Studies on aggregate stability. I. Re-formation of soil aggregates. Journal of Soil Science 37(2), 329-335.

Chaplot, V., Podwojewski, P., Phachomphon, K., Valentin, C., 2009. Soil Erosion Impact on Soil Organic Carbon Spatial Variability on Steep Tropical Slopes. 73(3), 769-779.

Chappell, N.A., Ternan, J.L., Bidin, K., 1999. Correlation of physicochemical properties and sub-erosional landforms with aggregate stability variations in a tropical Ultisol disturbed by forestry operations. Soil and Tillage Research 50(1), 55-71.

Chartier, M.P., Rostagno, C.M., Videla, L.S., 2013. Selective erosion of clay, organic carbon and total nitrogen in grazed semiarid rangelands of northeastern Patagonia, Argentina. Journal of arid environments 88, 43-49.

Cohen, M.J., Creed, I.F., Alexander, L., Basu, N.B., Calhoun, A.J.K., Craft, C., D'Amico, E., DeKeyser, E., Fowler, L., Golden, H.E., 2016. Do geographically isolated wetlands influence landscape functions? PNAS 113(8), 1978-1986.

De Gryze, S., Six, J., Brits, C., Merckx, R., 2005. A quantification of short-term macroaggregate dynamics: influences of wheat residue input and texture. Soil Biology Biochemistry 37(1), 55-66.

De Gryze, S., Six, J., Merckx, R., 2006. Quantifying water-stable soil aggregate turnover and its implication for soil organic matter dynamics in a model study. European Journal of Soil Science 57(5), 693-707.

de Nijs, E.A., Cammeraat, E.L.H., 2020. The stability and fate of Soil Organic Carbon during the transport phase of soil erosion. Earth-Science Reviews 201, 103067.Dexter, A., 1988. Advances in characterization of soil structure. Soil and Tillage Research 11(3-4), 199-238.

Díaz-Zorita, M., Perfect, E., Grove, J.H., 2002. Disruptive methods for assessing soil structure. Soil and Tillage Research 64(1), 3-22.

Doetterl, S., Berhe, A.A., Nadeu, E., Wang, Z., Sommer, M., Fiener, P., 2016. Erosion, deposition and soil carbon: A review of process-level controls, experimental tools and models to address C cycling in dynamic landscapes. Earth-Science Reviews 154, 102-122.

Doetterl, S., Six, J., Van Wesemael, B., Van Oost, K., 2012. Carbon cycling in eroding landscapes: geomorphic controls on soil organic C pool composition and C stabilization. Global Change Biology 18(7), 2218-2232.

Douglas, L., 1985. Aggregate breakdown in relation to raindrop energy. Soil Science 139(3), 239-242.

Ekwue, E., 1990. Effect of organic matter on splash detachment and the processes involved. Earth Surface Processes Landforms 15(2), 175-181.

Elliott, E., 1986. Aggregate Structure and Carbon, Nitrogen, and Phosphorus in Native and Cultivated Soils 1. Soil science society of America journal 50(3), 627-633.

Farres, P., 1987. The dynamics of rainsplash erosion and the role of soil aggregate stability. Catena 14(1-3), 119-130.

Feller, C., Beare, M.H., 1997. Physical control of soil organic matter dynamics in the tropics. Geoderma 79(1), 69-116.

Fiener, P., Dlugoß, V., Van Oost, K., 2015. Erosion-induced carbon redistribution, burial and mineralisation—Is the episodic nature of erosion processes important? Catena 133, 282-292.

Fissore, C., Dalzell, B.J., Berhe, A.A., Voegtle, M.A., Evans, M.A., Wu, A., 2017. Influence of topography on soil organic carbon dynamics in a Southern California grassland. Catena 149, 140-149.

Flanagan, D., Nearing, M., 2000. SEDIMENT PARTICLE SORTING ON HILLSLOPE PROFILES IN THE WEPP MODEL. Transactions of the ASAE 43(3), 573-583.

Flanagan, D.C., Ascough, J.C., Nearing, M.A., Laflen, J.M., 2001. The water erosion prediction project (WEPP) model, Landscape erosion and evolution modeling. Springer, pp. 145-199.

Foster, G., Young, R., Römkens, M., Onstad, C., 1985. Processes of soil erosion by water. Soil erosion crop productivity, 137-162.

Foufoula-Georgiou, E., Ganti, V., Dietrich, W., 2010. A nonlocal theory of sediment transport on hillslopes. Journal of Geophysical Research: Earth Surface 115(F2).

Fox, J.F., Papanicolaou, A.N., 2008. Application of the spatial distribution of nitrogen stable isotopes for sediment tracing at the watershed scale. Journal of Hydrology 358(1), 46-55.

Fu, Y., Li, G., Zheng, T., Li, B., Zhang, T., 2016. Impact of raindrop characteristics on the selective detachment and transport of aggregate fragments in the Loess Plateau of China. Soil Science Society of America Journal 80(4), 1071-1077.

Gabbard, D., Huang, C.-h., Norton, L., Steinhardt, G., 1998. Landscape position, surface hydraulic gradients and erosion processes. Earth Surface Processes Landforms: The Journal of the British Geomorphological Group 23(1), 83-93.

Gerard, C., 1987. Laboratory experiments on the effects of antecedent moisture and residue application on aggregation of different soils. Soil & Tillage Research 9(1), 21-32.

Govers, G., 1985. Selectivity and transport capacity of thin flows in relation to rill erosion. Catena 12(1), 35-49.

Guzmán, G., Quinton, J.N., Nearing, M.A., Mabit, L., Gómez, J.A., 2013. Sediment tracers in water erosion studies: current approaches and challenges. Journal of Soils and Sediments 13(4), 816-833.

Hogarth, W.L., Parlange, J.-Y., Rose, C., Sander, G., Steenhuis, T., Barry, A., 2004. Soil erosion due to rainfall impact with inflow: an analytical solution with spatial and temporal effects. Journal of hydrology 295(1-4), 140-148.

Horn, R., Taubner, H., Wuttke, M., Baumgartl, T., 1994. Soil physical properties related to soil structure. Soil Tillage Research 30(2-4), 187-216.

Hou, T., Berry, T.D., Singh, S., Hughes, M.N., Tong, Y., Thanos Papanicolaou, A.N., Wacha, K.M., Wilson, C.G., Chaubey, I., Filley, T.R., 2018. Control of tillage disturbance on the chemistry and proportion of raindrop-liberated particles from soil aggregates. Geoderma 330, 19-29.

Hoyos, N., Comerford, N.B., 2005. Land use and landscape effects on aggregate stability and total carbon of Andisols from the Colombian Andes. Geoderma 129(3-4), 268-278.

Huang, C., Bradford, J., Cushman, J., 1983. A numerical study of raindrop impact phenomena: the elastic deformation case. Soil Science Society of America Journal 47(5), 855-861.

Huang, C., Gascuel-Odoux, C., Cros-Cayot, S., 2002. Hillslope topographic and hydrologic effects on overland flow and erosion. Catena 46(2-3), 177-188.

Karlen, D.L., Stott, D.E., 1994. A framework for evaluating physical and chemical indicators of soil quality. Defining soil quality for a sustainable environment 35, 53-72.

Kemper, W., Rosenau, R., 1986. Aggregate stability and size distribution.

Kirkels, F.M.S.A., Cammeraat, L.H., Kuhn, N.J., 2014. The fate of soil organic carbon upon erosion, transport and deposition in agricultural landscapes — A review of different concepts. Geomorphology 226, 94-105.

Lal, R., 2006. Enhancing crop yields in the developing countries through restoration of the soil organic carbon pool in agricultural lands. Land Degradation & Development 17(2), 197-209.

Le Bissonnais, Y., 1996. Aggregate stability and assessment of soil crustability and erodibility: I. Theory and methodology. European Journal of Soil Science 47(4), 425-437.

Le Bissonnais, Y., Arrouays, D., 1997. Aggregate stability and assessment of soil crustability and erodibility: II. Application to humic loamy soils with various organic carbon contents. J European Journal of Soil Science 48(1), 39-48.

Le Bissonnais, Y., Cros-Cayot, S., Gascuel-Odoux, C., 2002. Topographic dependence of aggregate stability, overland flow and sediment transport. Agronomie 22(5), 489-501.

Le, P.V., Kumar, P., 2017. Interaction between ecohydrologic dynamics and microtopographic variability under climate change. Water Resources Research 53(10), 8383-8403.

Le, P.V.V., Kumar, P., 2014. Power law scaling of topographic depressions and their hydrologic connectivity. Geophysical Research Letters 41(5), 1553-1559.

Legout, C., Leguedois, S., Le Bissonnais, Y., 2005. Aggregate breakdown dynamics under rainfall compared with aggregate stability measurements. European Journal of Soil Science 56(2), 225-238.

Li, H., Zhang, X., Wang, K., Wen, A., 2010. Assessment of sediment deposition rates in a karst depression of a small catchment in Huanjiang, Guangxi, southwest China, using the cesium-137 technique. Journal of soil and water conservation 65(4), 223-232.

Li, Z., Yang, W., Cai, C., Wang, J., 2013. Aggregate mechanical stability and relationship with aggregate breakdown under simulated rainfall. Soil science 178(7), 369-377.

Liang, A., Zhang, Y., Zhang, X., Yang, X., McLaughlin, N., Chen, X., Guo, Y., Jia, S., Zhang, S., Wang, L., 2019. Investigations of relationships among aggregate pore structure, microbial biomass, and soil organic carbon in a Mollisol using combined non-destructive measurements and phospholipid fatty acid analysis. Soil Tillage Research 185, 94-101.

Liu, G., Xiao, H., Liu, P., Zhang, Q., Zhang, J., 2016. An improved method for tracing soil erosion using rare earth elements. Journal of Soils and Sediments 16(5), 1670-1679.

Liu, L., Li, Z., Xiao, H., Wang, B., Nie, X., Liu, C., Ni, L., Wang, D., 2019. The transport of aggregates associated with soil organic carbon under the rain-induced overland flow on the Chinese Loess Plateau. 44(10), 1895-1909.

Loch, R.J., Foley, J.L., 1994. Measurement of aggregate breakdown under rain-Comparison with tests of water stability and relationships with field measurements of infiltration. Soil Research 32(4), 701-720.

Márquez, C., Garcia, V., Cambardella, C.A., Schultz, R.C., Isenhart, T.M., 2004. Aggregate-size stability distribution and soil stability. Soil Science Society of America Journal 68(3), 725-735.

Martz, L.W., 1992. The variation of soil erodibility with slope position in a cultivated canadian prairie landscape. Earth Surface Processes and Landforms 17(6), 543-556.
Massey, H., Jackson, M., 1952. Selective Erosion of Soil Fertility Constituents 1. Soil Science Society of America Journal 16(4), 353-356.
Mathier, L., Roy, A., 1993. Temporal and spatial variations of runoff and rainwash erosion on an agricultural field. Hydrological processes 7(1), 1-18.
Matisoff, G., Ketterer, M.E., Wilson, C.G., Layman, R., Whiting, P.J., 2001. Transport of Rare Earth Element-Tagged Soil Particles in Response to Thunderstorm Runoff. Environmental Science & Technology 35(16), 3356-3362.
Meersmans, J., De Ridder, F., Canters, F., De Baets, S., Van Molle, M., 2008. A multiple regression approach to assess the spatial distribution of Soil Organic Carbon (SOC) at the regional scale (Flanders, Belgium). Geoderma 143(1), 1-13.
Michaelides, K., Ibraim, I., Nord, G., Esteves, M., 2010. Tracing sediment redistribution across a break in slope using rare earth elements. Earth Surface Processes and Landforms: The Journal of the British Geomorphological Research Group 35(5), 575-587.
Miller, B.A., Schaetzl, R.J., 2015. Digital classification of hillslope position. Soil Science Society of America Journal 79(1), 132-145.
Nciizah, A.D., Wakindiki, I.I.C., 2015. Physical indicators of soil erosion, aggregate stability and erodibility. Arch. Agron. Soil Sci. 61(6), 827-842.
Nearing, M., Bradford, J., 1985. Single Waterdrop Splash Detachment and Mechanical Properties of Soils 1. Soil Science Society of America Journal 49(3), 547-552.
Nearing, M., Bradford, J., Holtz, R., 1987. Measurement of waterdrop impact pressures on soil surfaces. Soil Science Society of America Journal 51(5), 1302-1306.
Nouwakpo, S.K., Song, J., Gonzalez, J.M., 2018. Soil structural stability assessment with the fluidized bed, aggregate stability, and rainfall simulation on long-term tillage and crop rotation systems. Soil Tillage Research 178, 65-71.
Oades, J., Waters, A., 1991. Aggregate hierarchy in soils. Soil Research 29(6), 815-828.
Oades, J.M., 1984. Soil organic matter and structural stability: mechanisms and implications for management. Plant and Soil 76(1-3), 319-337.
Olson, K.R., Gennadiyev, A., Zhidkin, A., Markelov, M., Golosov, V., Lang, J., 2013. Use of magnetic tracer and radio-cesium methods to determine past cropland soil erosion amounts and rates. Catena 104, 103-110.
Palis, R., Ghandiri, H., Rose, C., Saffigna, P.J.S.R., 1997. Soil erosion and nutrient loss. III.¤ Changes in the enrichment ratio of total nitrogen and organic carbon under rainfall detachment and entrainment. 35(4), 891-906.
Papanicolaou, A.N., Fox, J.F., Marshall, J., 2003. Soil fingerprinting in the Palouse Basin, USA, using stable carbon and nitrogen isotopes. International Journal of Sediment Research 18(2), 278-284.

Papanicolaou, A.N.T., Wacha, K.M., Abban, B.K., Wilson, C.G., Hatfield, J.L., Stanier, C.O., Filley, T.R., 2015. From soilscapes to landscapes: A landscape-oriented approach to simulate soil organic carbon dynamics in intensively managed landscapes. Journal of Geophysical Research: Biogeosciences 120(11), 2375-2401.

Passalacqua, P., Belmont, P., Staley, D.M., Simley, J.D., Arrowsmith, J.R., Bode, C.A., Crosby, C., DeLong, S.B., Glenn, N.F., Kelly, S.A., Lague, D., Sangireddy, H., Schaffrath, K., Tarboton, D.G., Wasklewicz, T., Wheaton, J.M., 2015. Analyzing high resolution topography for advancing the understanding of mass and energy transfer through landscapes: A review. Earth-Science Reviews 148, 174-193.

Peng, X., Zhu, Q., Zhang, Z., Hallett, P.D., 2017. Combined turnover of carbon and soil aggregates using rare earth oxides and isotopically labelled carbon as tracers. Soil Biology Biochemistry 109, 81-94.

Pierson, F.B., Mulla, D.J., 1990. Aggregate Stability in the Palouse Region of Washington: Effect of Landscape Position. 54(5), 1407-1412.

Plante, A., Feng, Y., McGill, W., 2002. A modeling approach to quantifying soil macroaggregate dynamics. Canadian Journal of Soil Science 82(2), 181-190.

Plante, A.F., Duke, M.J.M., McGill, W.B., 1999. A Tracer Sphere Detectable by Neutron Activation for Soil Aggregation and Translocation Studies. 63(5), 1284-1290.

Plante, A.F., McGill, W.B., 2002. Soil aggregate dynamics and the retention of organic matter in laboratory-incubated soil with differing simulated tillage frequencies. Soil and Tillage Research 66(1), 79-92.

Polyakov, V., Kimoto, A., Nearing, M., Nichols, M., 2009. Tracing sediment movement on a semiarid watershed using rare earth elements. Soil Science Society of America Journal 73(5), 1559-1565.

Polyakov, V., Nearing, M., 2004. Rare earth element oxides for tracing sediment movement. Catena 55(3), 255-276.

Polyakov, V., Nearing, M., Shipitalo, M., 2004. Tracking sediment redistribution in a small watershed: implications for agro-landscape evolution. Earth Surface Processes and Landforms: The Journal of the British Geomorphological Research Group 29(10), 1275-1291.

Proffitt, A., Rose, C., 1991. Soil erosion processes. II. Settling velocity characteristics of eroded sediment. Soil Research Erosion, conservation 29(5), 685-695.

Proffitt, A., Rose, C., Hairsine, P., 1991. Rainfall detachment and deposition: Experiments with low slopes and significant water depths. Soil Science Society of America Journal 55(2), 325-332.

Pulleman, M., Six, J., Van Breemen, N., Jongmans, A., 2005. Soil organic matter distribution and microaggregate characteristics as affected by agricultural management and earthworm activity. European Journal of Soil Science 56(4), 453-467.

Reddy, K.R., Patrick, W.H., 1975. Effect of alternate aerobic and anaerobic conditions on redox potential, organic matter decomposition and nitrogen loss in a flooded soil. Soil Biology and Biochemistry 7(2), 87-94.

Renard, K.G., Foster, G.R., Weesies, G.A., Porter, J.P., 1991. RUSLE: Revised universal soil loss equation. Journal of Soil Water Conservation 46(1), 30-33.

Roering, J.J., Kirchner, J.W., Dietrich, W.E., 1999. Evidence for nonlinear, diffusive sediment transport on hillslopes and implications for landscape morphology. Water Resources Research 35(3), 853-870.

Roering, J.J., Kirchner, J.W., Dietrich, W.E., 2001. Hillslope evolution by nonlinear, slope-dependent transport: Steady state morphology and equilibrium adjustment timescales. Journal of Geophysical Research: Solid Earth 106(B8), 16499-16513.

Ruhe, R.V., 1960. Elements of the soil landscape. Transactions 7th int. Congr. Soil Sci. 4, 165-170.

Sarker, J.R., Singh, B.P., Cowie, A.L., Fang, Y., Collins, D., Badgery, W., Dalal, R.C., 2018. Agricultural management practices impacted carbon and nutrient concentrations in soil aggregates, with minimal influence on aggregate stability and total carbon and nutrient stocks in contrasting soils. Soil Tillage Research 178, 209-223.

Schiettecatte, W., Gabriels, D., Cornelis, W.M., Hofman, G., 2008. Enrichment of organic carbon in sediment transport by interrill and rill erosion processes. Soil Science Society of America Journal 72(1), 50-55.

Schwanghart, W., Jarmer, T., 2011. Linking spatial patterns of soil organic carbon to topography—a case study from south-eastern Spain. Geomorphology 126(1-2), 252-263.

Serio, M.A., Carollo, F.G., Ferro, V., 2019. A method for evaluating rainfall kinetic power by a characteristic drop diameter. Journal of Hydrology, 123996.

Sexstone, A.J., Revsbech, N.P., Parkin, T.B., Tiedje, J.M., 1985. Direct Measurement of Oxygen Profiles and Denitrification Rates in Soil Aggregates1. 49(3), 645-651.

Shi, P., Thorlacius, S., Keller, T., Keller, M., Schulin, R., 2017. Soil aggregate breakdown in a field experiment with different rainfall intensities and initial soil water contents. 68(6), 853-863.

Shi, Z., Fang, N., Wu, F., Wang, L., Yue, B., Wu, G., 2012. Soil erosion processes and sediment sorting associated with transport mechanisms on steep slopes. Journal of Hydrology 454, 123-130.

Shih, H.-M., Yang, C.T., 2009. Estimating overland flow erosion capacity using unit stream power. International Journal of Sediment Research 24(1), 46-62.

Six, J., Bossuyt, H., Degryze, S., Denef, K., 2004. A history of research on the link between (micro) aggregates, soil biota, and soil organic matter dynamics. Soil Tillage Research 79(1), 7-31.

Six, J., Elliott, E., Paustian, K., 2000a. Soil macroaggregate turnover and microaggregate formation: a mechanism for C sequestration under no-tillage agriculture. Soil Biology and Biochemistry 32(14), 2099-2103.

Six, J., Elliott, E., Paustian, K., Doran, J., 1998. Aggregation and soil organic matter accumulation in cultivated and native grassland soils. Soil Science Society of America Journal 62(5), 1367-1377.

Six, J., Guggenberger, G., Paustian, K., Haumaier, L., Elliott, E.T., Zech, W., 2001. Sources and composition of soil organic matter fractions between and within soil aggregates. 52(4), 607-618.

Six, J., Paustian, K., Elliott, E.T., Combrink, C., 2000b. Soil Structure and Organic Matter I. Distribution of Aggregate-Size Classes and Aggregate-Associated Carbon. Soil Science Society of America Journal 64(2), 681-689.

Skidmore, E.L., Layton, J.B., 1992. Dry-Soil Aggregate Stability as Influenced by Selected Soil Properties. Soil Science Society of America Journal 56(2), 557-561.

Song, K., Zheng, X., Lv, W., Qin, Q., Sun, L., Zhang, H., Xue, Y., 2019. Effects of tillage and straw return on water-stable aggregates, carbon stabilization and crop yield in an estuarine alluvial soil. Scientific reports 9(1), 1-11.

Stallard, R., 1998. Terrestrial sedimentation and the carbon cycle: Coupling weathering and erosion to carbon burial. Global biogeochemical cycles 12(2), 231-257.

Staricka, J., Benoit, G., 1995. Freeze-drying effects on wet and dry soil aggregate stability. Soil science society of America journal 59(1), 218-223.

Staricka, J.A., Allmaras, R.R., Nelson, W.W., Larson, W.E., 1992. Soil Aggregate Longevity as Determined by the Incorporation of Ceramic Spheres. 56(5), 1591-1597.

Stevens, F., Bogaert, P., Van Oost, K., Doetterl, S., Van Wesemael, B., 2014. Regional-scale characterization of the geomorphic control of the spatial distribution of soil organic carbon in cropland. European Journal of Soil Science 65(4), 539-552.

Sutherland, R., Wan, Y., Lee, C.-T., Ziegler, A., 1996a. Aggregate enrichment ratios for splash and wash transported sediment from an Oxisol. Catena 26(3-4), 187-208.

Sutherland, R., Watung, R., El-Swaify, S., Landforms, 1996b. Splash transport of organic carbon and associated concentration and mass enrichment ratios for an Oxisol, Hawaii. Earth Surface Processes and Landforms 21(12), 1145-1162.

Tang, C., Shi, B., 2011. Swelling and shrinkage behaviour of expansive soil during wetting–drying cycles. Chinese Journal of Geotechnical Engineering 33(9), 1376-1384.

Thompson, S.E., Katul, G.G., Porporato, A., 2010. Role of microtopography in rainfall-runoff partitioning: An analysis using idealized geometry. Water Resources Research 46(7).

Tisdall, J., 1991. Fungal hyphae and structural stability of soil. Soil Reserach 29(6), 729-743.

Tisdall, J.M., Oades, J.M., 1982. Organic matter and water-stable aggregates in soils. Journal of soil science 33(2), 141-163.
Truman, C.C., Bradford, J.M., Ferris, J.E., 1990. Antecedent water content and rainfall energy influence on soil aggregate breakdown. Soil Science Society of America Journal 54(5), 1385-1392.
Tu, C.L., He, T.B., Lu, X.H., Luo, Y., Smith, P., 2018. Extent to which pH and topographic factors control soil organic carbon level in dry farming cropland soils of the mountainous region of Southwest China. Catena 163, 204-209.
USDA, 2004. Soil Survey of Sangamon County, Illinois. Natural Resources Conservation Service.
Van Dijk, A., Meesters, A., Bruijnzeel, L., 2002. Exponential distribution theory and the interpretation of splash detachment and transport experiments. Soil Science Society of America Journal 66(5), 1466-1474.
VandenBygaart, A.J., Gregorich, E.G., Angers, D.A., McConkey, B.G., 2007. Assessment of the lateral and vertical variability of soil organic carbon. Canadian Journal of Soil Science 87(4), 433-444.
Vieira, S.R., Paz Gonzalez, A., 2003. Analysis of the spatial variability of crop yield and soil properties in small agricultural plots. Bragantia 62(1), 127-138.
Wacha, K., Papanicolaou, A., Giannopoulos, C., Abban, B., Wilson, C., Zhou, S., Hatfield, J., Filley, T., Hou, T., 2018. The Role of Hydraulic Connectivity and Management on Soil Aggregate Size and Stability in the Clear Creek Watershed, Iowa. Geosciences 8(12), 470.
Wainwright, J., Parsons, A.J., Müller, E.N., Brazier, R.E., Powell, D.M., Fenti, B., 2008. A transport-distance approach to scaling erosion rates: 2. Sensitivity and evaluation of MAHLERAN. Earth Surface Processes and Landforms: The Journal of the British Geomorphological Research Group 33(6), 962-984.
Wang, J.-G., Li, Z.-X., Cai, C.-F., Yang, W., Ma, R.-M., Zhang, G.-B., 2013a. Effects of stability, transport distance and two hydraulic parameters on aggregate abrasion of Ultisols in overland flow. Soil and Tillage Research 126, 134-142.
Wang, J., Li, Z., Cai, C., Yang, W., 2012. Effects of transport distance and flow discharge of overland flow on destruction of Ultisol aggregates. Particuology 10(5), 607-613.
Wang, L., Shi, Z., 2015. Size selectivity of eroded sediment associated with soil texture on steep slopes. Soil Science Society of America Journal 79(3), 917-929.
Wang, L., Shi, Z., Wang, J., Fang, N., Wu, G., Zhang, H., 2014. Rainfall kinetic energy controlling erosion processes and sediment sorting on steep hillslopes: a case study of clay loam soil from the Loess Plateau, China. J Journal of Hydrology 512, 168-176.
Wang, Y., Zhang, J.H., Zhang, Z.H., 2015. Influences of intensive tillage on water-stable aggregate distribution on a steep hillslope. Soil and Tillage Research 151, 82-92.

Wang, Z., Govers, G., Oost, K.V., Clymans, W., den Putte, A.V., Merckx, R., 2013b. Soil organic carbon mobilization by interrill erosion: Insights from size fractions. Journal of Geophysical Research: Earth Surface 118(2), 348-360.

Whalen, J.K., Chang, C., 2002. Macroaggregate characteristics in cultivated soils after 25 annual manure applications. Soil Science Society of America Journal 66(5), 1637-1647.

Wickings, K., Grandy, A.S., Kravchenko, A.N., 2016. Going with the flow: Landscape position drives differences in microbial biomass and activity in conventional, low input, and organic agricultural systems in the Midwestern US. Agriculture, Ecosystems Environment international 218, 1-10.

Wilson, C.G., 2003. The transport of fines sediment through three NERR estuaries using radionuclide tracers.

Wilson, C.G., Kuhnle, R.A., Bosch, D.D., Steiner, J.L., Starks, P., Tomer, M.D., Wilson, G.V., 2008. Quantifying relative contributions from sediment sources in Conservation Effects Assessment Project watersheds. Journal of Soil and Water Conservation 63(6), 523-532.

Wilson, C.G., Matisoff, G., Whiting, P.J., Klarer, D.M., 2005. Transport of fine sediment through a wetland using radionuclide tracers: Old Woman Creek, OH. Journal of Great Lakes Research 31(1), 56-67.

Wilson, C.G., Wacha, K.M., Papanicolaou, A.N., Sander, H.A., Freudenberg, V.B., Abban, B.K.B., Zhao, C., 2016. Dynamic Assessment of Current Management in an Intensively Managed Agroecosystem. Journal of Contemporary Water Research & Education 158(1), 148-171.

Wysocki, D.A., Schoeneberger, P.J., LaGarry, H., 2000. Geomorphology of soil landscapes. Handbook of soil science 1, 315-321.

Xiao, H., Liu, G., Zhang, Q., Fenli, Z., Zhang, X., Liu, P., Zhang, J., Hu, F., Elbasit, M.A., 2018. Quantifying contributions of slaking and mechanical breakdown of soil aggregates to splash erosion for different soils from the Loess plateau of China. Soil Tillage Research 178, 150-158.

Xin, Z., Qin, Y., Yu, X., 2016. Spatial variability in soil organic carbon and its influencing factors in a hilly watershed of the Loess Plateau, China. CATENA 137, 660-669.

Yan, Q., Le, P., Vu Viet, Woo, D.K., Hou, T., Filley, T., R., Kumar, P., 2019. 3-D Modeling of the Co-evolution of Landscape and Soil Organic Carbon. Water Resources Research 0(ja).

Yoo, K., Amundson, R., Heimsath, A.M., Dietrich, W.E., 2005. Erosion of upland hillslope soil organic carbon: Coupling field measurements with a sediment transport model. Global Biogeochemical Cycles 19(3).

Yoo, K., Amundson, R., Heimsath, A.M., Dietrich, W.E., 2006. Spatial patterns of soil organic carbon on hillslopes: Integrating geomorphic processes and the biological C cycle. Geoderma 130(1-2), 47-65.

Zachar, D., 2011. Soil erosion. Elsevier.
Zhang, S., Li, Q., Zhang, X., Wei, K., Chen, L., Liang, W., 2012. Effects of conservation tillage on soil aggregation and aggregate binding agents in black soil of Northeast China. Soil and Tillage Research 124, 196-202.
Zhang, X.-c., Liu, G., Zheng, F., 2018. Understanding erosion processes using rare earth element tracers in a preformed interrill-rill system. Science of The Total Environment 625, 920-927.
Zhang, X., Friedrich, J., Nearing, M.A., Norton, L., 2001. Potential use of rare earth oxides as tracers for soil erosion and aggregation studies. Soil Science Society of America Journal 65(5), 1508-1515.
Zhao, P., Li, S., Wang, E., Chen, X., Deng, J., Zhao, Y., 2018. Tillage erosion and its effect on spatial variations of soil organic carbon in the black soil region of China. Soil Tillage Research 178, 72-81.
Zheng, H., Liu, W., Zheng, J., Luo, Y., Li, R., Wang, H., Qi, H., 2018. Effect of long-term tillage on soil aggregates and aggregate-associated carbon in black soil of Northeast China. PloS one 13(6).

CHAPTER TWO

TOPOGRAPHIC CONTROL ON SOIL ORGANIC CARBON SPATIAL VARIABILITY IN HIGH- AND LOW-GRADIENT AGRICULTURAL LANDSCAPES

A version of this chapter has been submitted to the peer-reviewed journal *Geoderma* for publication as Zhou, S., Papanicolaou, A.T., Wilson, C.G., Giannopoulos, C.P., Wacha, K.M., Hou, T., Filley, T.R., Rhoads, B.L., Topographic control on soil organic carbon spatial variability in high- and low-gradient agricultural landscapes.

Abstract: This study investigated the SOC spatial variability in two intensively managed landscapes (IMLs): Clear Creek, IA, a rolling, hilly, well-connected drainage environment, and the Upper Sangamon River, IL, a low-relief, poorly-connected drainage environment with topographic depressions. Representative hillslopes from both watersheds were selected with different hillslope gradients (HG). Soil samples from 0-5 cm and 5-10 cm deep were collected at the summit, shoulder, backslope, and toeslope positions of each hillslope following the primary flowpaths. SOC concentrations were determined using visible and near-infrared spectroscopy (Vis-NIR) and partial least squares regression (PLSR). For the high-gradient Clear Creek, HG was negatively correlated with SOC and accounted for most of the variation in SOC. Through erosion and deposition, lower SOC concentrations were found near the summits and higher levels were at the toeslopes. For the low-gradient Upper Sangamon River, gravimetric water content (GWC) and soil bulk density (BD) were positively correlated with SOC and accounted for most of the SOC variation. In the fields pocketed with depressions, the highest SOC concentrations appeared in these depressions compared to surrounding rises due to the deposition of SOC-rich fine sediments along with reduced microbial decomposition of carbon under anoxic conditions from elevated soil moisture. In contrast to observations for non-depressions, higher SOC concentration was found at 5-10 cm than at 0-5 cm within the depressions. SOC concentrations in Clear Creek were 25% lower on average than that in the Upper Sangamon River. Moreover, the SOC concentrations in Clear Creek exhibited a unimodal distribution and thus were more homogeneous than the SOC concentrations in the Sangamon, which displayed a multimodal distribution. The results suggest that the relatively low degree of SOC variability in high-gradient agricultural landscapes is mainly related to enhanced erosional mobilization and mixing under high surface runoff. By comparison, the high degree of SOC variability in low-gradient landscapes is governed by local depressions that trap SOC and hinder biogeochemical weathering under anoxic conditions, a process that fundamentally depends on topography.
Keywords: Soil organic carbon, Spatial variability, Visible and near-infrared spectroscopy, Topography, Hillslope gradient, Topographic depressions

Introduction

Soil organic carbon (SOC) is integral to soil health and agroecosystem resilience, playing crucial roles in the physical, ecohydrological, and biogeochemical functioning of agricultural soils (Reeves, 1997; Wiesmeier et al., 2019). Understanding the spatial variability of SOC at the field and watershed scales is essential for implementing sustainable land management practices (Moorman et al., 2004) and for informing carbon budgets and carbon transport models (Scharlemann et al., 2014; Yoo et al., 2005). SOC can exhibit high heterogeneity vertically through the soil profile and laterally across the soil surface, especially in intensively managed landscapes (IMLs) where human activity (e.g., tillage) has facilitated its mobility (VandenBygaart et al., 2007). In IMLs, interactions between land management and topography, which includes both gradient and curvature, shape SOC heterogeneity over short time scales of storm events and seasons (Li et al., 2018; Schwanghart and Jarmer, 2011; West and Post, 2002; Yu et al., 2018). Topography regulates overland flow and the resulting lateral/ downslope movement of soil and associated SOC, as gradient controls stream power and the transfer of momentum from the flowing water to the soil particles (Ali et al., 2013; Fissore et al., 2017; Patton et al., 2019; Papanicolaou et al., 2018; Shih and Yang, 2009). Different degrees of stream power selectively entrains lighter, less dense, carbon-rich material translocating it from steep upslope eroding zones to relatively flat downslope depositional zones (Figure 2-1a).

Topography, in the form of closed depressions, also affects the spatial heterogeneity of SOC. "Saucer-shaped" depressions usually have no natural outlets of surface flow and end up being storage zones for SOC (USDA, 2004; Figure 2-1b). In low-relief landscapes, topographic depressions create small, temporary ponded areas that experience anoxic conditions (Le and Kumar, 2017; Woo and Kumar, 2017). The reduced microbial metabolism of carbon caused by anoxic conditions increases SOC storage in the depressions (Keiluweit et al., 2016; Skopp et al., 1990).

Land management practices can alter the degree of SOC variability induced by topography (Hao et al., 2002). Tillage disintegrates aggregates, liberating the protected SOC and increasing its susceptibility for mobilization (Hou et al., 2018; Wacha et al., 2018). Additionally, tillage accelerates oxidation by aerating and drying the soil and increases the degree of contact between carbon-consuming microbes and SOC (Abid and Lal, 2008; John et al., 2005; Six et al., 2000). Many studies have reported lower SOC concentrations in fields under conventional tillage and higher SOC in fields with reduced tillage or no-till practices (Elliott and Efetha, 1999; Lopez-Bellido et al., 2017; West and Post, 2002).

To assess the spatial variability of SOC at larger scales, high-resolution mapping of near-surface SOC is required. These assessments generally involve extensive field campaigns with soil cores collected at different hillslope positions followed by analysis in the laboratory (Fox and Papanicolaou, 2007; Wilson et al., 2018). Increasingly, visible and near-infrared spectroscopy (Vis-NIR) is being used as a low-cost, rapid method to quantify SOC for large numbers of samples (Ben-Dor and Banin, 1995; Chang and Laird, 2002; Ge et al., 2014; Morgan et al., 2009; Viscarra Rossel et al., 2006). The Vis-NIR technique is part of the USDA-NRCS Rapid Carbon Assessment (RaCA) project for mapping carbon stocks in the U.S. and the European Land Use/Cover Area frame Statistical Survey (LUCAS) to develop a reference database for simulating carbon changes (Stevens et al., 2013; Wijewardane et al., 2016; Wills et al., 2014).

Vis-NIR detects the O-H, C-H, N-H, and C=O functional groups in organic molecules based on their optical properties (Margenot et al., 2015; Zou et al., 2010). When a soil sample interacts with Vis-NIR light, the functional groups vibrate as they absorb the light energy (Stenberg et al., 2010). Soils with more organic molecules, which are darker in

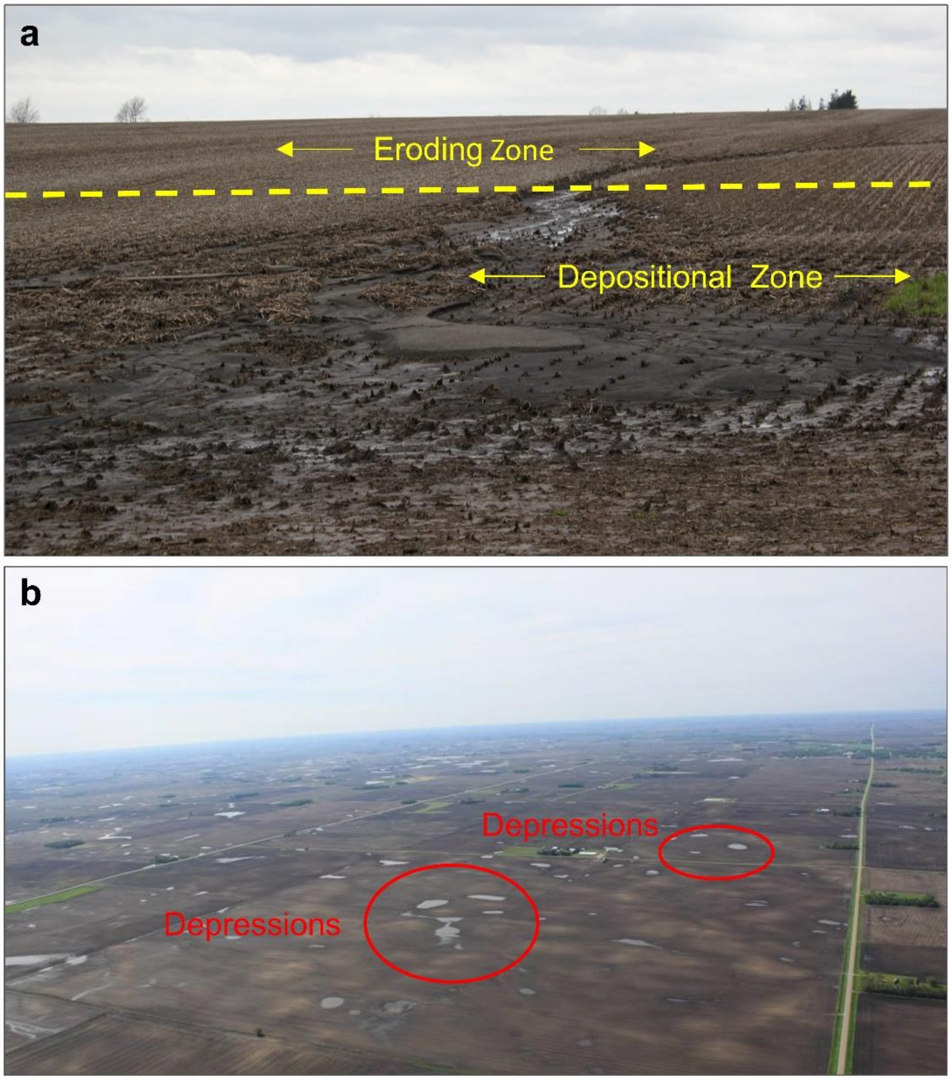

Figure 2-1. Examples of typical topographic features in high- and low-gradient IMLs. (a) In Clear Creek, the collective effects of rainsplash-, runoff-, and tillage-induced erosion/deposition redistribute finer soil particles and SOC along the hillslope (adapted from *Papanicolaou et al.* [2015]); (b) In the Upper Sangamon watershed, surface ponding in isolated topographic depressions (red circles) during intense rainfall events (photo courtesy of Dr. Thanos Papanicolaou). The two images at different spatial scales illustrate different topographic features.

color, absorb more light energy than lighter soils with less organic molecules (Ingleby and Crowe, 1999). Absorption of light energy in the visible region (i.e., 400-700 nm) occurs due to chromophores, whereas light absorption in the NIR region arises from overtones of the OH, SO_4, and CO_3 groups occurring at 700-1900 nm and from combinations of H_2O and CO_2 groups between 1900-2500 nm (Chang et al., 2005; Chang et al., 2001; Ingleby and Crowe, 1999). Partial least squares regression (PLSR), principal component regression, and stepwise multiple linear regression are commonly used methods to determine SOC from these spectral bands (Escandar et al., 2006; Ge et al., 2011; Viscarra Rossel, 2008).

The purpose of the present study is to use information derived from the Vis-NIR technique to decipher the influence of topography and management on SOC variability in two intensively management landscapes with contrasting slope gradients, but similar land-management practices. Specific objectives are to (1) examine the roles of hillslope gradient, soil water content, and bulk density on the spatial variability of SOC in both high- and low-gradient agricultural landscapes, and (2) differentiate the dominant processes controlling SOC heterogeneity in two environments with distinct topographies. By addressing these objectives, the study examines the hypotheses that toeslopes in dissected landscapes with high-gradient hillslopes and spatially continuous drainage pathways exhibit relatively higher spectral absorbances and SOC concentrations compared to summits, as selective erosion translocates organic-rich, fine soil downslope, while topographic depressions in poorly dissected landscapes with gentle hillslopes and poorly defined drainage pathways display higher spectral absorbances and SOC concentrations than surrounding topographic highs, as runoff, fine sediment, and organic matter converge toward the depressions where microbial decomposition is suppressed.

Site Descriptions

Field sites in the Intensively Managed Landscapes Critical Zone Observatory (IML-CZO) (Wilson et al., 2018), namely Clear Creek, IA, and the Upper Sangamon River, IL, were strategically selected to represent the ranges of hillslope gradients and soil properties (e.g., texture, water content, and bulk density) in agricultural landscapes of the U.S. Midwest. The 270-km^2 Clear Creek watershed (41°39ˈ - 41°46ˈ N, 92°00ˈ - 91°36ˈ W) is located in southeast Iowa (Figure 2-2a), and the 2400-km^2 Upper Sangamon watershed (39°37ˈ - 40°33ˈ N, 89°25ˈ - 88°08ˈ W) is in central Illinois (Figure 2-2b). Detailed descriptions of both sites can be found in Wilson et al. (2018). Both watersheds have continental climates characterized by wet springs, hot summers with mesoscale convective storms, relatively dry falls with freeze-thaw cycles, and cold winters with snowfall. The two rainfed watersheds have similar mean annual temperatures (9~11℃) and average amounts of precipitation (889~1000 mm) (Wilson et al., 2018).

Historically, a prairie-savanna, forest-wetland mosaic developed following deglaciation, facilitating the accumulation of organic matter (Kumar et al., 2018). The

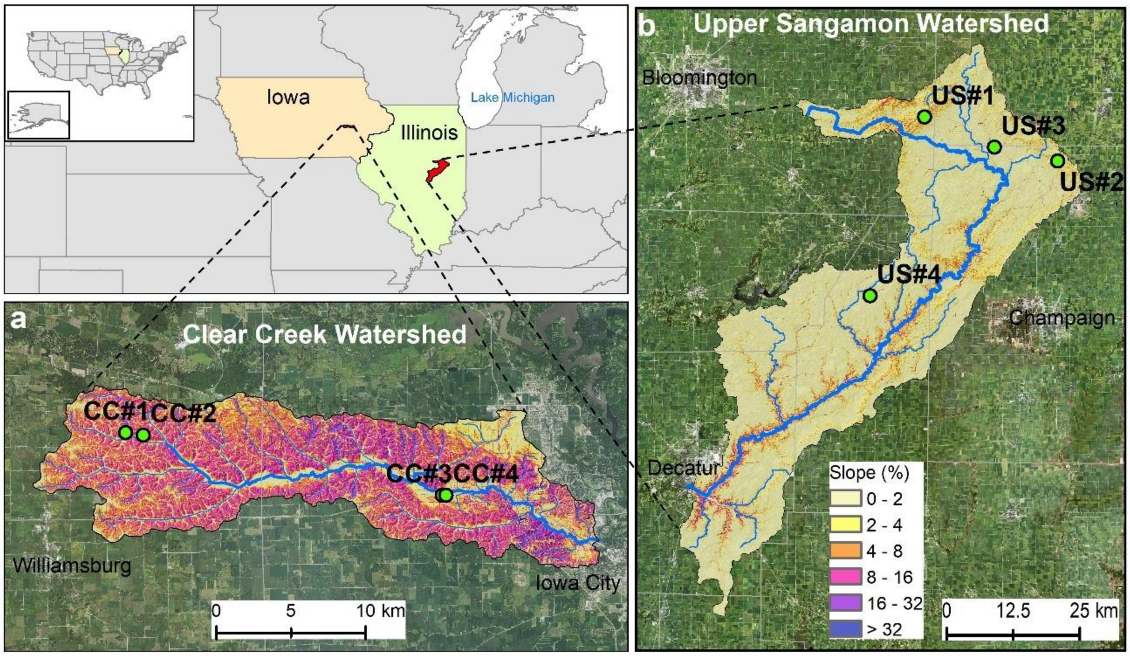

Figure 2-2. Geographic locations and slopes of the two study watersheds. (a) Cleek Creek watershed is located in southeast Iowa with sites CC#1 and CC#2 at the headwaters and sites CC#3 and CC#4 at the lower reaches. Upland slope mostly ranges from 4% to 16%; (b) The Upper Sangamon watershed is located in central Illinois with sites US#1 and US#2 on the sloping uplands and sites US#3 and US#4 on the morainal plains. Upland slope falls in the range of 0-2%.

resulting soils are loess-derived Mollisols and Alfisols (Anders et al., 2018). The most common soil associations in Clear Creek are the well-drained Tama-Fayette-Downs in uplands and poorly-drained Colo-Nevin-Nodaway in lowlands (Wilson et al., 2016). The predominant soil associations in the Upper Sangamon include poorly-drained Drummer-Sable and somewhat poorly-drained Flanagan-Ipava (USDA, 1982). Intensive agriculture was introduced in the region around 1820 (Rhoads et al., 2016) with most land presently devoted to corn (*Zea mays*) and soybean (*Glycine max*) production. Conventional tillage is often implemented at flat sites to dry and aerate the soil, while conservation reduced/no-tillage practices are usually adopted on steeper slopes to reduce soil erosion (Table 2-1). These practices have been used since the early 1990s in both watersheds with only slight differences in the timing of implementation (Papanicolaou et al., 2015).

Despite similarities in land use, the two watersheds differ topographically because of differences in their glacial histories. Clear Creek (Figure 2-2a) was glaciated during the pre-Illinois Episode (~0.5-2.4 Ma), and a long period of fluvioglacial processes left a relatively high-gradient landscape characterized by rolling relief and well-connected surface drainage networks (Bettis et al., 2003). The Upper Sangamon watershed (Figure 2-2b) was glaciated multiple times, most recently during the Wisconsin Glacial Episode (~25-75 ka), leaving a low-gradient landscape with numerous upland closed depressions (Figure 2-1b) and poorly-integrated upland drainage networks (Anders et al., 2018).

Materials and Methods

The methodological procedure for this study (Figure 2-3) involves the following steps: (1) collection of soil samples from fields with varied hillslope gradients, HG, following a grid design (Wilson et al., 2018); (2) laboratory analysis of soil gravimetric water content, GWC, and bulk density, BD, using established methods (Wilson et al., 2018); (3) measurements of Vis-NIR absorption spectra on dry soil samples following the RaCA protocol (Wills et al., 2014); (4) mathematical preprocessing of the spectral data (Zou et al., 2010); (5) calibration and validation of the Vis-NIR models using PLSR analysis; and (6) statistical analyses to identify the interdependence between SOC and hillslope gradient, soil water content, and soil bulk density.

Soil Sampling

Four representative fields were selected that cover the topographic range in each watershed. In Clear Creek (Figure 2-4a), two fields were selected in the rolling headwaters with steeper slopes (CC#1 & CC#2) and two fields were in the lower reaches with gentler slopes (CC#3 & CC#4). For the Upper Sangamon (Figure 2-4b), two fields were selected in the headwaters (US#1& US#2) and two fields were on the morainal plains (US#3 & US#4), all of which with low hillslope gradients.

The field sampling followed a grid composed of four hillslope positions (i.e., summit, shoulder, backslope, and toeslope) and three downslope transects with a minimum of 30 m spacing between each (Figure 2-4). Each downslope transect was aligned following

Table 2-1. General site characteristics.

Properties	Clear Creek Sites				Upper Sangamon Sites			
	CC#1	CC#2	CC#3	CC#4	US#1	US#2	US#3	US#4
Latitude (°)	41.738	41.737	41.699	41.698	40.444	40.374	40.396	40.149
Longitude (°)	-91.941	-91.928	-91.688	-91.685	-88.480	-88.194	-88.329	-88.59
Elevation (m)	239-261	237-243	210-211	210-211	259-265	231-233	218-219	216-217
Size (m^2)	51228	24017	11819	8904	9215	3280	8206	6723
Slope length (m)	342	166	120	118	111	90	95	92
Slope gradient (%)	5.74	3.44	1.39	0.84	3.45	2.57	0.8	0.1
Soil texture	SiCL	SiCL	SiL	SiL	SiL	SiL	CL	SiL
Current tillage	RT	NT	CT	CT	NT	NT	CT	CT
Associated crop	Corn	Bean	Corn	Corn	Corn	Bean	Corn	Corn
No. of samples	48	48	48	48	48	48	48	48

SiCL: silty clay loam; SiL: silt loam; CL: clay loam; RT: reduced tillage; NT: no-till; CT: conventional tillage.

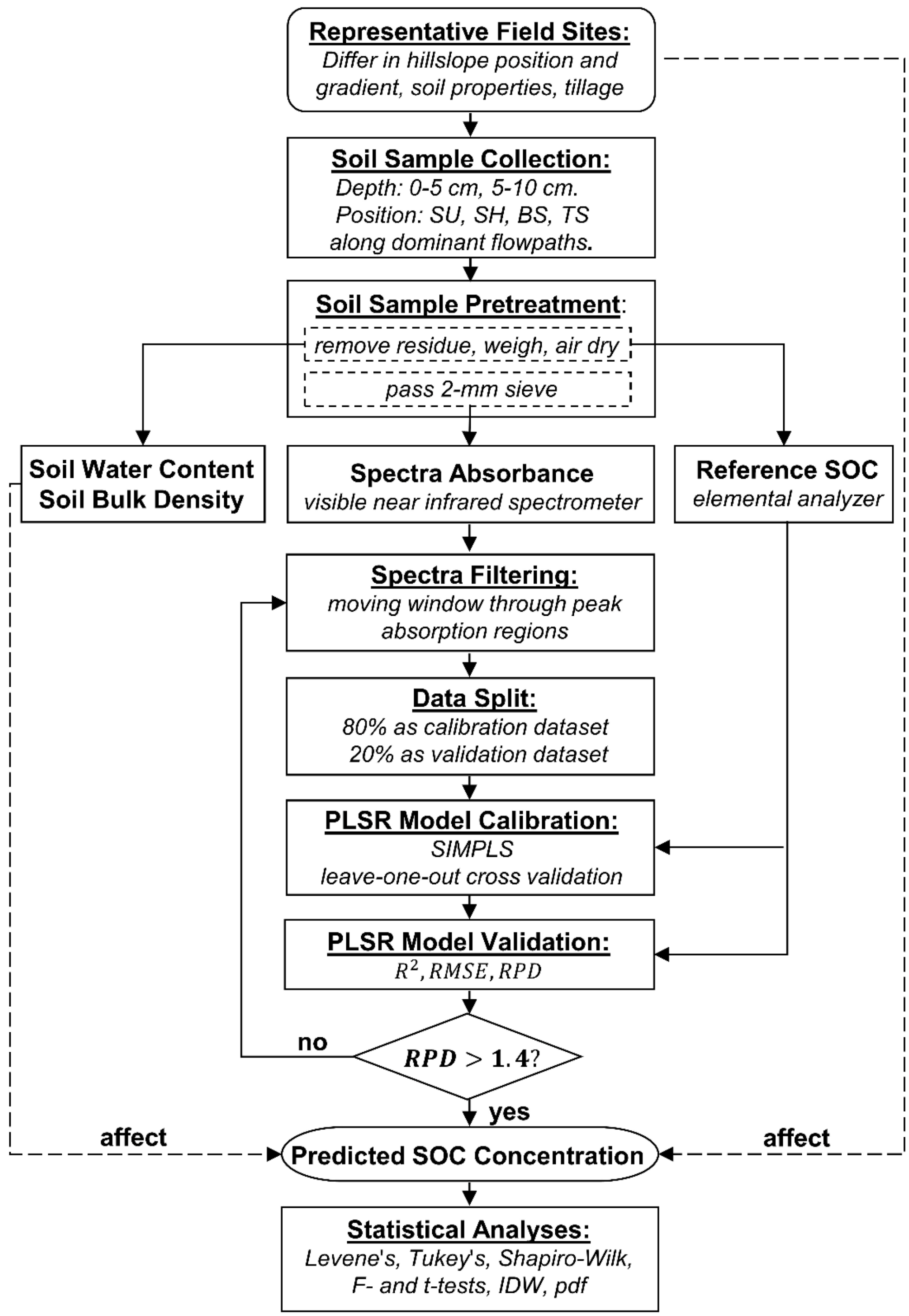

Figure 2-3. Schematic overview of the sequential procedure in this study. SU: summit; SH: shoulder; BS: backslope; TS: toeslope; R^2: coefficient of determination; RMSE: root means squares error; RPD: residual predictive deviation; IDW: inverse distance weighting; pdf: probability density function.

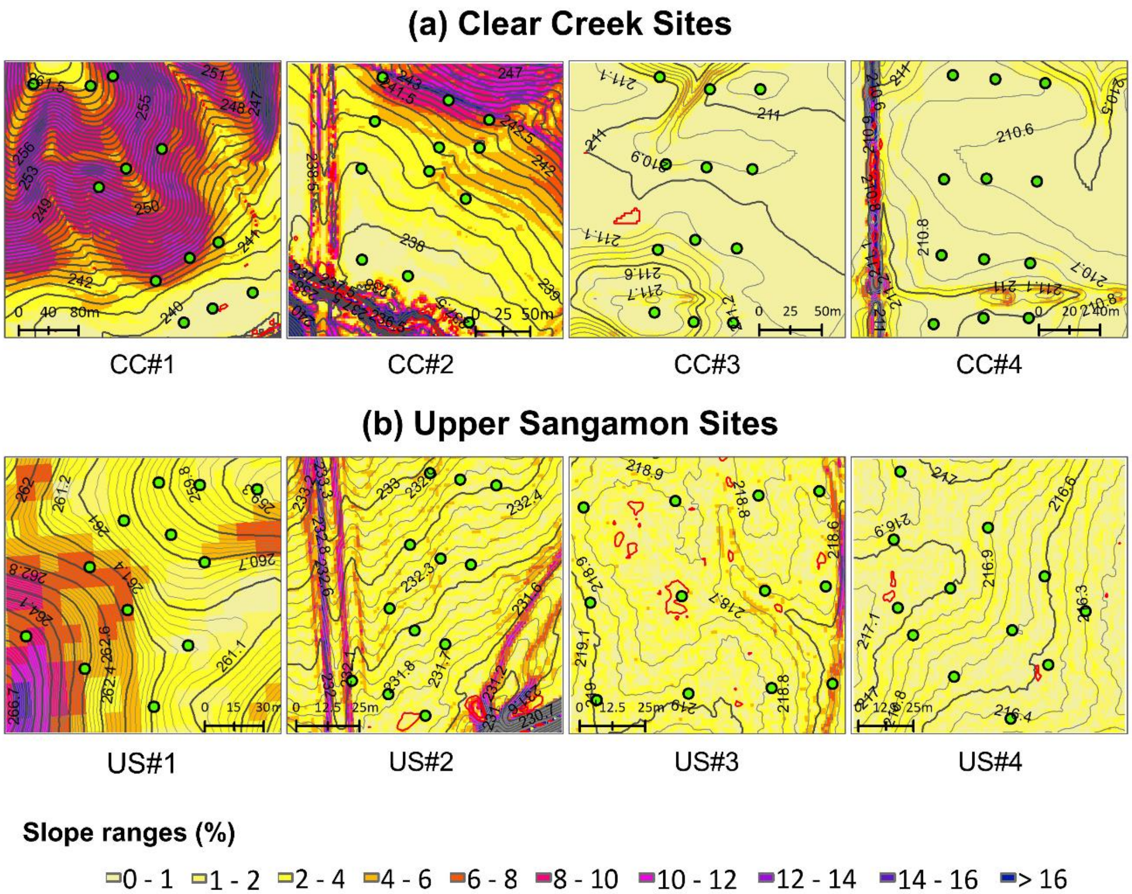

Figure 2-4. Contour and slope maps of the study fields. (a) In Cleek Creek, sites CC#1 and CC#2 have higher hillslope gradients (2-14%) than sites CC#3 and CC#4 (2-6%); (b) In the Upper Sangamon watershed, sites US#1 and US#2 have slightly higher slopes (2-6%) than sites US#3 and Us#4 (0-2%). Red polygons denote the topographic depressions and green dots show the sampling locations. The contour interval is 0.1 m.

primary overland flow pathways delineated using LiDAR-derived elevation data and hydrology tools in ArcGIS (Jenson and Domingue, 1988). Hence, the sampling implicitly accounts for the role of surface runoff and soil water content on SOC variability at different hillslope positions with varying ranges of slope. It also allows for sampling inside the depressions to evaluate their influences on SOC variability.

At the grid intersections, soil samples from depths of 0-5 cm and 5-10 cm were excavated with a ring (5.08 cm [d] x 5.08 cm [h]) for bulk density measurements (USDA, 1996). Replicate samples were taken from each location and depth with a steel scoop (5 cm [l] x 5 cm [w)] x 5 cm [h]) for SOC and gravimetric water content analyses. A total of 384 soil samples were used in this study.

Sample Analyses

The field-moist soil samples were sieved with 8-mm screens to remove stones and large residue. The sieved samples were weighed wet and then air-dried to constant weights (Hou et al., 2018; Li et al., 2020). The soil bulk density was calculated as the ratio of dry soil mass to the volume of the sampled soil defined by the ring. The gravimetric water content was calculated as the ratio of water mass to the dry soil mass. The subsamples were lightly crushed using a wooden rolling pin and passed through a 2-mm sieve to ensure constant particle size effects (e.g., scattering) on the Vis-NIR spectra following the RaCA protocol (Wills et al., 2014). A 0.5-g split of the subsamples was analyzed using the Sercon Ltd. (Crewe, UK) flash combustion elemental analyzer to provide the reference SOC concentration (Hou et al., 2018; Li et al., 2020) for the Vis-NIR model calibration and validation.

Vis-NIR Spectra Measurements

Absorption spectra of the dry soil samples were measured over the Vis-NIR region (350-2500 nm) using a portable ASD LabSpec® 2500 spectrometer (Boulder, CO, USA). The spectrometer connects to a light source through a fiber optic cable and communicates with the controlling computer through an Ethernet interface (Figure 2-5). when making measurements, the room was darkened to minimize background irradiance. This spectrometer combines three separate holographic diffraction gratings with three separate detectors to cover the solar reflected portion of the electromagnetic spectrum between 350 nm and 2500 nm, with a sampling interval of 1.4 nm in the 350-1000 nm region and 2 nm in the 1000-2500 nm region.

Approximately 10 g of soil were loaded inside a circular holder with glass base (3.2 cm [d] x 1.5 cm [h]) and then exposed to the light source for 30 seconds. Each soil sample was scanned three times to facilitate the assessment of sampling error (Henderson et al., 1992). An averaged signal spectrum with an average deviation of 0.06 was developed from the three scans for subsequent analysis. The spectral absorbance was calibrated to white reference using a circular panel (3 cm [d] x 1.1 cm [h]). Soil samples from the two study watersheds had the same reference and QA/QC samples to maintain consistency

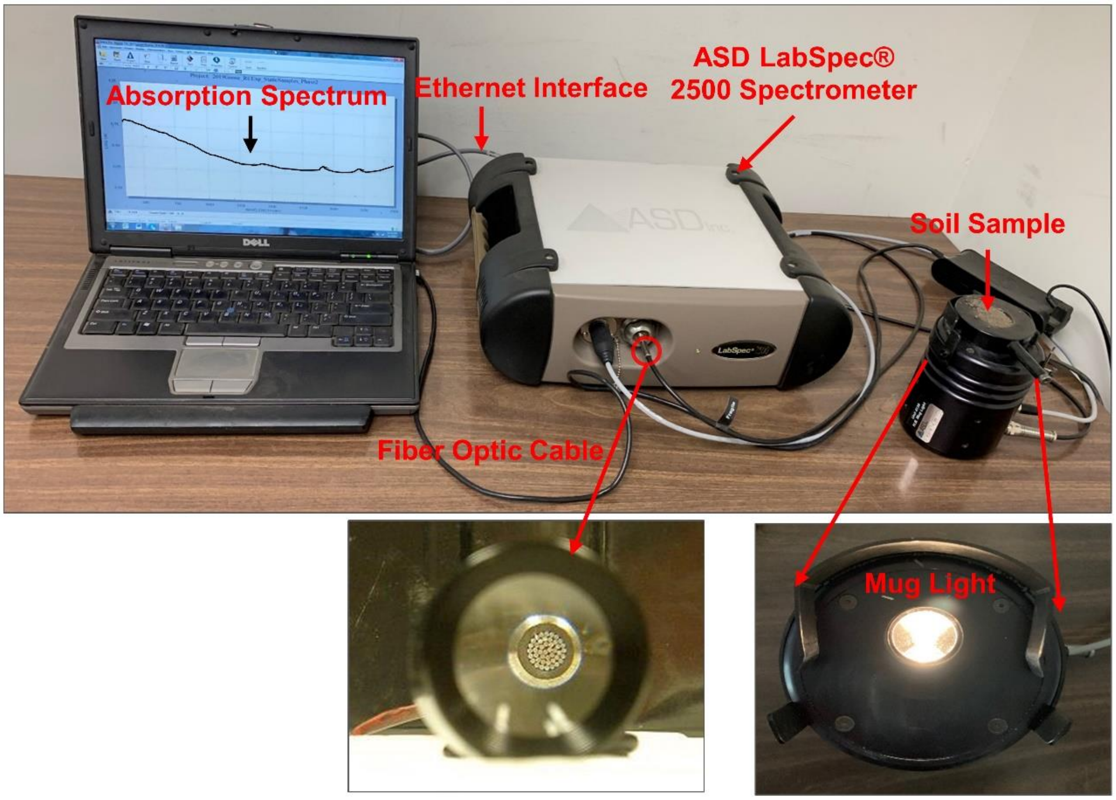

Figure 2-5. Vis-NIR spectrometer setup for measuring soil spectra.

and comparability across regions.

Spectra Preprocessing

The use of spectral transformations enhances the chemical absorption peaks and reduces the effects of random noise, baseline drift, and soil structure variations, all of which in turn affect the accuracy and robustness of model calibration (Ge et al., 2011; Wang et al., 2017). The first derivative transformation was used in this study (Chang et al., 2005; Ge et al., 2011). To obtain explanatory variables, the spectral absorbances in the visible range (450-700 nm) were filtered with a 3-nm moving window due to their high vibration frequency, and the spectral absorbances in the near-infrared range (950-1050 nm, 1300-1500 nm, 1846-2500 nm) were filtered with a 5-nm moving window, reducing the number of wavelengths from 2151 to 276 (Zou et al., 2010).

PLSR Model Calibration and Validation

PLSR has proven robust for predicting a set of soil-property response variables from large sets of spectral-absorbance predictor variables (Stenberg et al., 2010; Viscarra Rossel, 2008). PLSR analysis decomposes latent variables from the predictor variables, x (i.e., spectral absorbance bands) and the response variables, y (i.e., SOC) by selecting orthogonal factors that maximize the covariance as well as explain most of the variation both in predictors and in responses (Viscarra Rossel, 2008). More details about the PLSR method can be found in Martens and Nï (1992).

Before conducting PLSR analysis, the soil samples were divided into two groups, with 80% being used for calibration and 20% being used for validation (Wang et al., 2017). A stepwise partitioning scheme (Galvao et al., 2005) was used to divide the data, where every sixth observation was used for the validation dataset. The calibration was implemented using the SIMPLS algorithm in JMP Pro 14 (Cox and Gaudard, 2013). The calibrated equation was then used to determine SOC content for the samples in the validation dataset based on their spectral analysis. Leave-one-out cross-validation (Conforti et al., 2013) with as many as 15 orthogonal factors was adopted during the PLSR analysis. The number of orthogonal factors with minimum root mean PRESS (predicted residual error sum of squares) was chosen as the optimal number of latent variables.

Model efficiency was evaluated using the coefficient of determination (R^2), the root mean square error (RMSE), and the residual predictive deviation (RPD). RPD is defined as the ratio of the standard deviation of the elemental analyzer measured SOC values to the RMSE (Conforti et al., 2013). According to Chang et al. (2001), model performance in terms of predictability was assessed based on RPD values, which are classified as unsuccessful if RPD < 1.4, moderately successful if $1.4 \leq$ RPD ≤ 2, and successful if RPD > 2. The PLSR models were separately developed for the Clear Creek and Upper Sangamon datasets.

Statistical Analyses

Levene's test was used for testing homogeneity of variance (Levene, 1961), and Tukey's HSD (honestly significant difference) test was used for identifying significant differences amongst the means of the four site-groups within each watershed (Keselman and Rogan, 1977). The Shapiro-Wilk test was used to assess the normality of SOC concentration (sample size < 200) (Razali and Wah, 2011). Fisher-Snedecor (F) test was used for testing equality of variance, and Student's t-test was used for testing significant differences between the means of the two watersheds. All statistical tests were accomplished using SAS Enterprise Guide 7.1, at a significance level of 0.05. SOC maps were generated using the geostatistical toolsets in ArcGIS 10.6.1. The SOC concentrations between sampling points were interpolated using the inverse distance weighting (IDW) algorithm (Schloeder et al., 2001). Probability density functions (pdfs) of SOC concentrations were generated to facilitate the comparison of SOC variability between the two watersheds. The central and dispersion trends of SOC pdfs were described using traditional statistical parameters: mean, standard deviation, minimum, maximum, the coefficient of variation, kurtosis, and skewness.

Results

Spectra Analyses and PLSR Predictions

The spectral absorbances of all soil samples varied from 0.21 to 0.97 (Figure 2-6a and c) following the same basic shape as also seen by other researchers (Chang et al., 2001; Katuwal et al., 2018; Viscarra Rossel et al., 2016). There was an absorption plateau between 400-700 nm that corresponds with iron oxides and N-H bonds (Figure 2-6a and c). Absorbance spikes were near 1400 nm, 1900 nm, and 2200 nm, and these wavelengths are associated with clay minerals and O-H bonds of free water (Viscarra Rossel et al., 2006). The rising absorbances from 2300-2400 nm capture the C-H bonds showing enrichment of organic matter (Katuwal et al., 2018). These absorbance peaks were significantly enhanced by the first derivative transformations (Figure 2-6b and d). Soil from Clear Creek exhibited less variability in spectral absorbances than soil from the Upper Sangamon watershed, which was seen with less extensive spread amongst different topographic locations. Within each watershed, soil from the summit generally had lower spectral absorbances than soil from the toeslopes. Soil from steeper sites showed lower absorbances than soil from gentler sites.

A linear relationship was developed between the measured SOC concentrations of sample splits using the elemental analyzer and the corresponding spectral absorbances (Figure 2-7 and Figure 2-8). For the Clear Creek dataset, a strong calibration was obtained for the 0-5 cm samples with 12 latent variables (PRESS = 0.8). A relatively weaker calibration was obtained for the 5-10 cm samples with four latent variables (PRESS = 1.13). For the Upper Sangamon dataset, good calibrations were obtained for 0-5 cm and 5-10 cm samples with five optimal latent variables identified for both models

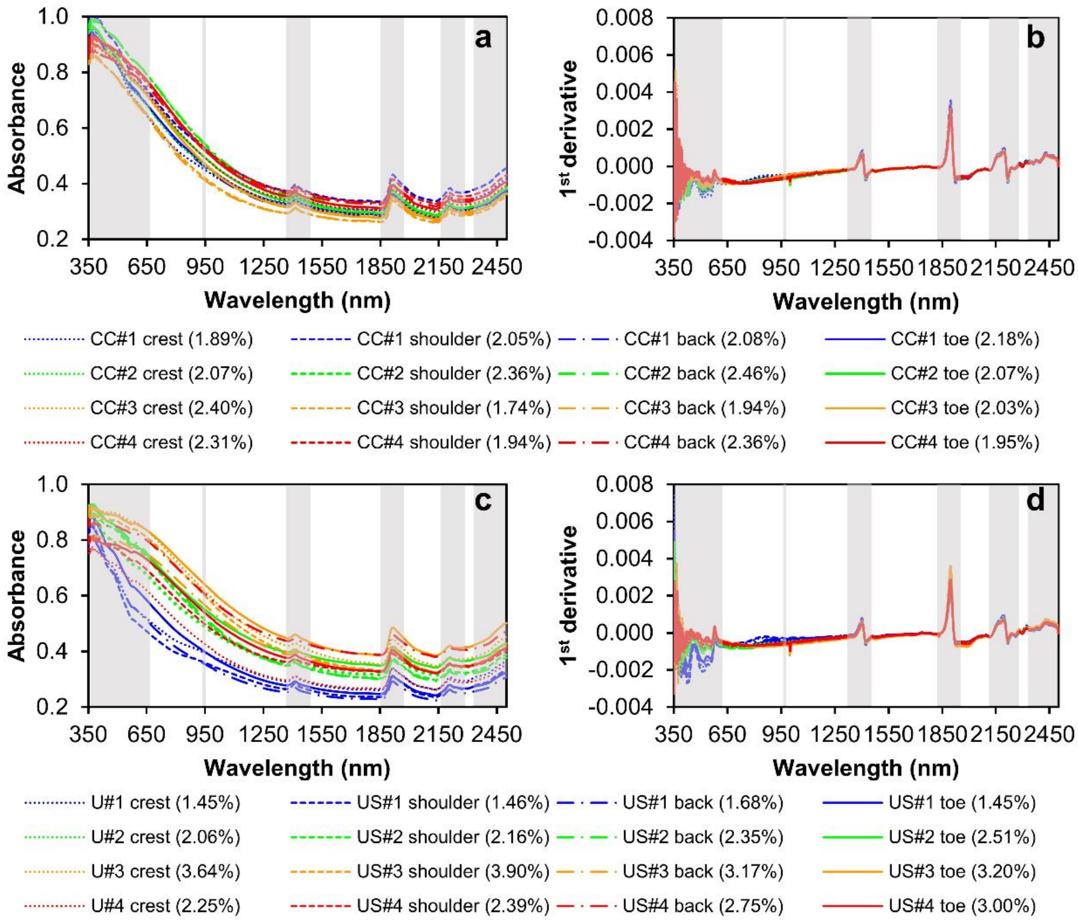

Figure 2-6. Absorbance spectra and first derivative transform of soil at the field summit (SU), shoulder (SH), backslope (BS), and toeslope (TS) in (a, b) Clear Creek and (c, d) the Upper Sangamon watershed. Numbers in parenthesis are SOC concentrations measured by elemental analyzer using the identical soil samples. Gray bars denote the absorbance spikes associated with iron oxides, water/clay minerals, and organic matter. Presented here is the spectra of soil at 0-5 cm which is in the same shape as soil at 5-10 cm.

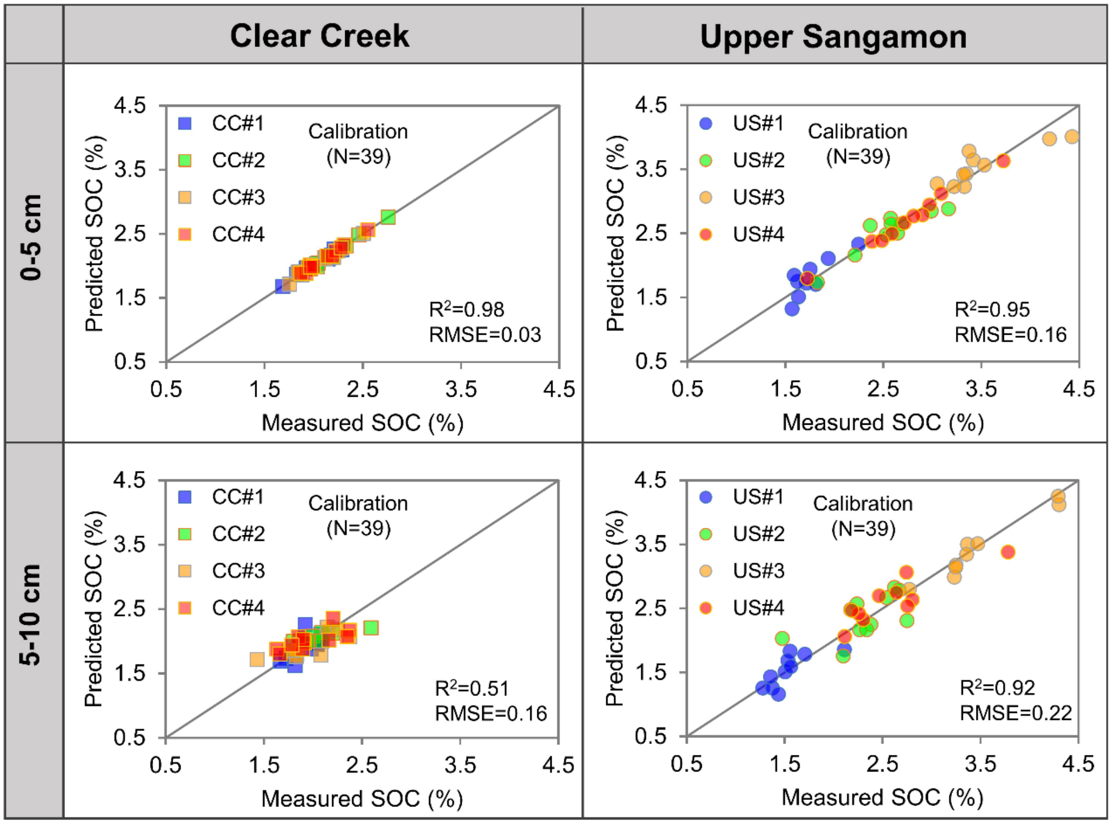

Figure 2-7. Scatter plots of elemental analyzer measured SOC against Vis-NIR predicted SOC in calibration via PLSR approach for Clear Creek soil from0-5 cm and 5-10 cm, and for the Upper Sangamon soil from 0-5 cm and 5-10 cm. The 1:1 line is indicated in each plot.

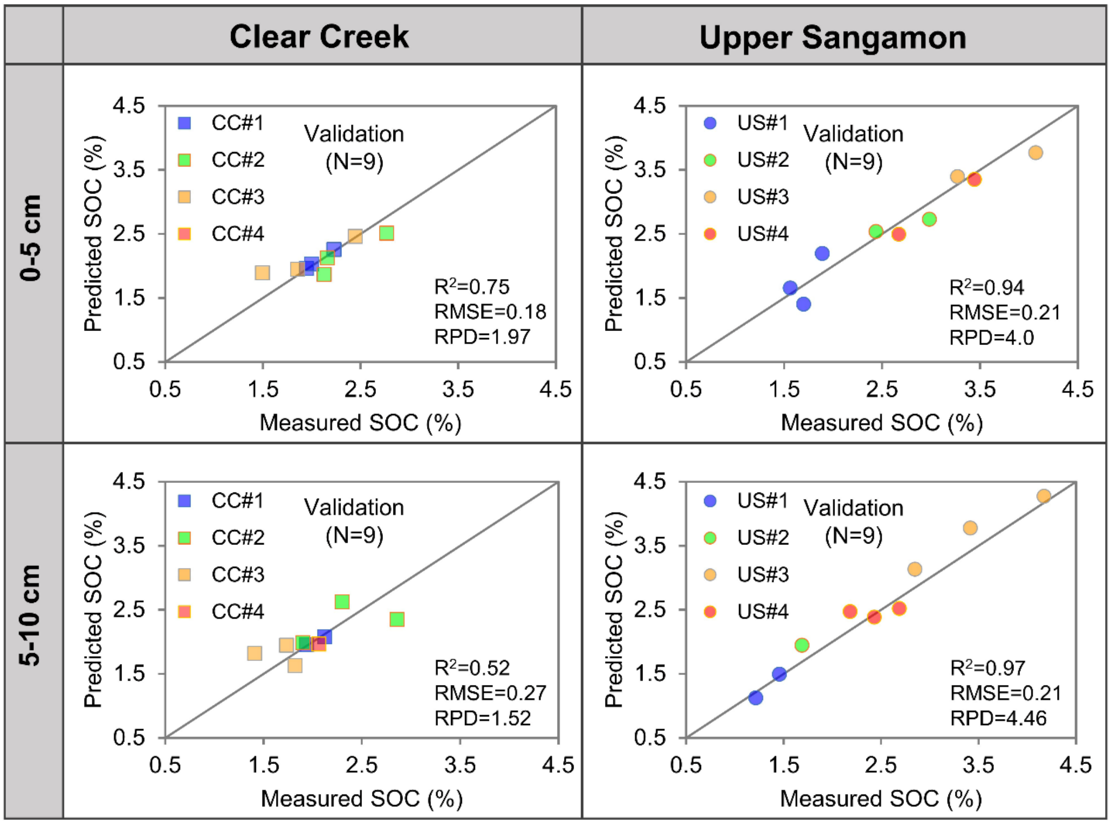

Figure 2-8. Scatter plots of elemental analyzer measured SOC against Vis-NIR predicted SOC in validation via PLSR approach for Clear Creek soil from 0-5 cm and 5-10 cm, and for the Upper Sangamon soil from 0-5 cm and 5-10 cm. The 1:1 line is indicated in each plot.

(PRESS = 0.27). In Clear Creek, validation results for the 0-5 cm and 5-10 cm samples were acceptable. In the Upper Sangamon, model performances on the 0-5 cm and 5-10 cm samples were also good. Thus, values derived from either PLSR analysis were judged to be reliable for evaluating SOC variability in these watersheds.

Statistical Properties of SOC Concentrations

The four Clear Creek sites had similar mean SOC concentrations at 0-5 cm with an average of 2.11% ± 0.23% and at 5-10 cm with an average of 1.99% ± 0.19% (Figure 2-9a). However, the four Upper Sangamon sites had significantly ($P < 0.0001$) different SOC concentrations at both depths (Figure 2-9b). The highest SOC concentration was found at site US#3 with an average of 3.56% ± 0.28% at 0-5 cm and 3.50% ± 0.50% at 5-10 cm. The lowest SOC concentration was at site US#1 with an average of 1.79% ± 0.31% at 0-5 cm and 1.50% ± 0.26% at 5-10 cm. Sites US#2 and US#4 had similar, intermediate SOC concentrations at both depths with averages of 2.64% ± 0.42% at 0-5 cm and 2.45% ± 0.36% at 5-10 cm.

For both depths, the site-averaged SOC concentrations in the Upper Sangamon watershed were 25% higher than the corresponding site-averaged SOC concentrations in Clear Creek ($P < 0.0001$; t-Test). At 0-5 cm, the Upper Sangamon locations had average concentrations of 2.66% ± 0.72%, compared to 2.11% ± 0.23% in Clear Creek. For 5-10 cm, the Upper Sangamon sites had average concentrations of 2.48% ± 0.81%, compared to 1.99% ± 0.19% in Clear Creek. All field sites exhibited higher averaged SOC concentrations at 0-5 cm than at 5-10 cm, but there was a greater decrease in mean SOC concentrations with depth for the Upper Sangamon sites ($P < 0.001$) than for the Clear Creek sites ($P = 0.01$).

Factors Controlling SOC Variability

Hillslope Gradient

Hillslope gradient (HG) showed different variability within each watershed. In Clear Creek, the headwater sites CC#1 (5.74%) and CC#2 (3.44%) had significantly ($P=0.0002$) higher mean HG than the lower reach sites of CC#3 (1.39%) and CC#4 (0.84%) (Figure 2-9c). In the Upper Sangamon watershed, however, all sites had statistically similar mean HG values ranging from 0.1% to 3.45% (Figure 2-9d). In both IMLs, HG was inversely related to SOC concentration, but to different degrees. In Clear Creek, as the mean decreased from 6% to 0.8% moving from the headwaters to the mouth locations, the corresponding average SOC concentration increased slightly from 2.06% to 2.12%. In the Upper Sangamon watershed, however, as the mean HG decreased from 3% to 0.1% from the sloping uplands to the depressional lowlands, the average SOC concentration increased from 1.5% to 3.5%.

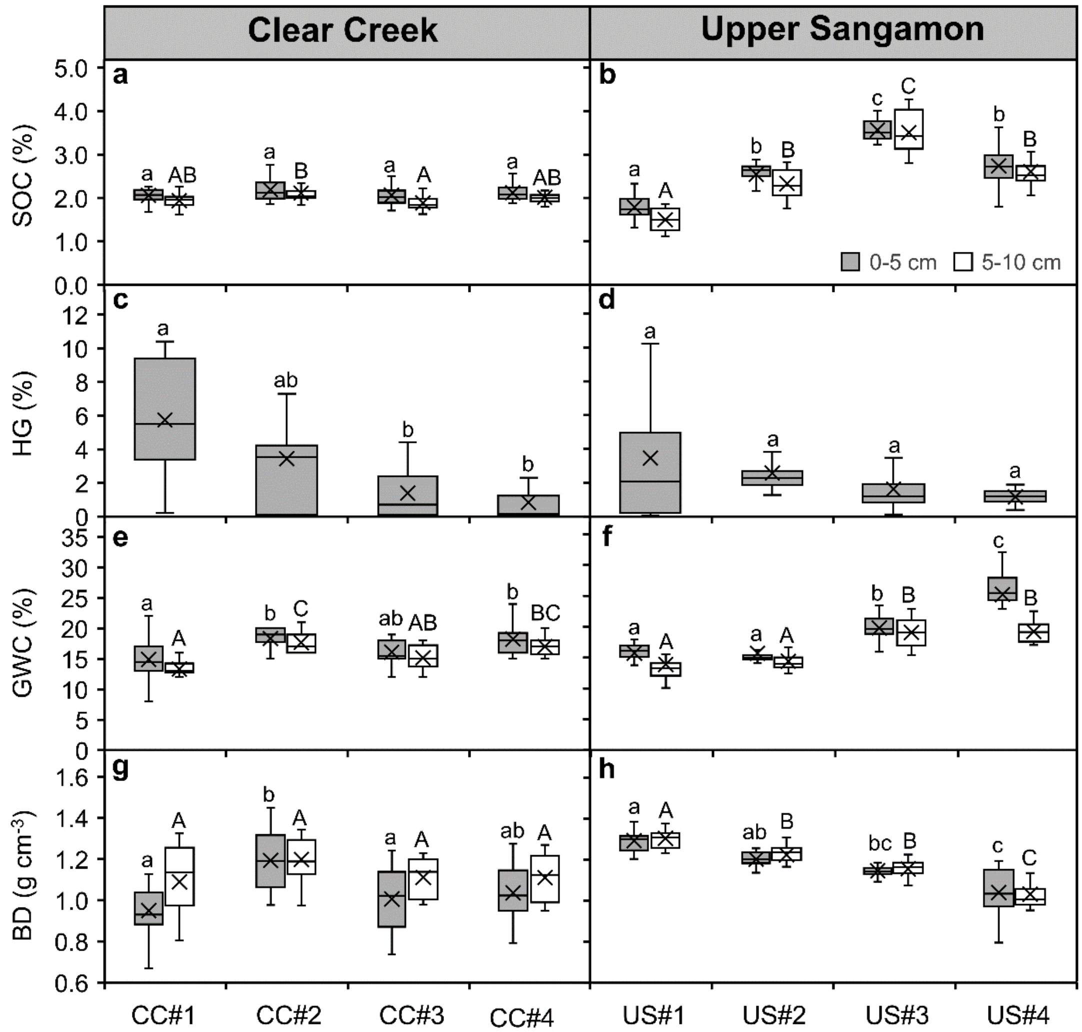

Figure 2-9. Range, median, and mean of (a, b) SOC, (c, d) hillslope gradient (HG), (e, f) gravimetric water content (GWC), and (g, h) bulk density (BD) in Clear Creek field sites and the Upper Sangamon field sites. For each variable, the plot represents min and max values as whiskers, the range of 25% and 75% quartiles as box, the median as the middle line, and the mean as the 'x' mark. Different lowercase/uppercase letters represent significant differences in mean values between field sites from 0-5 cm/5-10 cm depths, using Tukey's HSD test at α=0.05.

Gravimetric Water Content

Similar to the SOC concentrations, the 0-5 cm soil from all locations had higher gravimetric water content (GWC) (Clear Creek: 17% ± 3%; Upper Sangamon: 19% ± 5%) than the soil at 5-10 cm (Clear Creek: 16% ± 3%; Upper Sangamon: 17% ± 4%) (Figure 2-9e and f). In Clear Creek, specifically, the lower reach sites of CC#3 and CC#4 had slightly higher mean GWC (17% ± 3% at 0-5 cm; 16% ± 2% at 5-10 cm) than one of the headwater sites CC#1 (15% ± 4% at 0-5 cm; 13% ± 2% at 5-10 cm). In the Upper Sangamon watershed, the lower-gradient sites on the morainal plain, US#3 (20% ± 2% at 0-5 cm; 19 ± 3% at 5-0 cm) and US#4 (25% ± 6% at 0-5 cm; 19% ± 2% at 5-10 cm) had significantly higher GWC than the more sloping sites of US#1 and US#2 (16% ± 2% at 0-5 cm; 14% ± 3% at 5-10 cm).

Bulk Density

The sampling locations in both watersheds showed similar mean bulk density (BD) of dry soil at 0-5 cm and 5-10 cm (Table 2-2). However, a correspondence existed in both watersheds between BD and most recent tillage practices. In Clear Creek, higher BD at 0-5 cm was measured at the no-tillage site CC#2 with a mean of 1.19 g cm^{-3}, while lower mean BD values were measured at the tilled sites of CC#1 (0.95 g cm^{-3}), CC#3 (1.01 g cm^{-3}), and CC#4 (1.04 g cm^{-3}). At 5-10 cm, no significant differences in BD were found between the four fields (Figure 2-9g). For both sampling depths in the Upper Sangamon watershed, higher mean BD values were also measured at the no-till sites of US#1 and US#2 (Figure 2-9h), compared to the tilled sites of US#3 and US#4 ($P < 0.0001$; Tukey's HSD).

Analysis of Principal Factors

To understand further how HG, GWC, and BD relate to the variability of SOC concentrations in the two watersheds, the principal component analysis (PCA) was conducted to summarize the major patterns of variation (Figure 2-10). The first (PC1 = 42.2%) and second (PC2 = 24.7%) principal components accounted for 66.9% of the total variation in the variables, having similar weights (-3 to 3) on PC1 but clear partitioning of Clear Creek samples from Upper Sangamon samples on PC2. On PC2, Clear Creek samples had negative weights (-3 to 0), whereas Upper Sangamon samples had positive weights (0 to 2). HG had a negative weight (-3.4) on PC1 and a negative correlation with SOC, with soil samples being mainly from Clear Creek. GWC had a positive weight (4.8) on PC1 and was positively correlated with SOC, with soil samples being primarily from the Upper Sangamon. BD had a positive weight (5) on PC2 and a negative correlation with SOC, with soil samples being mainly from the Upper Sangamon. Meanwhile, negative associations existed among HG, GWC, and BD. The PCA biplot shows that for the higher-gradient Clear Creek, HG accounts for the highest amount of variation in SOC concentrations, while for the lower-gradient Upper Sangamon watershed GWC and BD account for the most variation in SOC.

Table 2-2. Mean and statistical tests of hillslope gradient (HG), SOC concentrations, gravimetric water content (GWC), and bulk density (BD) for the four sites across each watershed.

Properties	Clear Creek Sites						Upper Sangamon Sites					
	CC#1	CC#2	CC#3	CC#4	Levene test P	Tukey test P	US#1	US#2	US#3	US#4	Levene test P	Tukey test P
HG (%)	5.74 (65)	3.44 (98)	1.39 (111)	0.84 (129)	0.002	0.0002	3.45 (123)	2.57 (65)	0.80 (83)	0.10 (39)	<0.0001	0.103
0-5 cm												
SOC (%)	2.06 (8)	2.19 (12)	2.07 (12)	2.12 (10)	0.402	0.464	1.79 (17)	2.54 (12)	3.56 (8)	2.74 (18)	0.332	<0.0001
GWC (%)	15 (24)	18 (10)	16 (13)	18 (14)	0.216	0.005	16 (12)	16 (15)	20 (12)	25 (24)	0.124	<0.0001
BD (g cm^{-3})	0.95 (19)	1.19 (13)	1.01 (17)	1.04 (14)	0.908	0.005	1.29 (4)	1.2 (3)	1.15 (2)	1.04 (12)	<0.0001	<0.0001
5-10 cm												
SOC (%)	1.94 (9)	2.11 (10)	1.89 (10)	2.01 (7)	0.816	0.025	1.50 (17)	2.33 (15)	3.50 (14)	2.60 (13)	0.144	<0.0001
GWC (%)	13 (12)	18 (10)	15 (15)	17 (9)	0.304	<0.0001	14 (28)	14 (10)	19 (14)	19 (9)	0.291	<0.0001
BD (g cm^{-3})	1.09 (16)	1.20 (9)	1.11 (9)	1.11 (10)	0.078	0.180	1.30 (7)	1.20 (5)	1.16 (4)	1.03 (7)	0.228	<0.0001

Numbers in parentheses show the coefficient of variation in % of the respective variables inside the fields.

Levene's test and Tukey's HSD test were conducted at α=0.05.

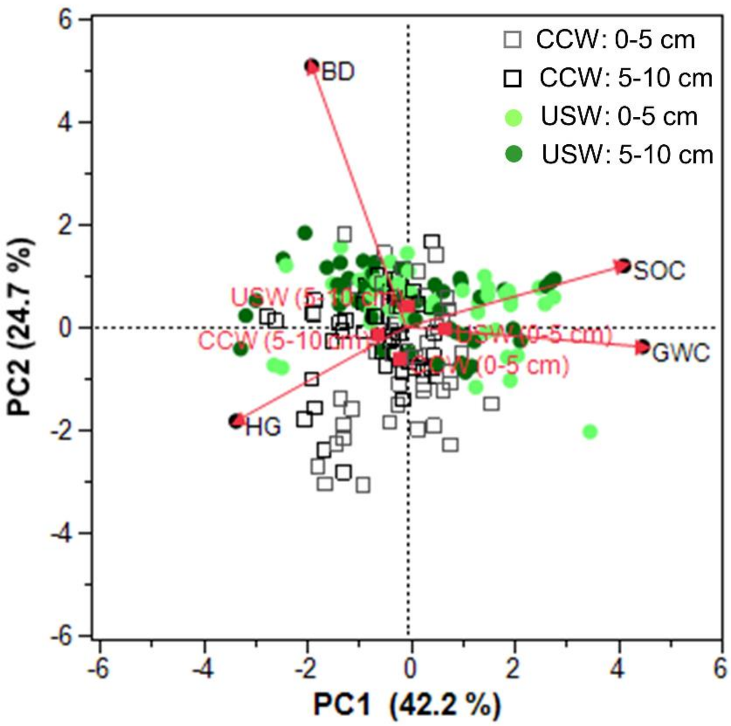

Figure 2-10. Principal component analysis (PCA) scores and vectors of Vis-NIR predicted SOC concentration, hillslope gradient (HG), gravimetric water content (GWC), and bulk density (BD) for Clear Creek watershed (CCW) and Upper Sangamon watershed (USW). Red arrows represent weighting score and correlation between any two variables. Hollow squares represent Clear Creek data at 0-5 cm (gray) and 5-10 cm (black). Solid dots represent Upper Sangamon data at 0-5 cm (light green) an 5-10 cm (dark green).

SOC Variability at the Field Scale

The spatial distributions of SOC in each field were examined using the SOC maps (Figure 2-11). In Clear Creek field CC#1, SOC concentrations increased from 1.88% to 2.18% at 0-5 cm and from 1.68% to 2.04% at 5-10 cm, moving from the summit to the toeslope. Within the less-sloped field CC#2, there were two higher SOC clusters (2.8%) on the sides of the central ridge at backslope, and regions of lower SOC (1.97%) were distributed on the summit and along the central ridge. SOC at 5-10 cm displayed a similar spatial pattern as the upper layer. The fields of CC#3 and CC#4 were less steep, with average slopes of less than 1%. In CC#3, the slightly raised summit displayed higher SOC concentrations at 0-5 cm (2.40%) and 5-10 cm (2.16%) than the rest of the field. In CC#4, higher SOC concentrations (2.25-2.32%) were observed on the slightly raised level summit and gently sunken backslope, and lower SOC concentrations (1.94-2.02%) were found at the relatively gently sloping shoulder and toeslope.

In the Upper Sangamon, US#1 had lower SOC concentrations on the steeper summit and shoulder (1.55-1.72% at 0-5 cm; 1.48-1.53% at 5-10 cm), and higher SOC at the gentler back- and toe-slopes (1.90-1.99% at 0-5 cm; 1.36-1.63% at 5-10 cm). At 0-5 cm of US#2, a local area of low SOC was located at the northeast edge of the field (1.57-2.02%), and higher SOC concentrations were spread throughout the shoulder to the toeslope (2.47-2.92%). At 5-10 cm, lower SOC concentrations extended from the summit to the backslope (1.98-2.17%), and higher SOC levels distributed around the toeslope (2.44-2.73%). The center and northwest corner of US#3 were inlaid with multiple closed depressions. These depressions displayed higher SOC concentrations (3.60-4.27%) than the surrounding higher areas (2.92-3.37%). In contrast to the depth distribution of SOC observed in the non-depression areas, SOC concentrations in the depressions were slightly higher at 5-10 cm (4.2%) than at 0-5 cm (3.8%). In US#4, moving from the summit to the toeslope, SOC concentrations generally increased from 2.22% to 3.18% at 0-5 cm and from 2.41% to 3.05% at 5-10 cm.

SOC Variability at the Watershed Scale

A comparison of the SOC variability was conducted between Clear Creek and the Upper Sangamon using the pdfs (Figure 2-12). Since the field sites are representative of geophysical variations across each watershed, site-combined pdfs of SOC can project the degree of SOC variability at the watershed scale. For both 0-5 cm and 5-10 cm depths, the pdfs of SOC concentrations of the Clear Creek sites exhibited overlapping "wedge" shapes (Figure 2-12a and b), whereas the pdfs of SOC of the Upper Sangamon sites displayed various shapes that covered multiple SOC ranges (Figure 2-12c and d). For Clear Creek, the site-combined pdf of SOC concentrations at both depths followed a sharp "bell" shape symmetrical about the mean values (2.11% at 0-5 cm; 1.99% at 5-10 cm) with narrow spreads (1.68-2.68% at 0-5 cm; 1.62-2.62% at 5-10 cm) (Figure 2-12e and f). The SOC concentrations measured for Clear Creek followed normal distributions, an assessment that was verified by the Shapiro-Wilk normality test (Table 2-3). For the

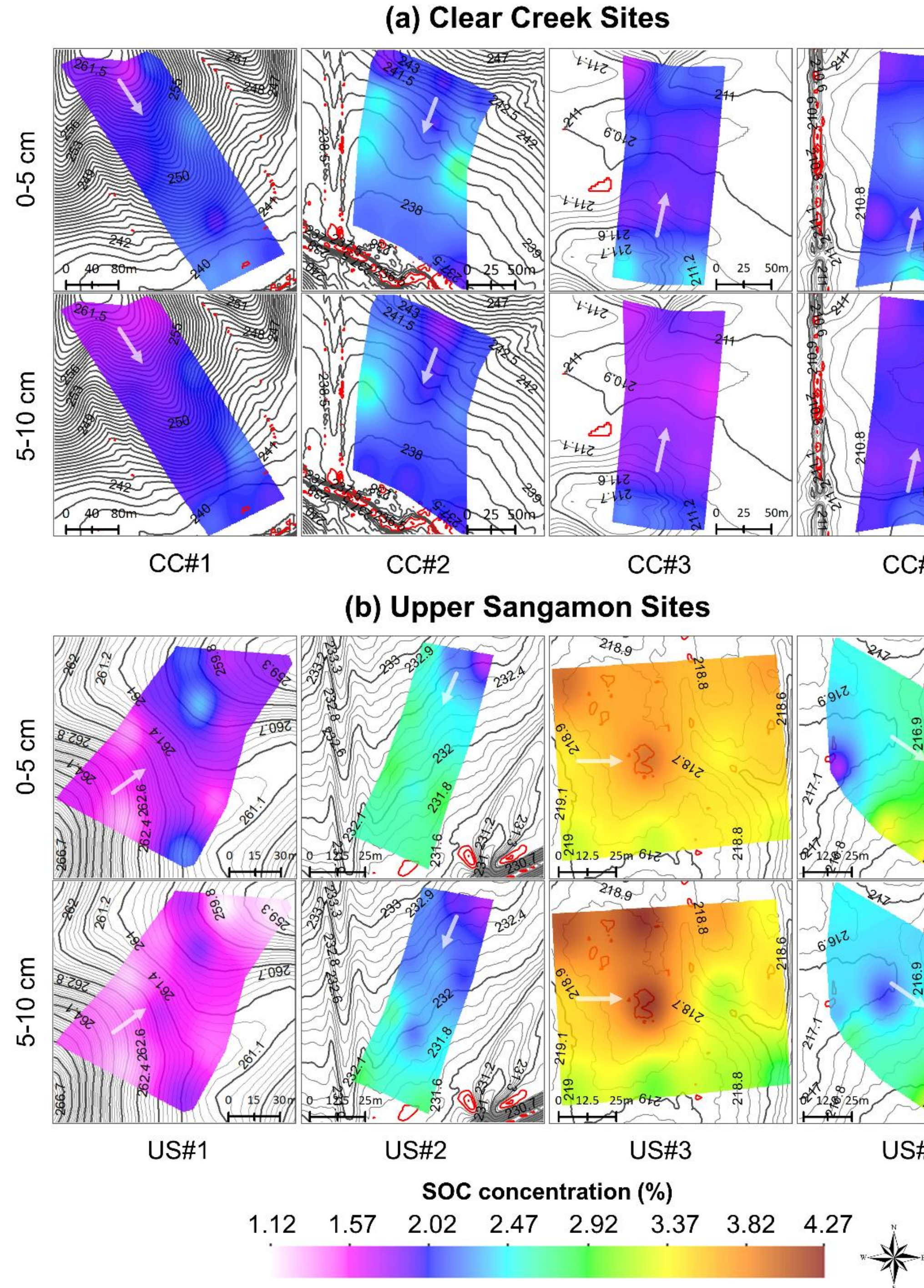

Figure 2-11. SOC maps for (a) Clear Creek fields and (b) Upper Sangamon fields at 0-5 cm and 5-10 cm depths. Red polygons represent topographic depressions and white arrows denote the flow directions. The contour interval is 0.1 m.

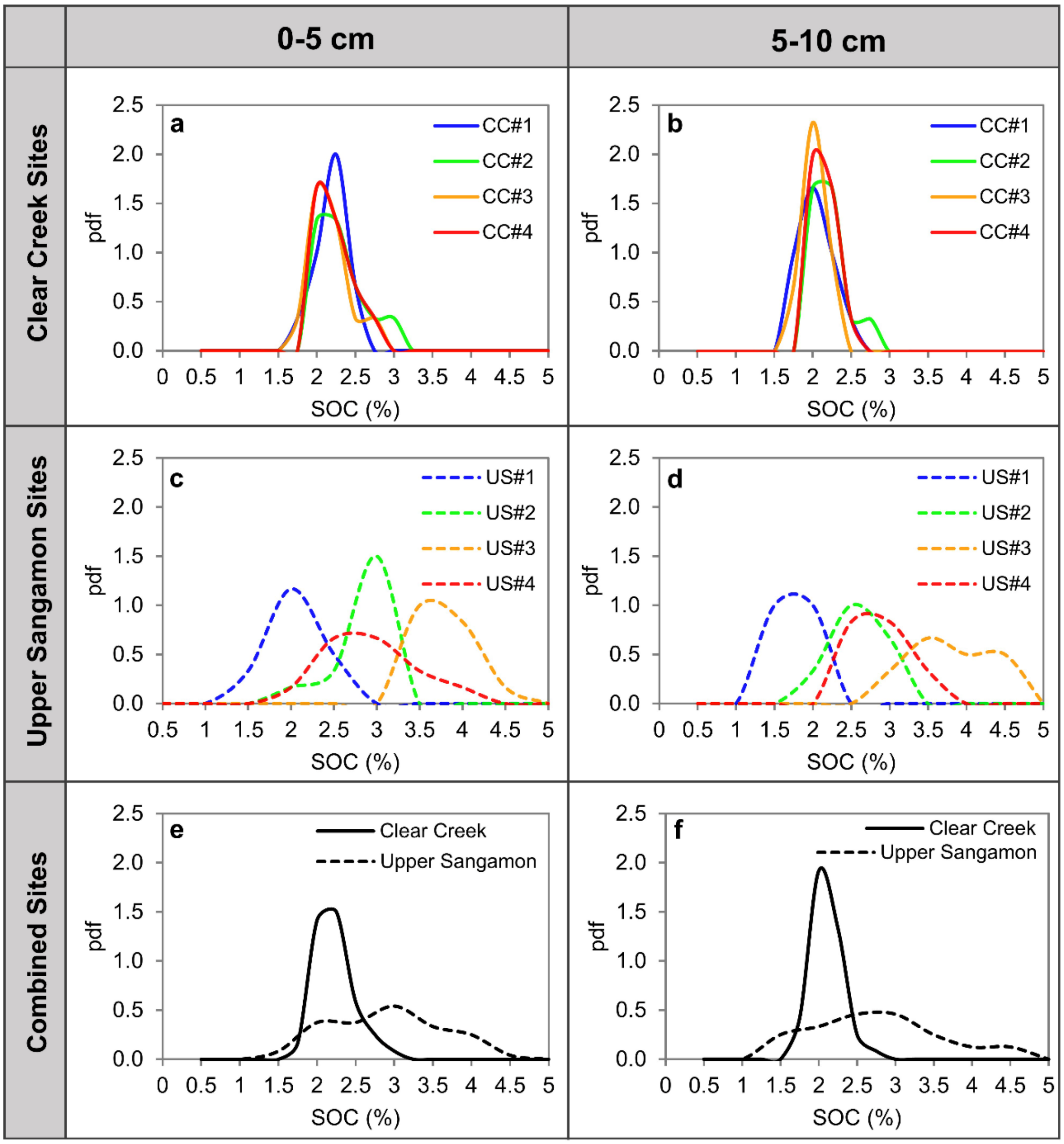

Figure 2-12. Probability density functions (pdfs) of Vis-NIR predicted SOC concentrations for the (a, b) Clear Creek sites, (c, d) Upper Sangamon sites, and (e, f) combined sites, at 0-5 cm and 5-10 cm depths.

Table 2-3. Descriptive statistics of sites-combined SOC concentrations for Clear Creek and the Upper Sangamon watershed at 0-5 cm and 5-10 cm depths.

SOC (%)	0-5 cm				5-10 cm			
	Clear Creek	Upper Sangamon	F-test P	t-test P	Clear Creek	Upper Sangamon	F-test P	t-test P
Mean	2.11	2.66	<0.0001	<0.0001	1.99	2.48	<0.0001	<0.0001
SD	0.23	0.72			0.19	0.81		
Min	1.68	1.32			1.62	1.12		
Max	2.76	4.01			2.62	4.27		
CV	10.90	27.07			9.55	32.66		
Kurt	0.53	-0.88			1.39	-0.34		
Skew	0.70	0.03			0.64	0.35		
Shapiro-Wilk test P	0.079	0.280			0.224	0.384		

SD: standard deviation; Min: minimum; Max: maximum; CV: the coefficient of variation (%); Kurt: kurtosis; Skew: skewness.

F- and t-tests were conducted at α=0.05.

Upper Sangamon watershed, the site-combined pdf of SOC at both depths contained a multimodal distribution with wide spreads (1.32-4.01% at 0-5 cm; 1.12-4.27% at 5-10 cm) (Figure 2-12e and f). The coefficients of variation of SOC concentrations in the Upper Sangamon were 27.07% at 0-5 cm and 32.66% at 5-10 cm, which were roughly two times higher than that in Clear Creek (Table 2-3). The results illustrate that the surface SOC concentrations across the higher-gradient Clear Creek tend to be more homogenous than those of the lower-gradient Upper Sangamon watershed, which are more heterogeneous.

Discussion

SOC stocks in IMLs are governed by carbon inputs via crop biomass production (Kögel-Knabner, 2002) and by carbon losses through decomposition and erosion (Berhe et al., 2018; Doetterl et al., 2016; Kirkels et al., 2014). The decomposition of organic matter is driven mainly by microbial activity and regulated by soil microclimate, namely temperature, soil moisture, and oxygen availability (Kirschbaum, 1995; Sollins et al., 1996; Van Veen and Kuikman, 1990). Soil erosion, although often neglected in SOC budgets (Wilson et al., 2016), is important in IMLs (Papanicolaou et al., 2015). The rate and extent of soil erosion are affected by topography, particularly hillslope gradient and topographic depressions, in combination with rainfall-runoff, soil properties, and land cover/management (Flanagan and Nearing, 1995). Similar climates between the two watersheds examined in the present study, along with similar soil types and land cover/management practices, provided the context for determining the effects of topography on SOC variability. Topography influences water partitioning between runoff and infiltration (Thompson et al., 2010), leading to different rates of transport and transformation of SOC (Yan et al., 2019). Through these effects, topography broadly controls the spatial distribution of SOC concentrations both vertically and laterally through the balance of carbon-loss processes by decomposition and erosion.

Vertical Variability of SOC

In the study fields, the occurrence of higher SOC concentration at 0-5 cm than at 5-10 cm in non-depression locations is consistent with other studies for this region (Harden et al., 2002; Ritchie et al., 2007; Rosenbloom et al., 2006), suggesting the typical exponential decay of SOC with soil depth (Hilinski, 2001; Ottoy et al., 2016; Rosenbloom et al., 2001). The exponential decrease of SOC with depth in the near-surface develops primarily because of above-ground biomass and root litters, which are the main sources of carbon inputs to soil (Kögel-Knabner, 2002), mostly accumulating in the uppermost soil layer, namely 0-5 cm (Martinez et al., 2010). The decrease in SOC with soil depth does not hold, however, for depressions, where higher SOC concentration is found at 5-10 cm. This increase in SOC at depth probably results from the burial of soil by delivery and settling of incoming eroded material to the depressions, which physically protects the already residing SOC from decomposition (Berhe et al., 2012; Yan et al., 2019). Additionally, the Upper Sangamon fields generally exhibit more significant declines of

SOC concentrations between the 0-5 cm and 5-10 cm depths than those at the Clear Creek sites. The decreases of SOC concentration with soil depth become more prominent in "less-disturbed" sites (Billings et al., 2010; Don et al., 2007). This type of site is represented by those in the Upper Sangamon watershed, which is flatter and therefore experiences less runoff energy (i.e., stream power) to "disturb" it. Because surface erosion is limited, the biogeochemical processes, such as stabilization and decomposition, dominate the carbon dynamics in the Upper Sangamon Basin.

For the high-gradient Clear Creek sites, the mobilization of carbon-rich fine particles by runoff reduces the amount of SOC at the surface leading to less variability over depth in the top 10 cm of the soil (Harden et al., 2002; Papanicolaou et al., 2015). The possibility that runoff-driven erosion also contributes to a uniform SOC profile represents an alternative perspective to homogenization of SOC in the topsoil via mechanical mixing by tillage (Meersmans et al., 2009; Yan et al., 2019). Most likely, erosion (a by-product of the steep hillslope gradients) in combination with mechanical mixing homogenizes the vertical SOC profile.

The results herein do not reveal a direct correlation between SOC concentration and tillage intensity. A caveat of this study is that the soil samples analyzed in this study were collected as part of individual field campaigns. Therefore it is challenging to capture the effects of tillage on dynamic properties of soil such as SOC concentration, bulk density , or water content. Papanicolaou et al. (2015) reported that soil bulk density decreased directly following tillage events and then rebounded due to weight consolidation. Care, however, was given to limit the effects of seasonal dynamics, where samples in the two watersheds were collected between harvest and planting to allow sufficient time for consolidation. In addition to tillage and consolidation, particle size distribution and organic matter content also cause bulk density changes (Keller and Håkansson, 2010; Ruehlmann and Körschens, 2009). Nevertheless, the negative correlation between bulk density and SOC observed in the Upper Sangamon watershed can be attributed to the effect of SOC on bulk density given that increases in organic matter increase soil resilience to mechanical compressive stress (Soane, 1990).

Spatial Variability of SOC

The SOC concentrations in Clear Creek followed unimodal distributions with mean values of 2.11% at 0-5 cm and 1.99% at 5-10 cm and coefficients of variation from 9.55-10.90% showing low spatial variability. This result is similar to those reported by Guo et al. (2018) for the same area, where the SOC followed the normal distribution with a mean of 2.36% and a coefficient of variation of 14.41%. For the Upper Sangamon watershed, the SOC concentrations had multimodal distributions with mean values of 2.66% at 0-5 cm and 2.48% at 5-10 cm and coefficients of variation ranging from 27.07-32.66% revealing moderate spatial variability. These values fall in the reported SOC range of 2% to 6% for the Upper Sangamon region (Konen et al., 2002; Li et al., 2020). The higher-gradient

Clear Creek thus had roughly 25% less carbon and less than half a degree of variability of SOC than the lower-gradient Upper Sangamon watershed.

Topography, in terms of either surface gradient or topographic depressions, modulated by tillage induced oriented roughness (Hou et al., in press; Wacha et al., 2020), appears to be a primary control of the partitioning of rainfall into surface runoff and infiltration (Dunne et al., 1991; Thompson et al., 2010), which influences surface carbon dynamics through transport (i.e., erosion and deposition) and transformation (i.e., stabilization and decomposition). The surface gradient of Clear Creek is about eight times steeper on average than that of the Upper Sangamon watershed (Figure 2-2), providing higher potential energy for runoff-driven mobilization. The hillslope-scale plots illustrate the significant differences in hillslope gradients between the two watersheds. Differences in the spatial distribution and frequency of depressions (e.g., location, sizes, abundance), and possible effects of these differences on SOC distribution, is less obvious, given that only one of the hillslope plots for the Upper Sangamon River exhibits depressions. To characterize differences in depressions between the two watersheds, the location and sizes of the depressions were hence mapped for a 6 km × 6 km representative landscape from each watershed (Figure 2-13) using the topographic depression identification (TDI) model (Le and Kumar, 2014). The TDI model identifies depressions by searching local elevation minima and flow spillover thresholds (local elevation maxima). For each area, the total number of depressions, the density of depressions by surface area (m^2/m^2), and the density of depressions by storage volume (m^3/m^2) were computed. The Clear Creek watershed, an erosionally dissected landscape, only has depressions on valley floors and upland depressions are nearly non-existent (Figure 2-13a). Thus the steeper depression-free hillslopes in Clear Creek produce runoff with higher stream power and consequently enhance erosion-induced carbon mobilization (Fiener et al., 2015; Kirkels et al., 2014; Peñuela et al., 2015). The Upper Sangamon site is dominated by a large number of upland depressions (Figure 2-13b) that exceeds the number in Clear Creek by an order of magnitude. Moreover, the areal density of depressions in the Upper Sangamon watershed is 13 times greater than that in Clear Creek, and the volumetric density, or average depth of depression storage, in the Upper Sangamon watershed is about three times as large as it is in Clear Creek. The high density of upland depressions in the Upper Sangamon impedes the connectivity of surface runoff and, when filled with water under anoxic conditions, serve as biogeochemical reactors (Marton et al., 2015). These depressions substantially contributed to the spatial heterogeneity of SOC over the landscape (Cohen et al., 2016).

Conceptual models were created to illustrate the difference in governing processes of SOC dynamics between the two watersheds (Figure 2-14). In the higher-gradient Clear Creek, the steeper slopes produce higher runoff volumes with higher stream power (Papanicolaou et al., 2018), leading to three primary ways of SOC loss (Figure 2-14a): (1) preferential entrainment of carbon-rich particles by erosion usually in the upslope

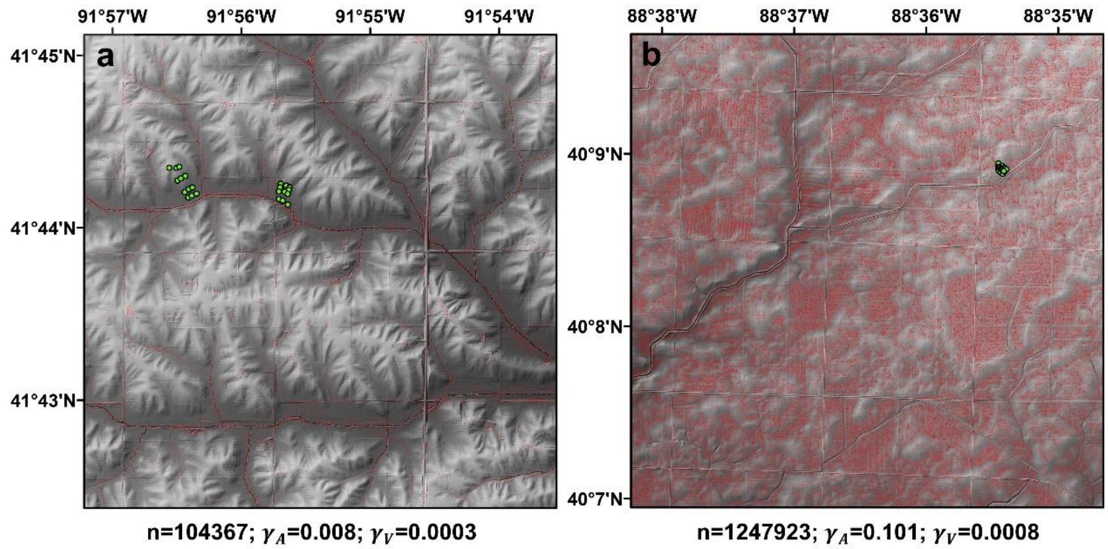

Figure 2-13. Shaded relief maps with identified topographic depressions (red polygons) in (a) South Amana-Clear Creek and (b) Goose Creek-Upper Sangamon. The depressions were identified by using the topographic depression identification (TDI) model of Le and Kumar (2014). Both example sites are 6 km × 6 km in area. The resolution of the LiDAR data used is 1 m. Green dots denote the soil sampling locations at CC#1, CC#2, and US#4, n represents the number of depressions on each site, γ_A represents the density of depressions by surface area on each site (m^2/m^2), γ_V represents the density of depressions by storage volume on each site (m^3/m^2).

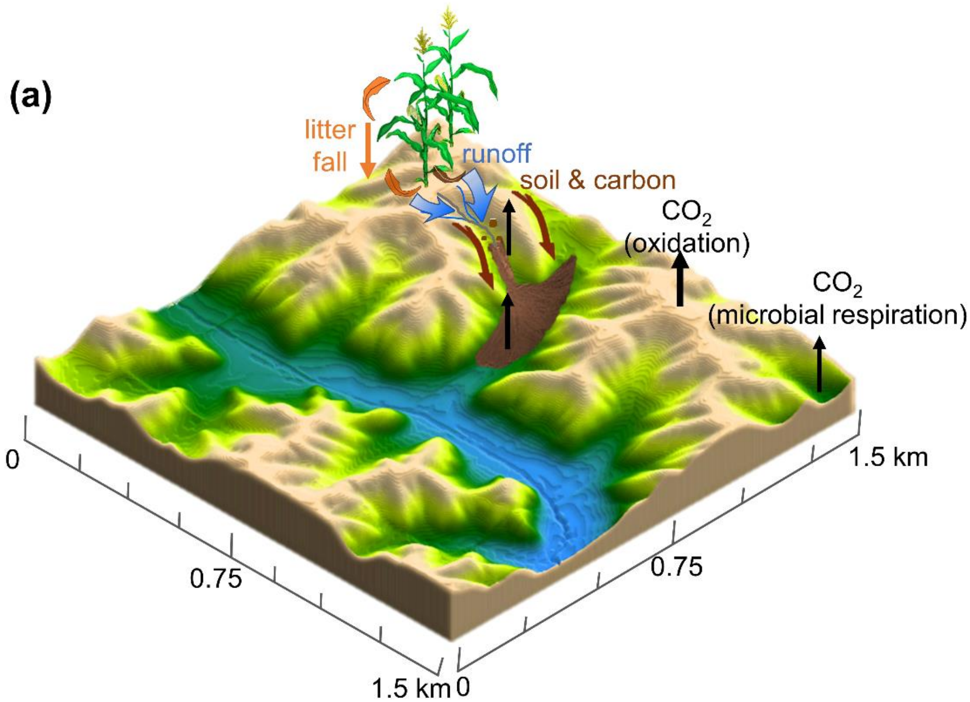

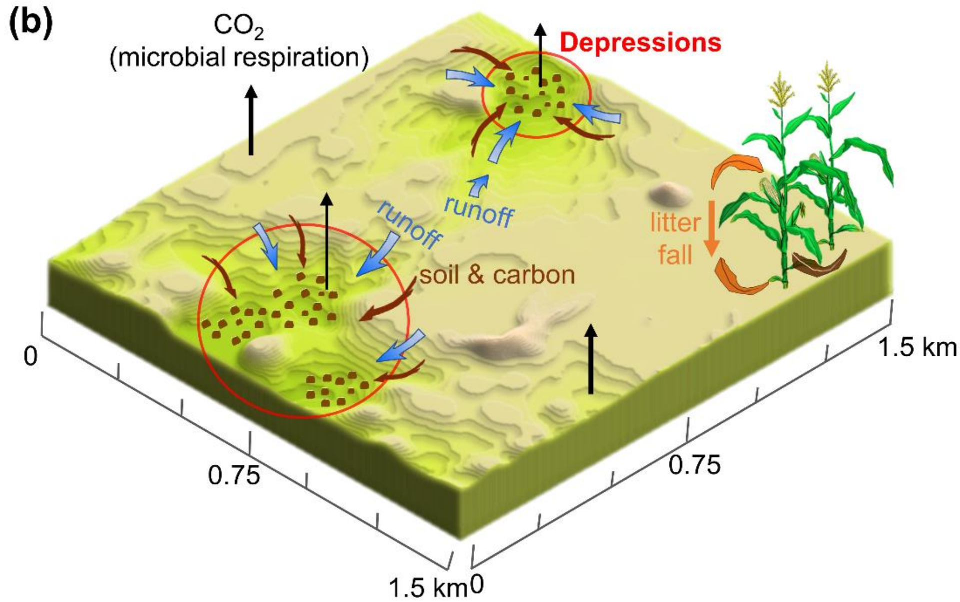

Figure 2-14. Conceptual relations governing surface carbon dynamics in (a) Clear Creek and (b) the Upper Sangamon watershed. Arrow size reflects the magnitude of respective variables.

(Papanicolaou et al., 2015); (2) enhanced turnover rate of buried carbon that has been uncovered by erosion and exposed to oxygen (Doetterl et al., 2016); and (3) erosion-induced mineralization of carbon during transport due to aggregates breakdown (Polyakov and Lal, 2008). The redistribution of soil over the landscape accelerates carbon depletion in the upslope eroding zone but slows carbon depletion in the downslope depositional zone as the mobilized SOC accumulates and is physically protected through burial (Berhe et al., 2012; Berhe et al., 2007; Doetterl et al., 2012; Ritchie et al., 2007).

The conceptual model shows the lateral geomorphological transport governing SOC storage and redistribution in the higher-gradient Clear Creek. Fields in Clear Creek have some of the highest erosion rates in Iowa with an average of 2 kg m^{-2} yr^{-1} (Abaci and Papanicolaou, 2009), due to the combination of steep slopes and intensive agriculture management (Cruse et al., 2006; Wilson et al., 2016). The average annual carbon loss due to soil erosion is 32 g m^{-2} yr^{-1} in CC#1 (Papanicolaou et al., 2015). In terms of the variability of SOC, the level of preferential mobilization of organic-rich particles decreases with higher runoff volumes due to the general movement of all particles regardless of size and density (Papanicolaou et al., 2015; Schiettecatte et al., 2008; Shi et al., 2012). In other words, the composition of the mobilized soil is more similar to the composition of the source soil under large runoff events, resulting in little to no SOC enrichment of the transported soil and lessening the degree of SOC heterogeneity across a field.

Though low slopes in the Upper Sangamon limit the lateral mobilization of surface material, the importance of depressions on SOC biogeochemistry becomes especially prominent (Figure 2-14b). The depressions not only collect significant amounts of water and organic-rich fine sediments from surrounding higher areas but also increase vertical mobilization of material through the soil column (Woo and Kumar, 2019; Zhao et al., 2018). Microbial decomposition of organic matter is likely suppressed under elevated soil moisture and associated anoxic conditions (Li et al., 2020; Skopp et al., 1990), leading to SOC accumulation in the depressions (Keiluweit et al., 2016). The higher carbon storage in the local depressions than in surrounding areas results in a high degree of SOC variability across this IML. Therefore, the SOC storage and distribution in the lower-gradient Upper Sangamon is controlled mostly by the biogeochemical cycles, which are limited by anoxic conditions in wet depressions. This inference is reflected by the PCA result, in which gravimetric water content is mostly related to the variation of SOC. A recent study conducted at the same sites by Li et al. (2020) also demonstrated that soil moisture correlates strongly with SOC as filling and vertical transport of water are more prominent in these depressions.

Conclusions

The present study has investigated the spatial variability of SOC concentrations for two intensively managed landscapes in the U.S. Midwest that differ substantially in topographic characteristics: a hilly erosional-depositional environment (e.g., Clear Creek) and a relatively flat, depression-dominated environment (e.g., Upper Sangamon).

Hillslope gradient and topographic depressions play central roles in the spatial heterogeneity of SOC at field and watershed scales by controlling the fate of water. On steep hillslopes, downslope mobilization of material under high runoff rates results in low SOC near hillslope summits or ridges and high SOC at toeslopes. On low-gradient hillslopes with depressions, mainly present in the Upper Sangamon, microbial decomposition of organic matter declines under elevated soil moisture and associated anoxic conditions, leading to higher SOC in the depressions than on surrounding rises. Additionally, the commonly observed exponential decay of SOC with depth does not hold for the depressions, in which SOC at 5-10 cm is physically protected from decomposition by the burial of surrounding rises eroded material. In the higher-gradient landscape, lower SOC variability occurs both vertically and laterally (unimodal, homogeneous) due to accelerated mass mobilization and mixing under high surface runoff. In contrast, SOC in the lower-gradient system owns 25% higher concentrations and two times higher spatial variability (multimodal, heterogeneous) as more carbon accumulates in the local depressions than surrounding areas, of which cascade effect increases the degree of SOC heterogeneity.

The preservation of soil quality is important in the U.S. Corn Belt, where local economies are driven by agricultural production. As one of the most important indicators of soil quality, SOC substantially affects soil health and crop productivity. The abundance and distribution of SOC are strongly influenced by applied management practices in the fields. Knowledge of the spatial variability of SOC concentration across the landscape is valuable for improving soil quality by altering management practices (e.g., tillage methods, fertilizer types) at steeper locations where low SOC concentrations are more likely to occur. The Vis-NIR technique can save considerable time and labor when analyzing large numbers of soil samples to support watershed-scale SOC modeling or developing high-resolution SOC maps for field-scale precision farming. Refinements of this method should focus on the variability in the shapes of Vis-NIR spectra to better define relationships between site characteristics and dominant spectra spikes.

Acknowledgements

This research was primarily supported by the National Science Foundation [grant number EAR1331906] for the IML-CZO program, a multi-institutional collaborative effort. This research was partially supported by USDA-NRCS [grant number 68748214530] for the RaCA program. Any opinions, findings, and conclusions or recommendations expressed in this material are those of the author(s) and do not necessarily reflect the views of the above agencies. The authors gratefully acknowledge Dr. David Hoover and Dr. Skye Wills from the National Soil Survey Center of USDA-NRCS for providing us with the Vis-NIR spectrometer. We would like to thank Dr. Praveen Kumar and Dr. Phong Le from the University of Illinois at Urbana-Champaign for their assistance in the TDI model. Special thanks are given to Dr. Andrew Stumpf from the Illinois State Geological Survey for reviewing and editing this manuscript. We also thank all members of IMLCZO who helped in the sampling campaigns of Clear Creek and Upper Sangamon. The first author was part of the China-UT EcoPartnership Scholars Program and is grateful for the support from the China Scholarship Council.

References

Abaci, O., Papanicolaou, A.N.T., 2009. Long-term effects of management practices on water-driven soil erosion in an intense agricultural sub-watershed: monitoring and modelling. Hydrological Processes 23(19), 2818-2837.

Abid, M., Lal, R., 2008. Tillage and drainage impact on soil quality: I. Aggregate stability, carbon and nitrogen pools. Soil and Tillage Research 100(1), 89-98.

Ali, M., Seeger, M., Sterk, G., Moore, D., 2013. A unit stream power based sediment transport function for overland flow. CATENA 101, 197-204.

Anders, A.M., Bettis III, E.A., Grimley, D.A., Stumpf, A.J., Kumar, P., 2018. Impacts of Quaternary History on Critical Zone Structure and Processes: Examples and a Conceptual Model From the Intensively Managed Landscapes Critical Zone Observatory. Frontiers in Earth Science 6, 24.

Ben-Dor, E., Banin, A., 1995. Near-Infrared Analysis as a Rapid Method to Simultaneously Evaluate Several Soil Properties. Soil Science Society of America Journal 59(2), 364-372.

Berhe, A.A., Barnes, R.T., Six, J., Marín-Spiotta, E., 2018. Role of soil erosion in biogeochemical cycling of essential elements: Carbon, nitrogen, and phosphorus. Annual Review of Earth and Planetary Sciences 46, 521-548.

Berhe, A.A., Harden, J.W., Torn, M.S., Kleber, M., Burton, S.D., Harte, J., 2012. Persistence of soil organic matter in eroding versus depositional landform positions. Journal of Geophysical Research: Biogeosciences 117(G2).

Berhe, A.A., Harte, J., Harden, J.W., Torn, M.S., 2007. The significance of the erosion-induced terrestrial carbon sink. BioScience 57(4), 337-346.

Bertassello, L.E., Rao, P.S.C., Jawitz, J.W., Botter, G., Le, P.V.V., Kumar, P., Aubeneau, A.F., 2018. Wetlandscape Fractal Topography. 45(14), 6983-6991.

Bettis, E.A., Muhs, D.R., Roberts, H.M., Wintle, A.G., 2003. Last glacial loess in the conterminous USA. Quaternary Science Reviews 22(18-19), 1907-1946.

Billings, S.A., Buddemeier, R.W., deB. Richter, D., Van Oost, K., Bohling, G., 2010. A simple method for estimating the influence of eroding soil profiles on atmospheric CO_2. Global Biogeochemical Cycles 24(2).

Chang, C.-W., Laird, D.A., 2002. Near-infrared reflectance spectroscopic analysis of soil C and N. Soil Science 167(2), 110-116.

Chang, C.-W., Laird, D.A., Hurburgh, C.R.J., 2005. Influence of soil moisture on near-infrared reflectance spectroscopic measurement of soil properties. Soil Science 170(4), 244-255.

Chang, C.-W., Laird, D.A., Mausbach, M.J., Hurburgh, C.R., 2001. Near-Infrared Reflectance Spectroscopy–Principal Components Regression Analyses of Soil Properties. Soil Science Society of America Journal 65(2), 480-490.

Cohen, M.J., Creed, I.F., Alexander, L., Basu, N.B., Calhoun, A.J.K., Craft, C., D'Amico, E., DeKeyser, E., Fowler, L., Golden, H.E., 2016. Do geographically isolated wetlands influence landscape functions? PNAS 113(8), 1978-1986.

Conforti, M., Buttafuoco, G., Leone, A.P., Aucelli, P.P.C., Robustelli, G., Scarciglia, F., 2013. Studying the relationship between water-induced soil erosion and soil organic matter using Vis–NIR spectroscopy and geomorphological analysis: A case study in southern Italy. Catena 110, 44-58.

Cox, I., Gaudard, M., 2013. Discovering partial least squares with JMP. SAS Institute.

Cruse, R., Flanagan, D., Frankenberger, J., Gelder, B., Herzmann, D., James, D., Krajewski, W., Kraszewski, M., Laflen, J., Opsomer, J., Todey, D., 2006. Daily estimates of rainfall, water runoff, and soil erosion in Iowa. Journal of Soil and Water Conservation 61(4), 191-199.

Doetterl, S., Berhe, A.A., Nadeu, E., Wang, Z., Sommer, M., Fiener, P., 2016. Erosion, deposition and soil carbon: A review of process-level controls, experimental tools and models to address C cycling in dynamic landscapes. Earth-Science Reviews 154, 102-122.

Doetterl, S., Six, J., Van Wesemael, B., Van Oost, K., 2012. Carbon cycling in eroding landscapes: geomorphic controls on soil organic C pool composition and C stabilization. Global Change Biology 18(7), 2218-2232.

Don, A., Schumacher, J., Scherer-Lorenzen, M., Scholten, T., Schulze, E.-D., 2007. Spatial and vertical variation of soil carbon at two grassland sites — Implications for measuring soil carbon stocks. Geoderma 141(3), 272-282.

Dunne, T., Zhang, W., Aubry, B.F., 1991. Effects of rainfall, vegetation, and microtopography on infiltration and runoff. Water Resources Research 27(9), 2271-2285.

Elliott, J., Efetha, A., 1999. Influence of tillage and cropping system on soil organic matter, structure and infiltration in a rolling landscape. Canadian Journal of Soil Science 79(3), 457-463.

Escandar, G.M., Damiani, P.C., Goicoechea, H.C., Olivieri, A.C., 2006. A review of multivariate calibration methods applied to biomedical analysis. Microchemical Journal 82(1), 29-42.

Fiener, P., Dlugoß, V., Van Oost, K., 2015. Erosion-induced carbon redistribution, burial and mineralisation—Is the episodic nature of erosion processes important? Catena 133, 282-292.

Fissore, C., Dalzell, B.J., Berhe, A.A., Voegtle, M.A., Evans, M.A., Wu, A., 2017. Influence of topography on soil organic carbon dynamics in a Southern California grassland. Catena 149, 140-149.

Flanagan, D.C., Nearing, M.A., 1995. USDA-Water Erosion Prediction Project: Hillslope profile and watershed model documentation. Nserl Rep 10, 1-123.

Fox, J.F., Papanicolaou, A.N., 2007. The use of carbon and nitrogen isotopes to study watershed erosion processes. JAWRA Journal of the American Water Resources Association 43(4), 1047-1064.

Galvao, R.K., Araujo, M.C., Jose, G.E., Pontes, M.J., Silva, E.C., Saldanha, T.C., 2005. A method for calibration and validation subset partitioning. Talanta 67(4), 736-740.

Ge, Y., Morgan, C.L.S., Grunwald, S., Brown, D.J., Sarkhot, D.V., 2011. Comparison of soil reflectance spectra and calibration models obtained using multiple spectrometers. Geoderma 161(3-4), 202-211.

Ge, Y., Thomasson, J.A., Morgan, C.L.S., 2014. Mid-infrared attenuated total reflectance spectroscopy for soil carbon and particle size determination. Geoderma 213, 57-63.

Guo, L., Linderman, M., Shi, T., Chen, Y., Duan, L., Zhang, H., 2018. Exploring the sensitivity of sampling density in digital mapping of soil organic carbon and its application in soil sampling. Remote Sensing 10(6), 888.

Hao, Y., Lal, R., Owens, L.B., Izaurralde, R.C., Post, W.M., Hothem, D.L., 2002. Effect of cropland management and slope position on soil organic carbon pool at the North Appalachian Experimental Watersheds. Soil and Tillage Research 68(2), 133-142.

Harden, J.W., Fries, T.L., Pavich, M.J., 2002. Cycling of Beryllium and Carbon through hillslope soils in Iowa. Biogeochemistry 60(3), 317-336.

Henderson, T.L., Baumgardner, M.F., Franzmeier, D.P., Stott, D.E., Coster, D.C., 1992. High dimensional reflectance analysis of soil organic matter. Soil Science Society of America Journal 56(3), 865-872.

Hilinski, T.E., 2001. Implementation of exponential depth distribution of organic carbon in the CENTURY model. Dep. of Soil and Crop Sci., Colorado State Univ., Fort Collins.

Hou, T., Berry, T.D., Singh, S., Hughes, M.N., Tong, Y., Thanos Papanicolaou, A.N., Wacha, K.M., Wilson, C.G., Chaubey, I., Filley, T.R., 2018. Control of tillage disturbance on the chemistry and proportion of raindrop-liberated particles from soil aggregates. Geoderma 330, 19-29.

Hou, T., Filley, T.R., Tong, Y., Abban, B.K., Singh, S., Papanicolaou, A.T., Wacha, K.M., Wilson, C.G., Chaubey, I., in press. Tillage-induced surface soil roughness controls the chemistry and physics of eroded particles at early erosion stage. Soil and Tillage Research.

Ingleby, H.R., Crowe, T.G., 1999. Spectral reflectance measurements for organic matter sensing in Saskatchewan soils. Canadian Agricultural Engineering 41(2), 73-80.

Jenson, S.K., Domingue, J.O., 1988. Extracting topographic structure from digital elevation data for geographic information system analysis. Photogrammetric engineering remote sensing 54(11), 1593-1600.

John, B., Yamashita, T., Ludwig, B., Flessa, H., 2005. Storage of organic carbon in aggregate and density fractions of silty soils under different types of land use. Geoderma 128(1), 63-79.

Katuwal, S., Knadel, M., Moldrup, P., Norgaard, T., Greve, M.H., de Jonge, L.W., 2018. Visible–Near-Infrared Spectroscopy can predict Mass Transport of Dissolved Chemicals through Intact Soil. Scientific Reports 8(1), 11188.

Keiluweit, M., Nico, P.S., Kleber, M., Fendorf, S., 2016. Are oxygen limitations under recognized regulators of organic carbon turnover in upland soils? Biogeochemistry 127(2), 157-171.

Keller, T., Håkansson, I., 2010. Estimation of reference bulk density from soil particle size distribution and soil organic matter content. Geoderma 154(3), 398-406.

Keselman, H.J., Rogan, J.C., 1977. The Tukey multiple comparison test: 1953–1976. Psychological Bulletin 84(5), 1050-1056.

Kirkels, F.M.S.A., Cammeraat, L.H., Kuhn, N.J., 2014. The fate of soil organic carbon upon erosion, transport and deposition in agricultural landscapes — A review of different concepts. Geomorphology 226, 94-105.

Kirschbaum, M.U.F., 1995. The temperature dependence of soil organic matter decomposition, and the effect of global warming on soil organic C storage. Soil Biology and Biochemistry 27(6), 753-760.

Kögel-Knabner, I., 2002. The macromolecular organic composition of plant and microbial residues as inputs to soil organic matter. Soil Biology and Biochemistry 34(2), 139-162.

Konen, M.E., Jacobs, P.M., Burras, C.L., Talaga, B.J., Mason, J.A., 2002. Equations for Predicting Soil Organic Carbon Using Loss-on-Ignition for North Central U.S. Soils. Soil Science Society of America Journal 66(6), 1878-1881.

Kumar, P., Le, P.V.V., Papanicolaou, A.N.T., Rhoads, B.L., Anders, A.M., Stumpf, A., Wilson, C.G., Bettis, E.A., Blair, N., Ward, A.S., Filley, T., Lin, H., Keefer, L., Keefer, D.A., Lin, Y.-F., Muste, M., Royer, T.V., Foufoula-Georgiou, E., Belmont, P., 2018. Critical transition in critical zone of intensively managed landscapes. Anthropocene 22, 10-19.

Le, P.V.V., Kumar, P., 2014. Power law scaling of topographic depressions and their hydrologic connectivity. Geophysical Research Letters 41(5), 1553-1559.

Le, P.V.V., Kumar, P., 2017. Interaction Between Ecohydrologic Dynamics and Microtopographic Variability Under Climate Change. Water Resources Research 53(10), 8383-8403.

Levene, H., 1961. Robust tests for equality of variances. Contributions to probability and statistics. Essays in honor of Harold Hotelling, 279-292.

Li, M., Foster, E.J., Le, P.V.V., Yan, Q., Stumpf, A., Hou, T., Papanicolaou, A.N., Wacha, K.M., Wilson, C.G., Wang, J., Kumar, P., Filley, T., 2020. A new dynamic wetness index (DWI) predicts soil moisture persistence and correlates with key indicators of surface soil geochemistry. Geoderma 368, 114239.

Li, X., McCarty, G.W., Karlen, D.L., Cambardella, C.A., 2018. Topographic metric predictions of soil redistribution and organic carbon in Iowa cropland fields. CATENA 160, 222-232.

Lopez-Bellido, R.J., Muñoz-Romero, V., Fuentes-Guerra, R., Fernandez-Garcia, P., Lopez-Bellido, L., 2017. No-till: A key tool for sequestering C and N in microaggregates on a Mediterranean Vertisol. Soil and Tillage Research 166, 131-137.

Margenot, A.J., Calderón, F.J., Bowles, T.M., Parikh, S.J., Jackson, L.E., 2015. Soil Organic Matter Functional Group Composition in Relation to Organic Carbon, Nitrogen, and Phosphorus Fractions in Organically Managed Tomato Fields. Soil Science Society of America Journal 79(3), 772-782.

Martens, H., Nï, T., 1992. Multivariate calibration. John Wiley & Sons.

Martinez, C., Hancock, G.R., Kalma, J.D., 2010. Relationships between 137Cs and soil organic carbon (SOC) in cultivated and never-cultivated soils: An Australian example. Geoderma 158(3), 137-147.

Marton, J.M., Creed, I.F., Lewis, D.B., Lane, C.R., Basu, N.B., Cohen, M.J., Craft, C.B., 2015. Geographically isolated wetlands are important biogeochemical reactors on the landscape. Bioscience 65(4), 408-418.

Meersmans, J., van Wesemael, B., De Ridder, F., Van Molle, M., 2009. Modelling the three-dimensional spatial distribution of soil organic carbon (SOC) at the regional scale (Flanders, Belgium). Geoderma 152(1), 43-52.

Moorman, T.B., Cambardella, C.A., James, D.E., Karlen, D.L., Kramer, L.A., 2004. Quantification of tillage and landscape effects on soil carbon in small Iowa watersheds. Soil and Tillage Research 78(2), 225-236.

Morgan, C.L.S., Waiser, T.H., Brown, D.J., Hallmark, C.T., 2009. Simulated in situ characterization of soil organic and inorganic carbon with visible near-infrared diffuse reflectance spectroscopy. Geoderma 151(3), 249-256.

Ottoy, S., Elsen, A., Van De Vreken, P., Gobin, A., Merckx, R., Hermy, M., Van Orshoven, J., 2016. An exponential change decline function to estimate soil organic carbon stocks and their changes from topsoil measurements. European Journal of Soil Science 67(6), 816-826.

Papanicolaou, A.N., Abban, B.K.B., Dermisis, D.C., Giannopoulos, C.P., Flanagan, D.C., Frankenberger, J.R., Wacha, K.M., 2018. Flow Resistance Interactions on Hillslopes With Heterogeneous Attributes: Effects on Runoff Hydrograph Characteristics. Water Resources Research 54(1), 359-380.

Papanicolaou, A.N.T., Wacha, K.M., Abban, B.K., Wilson, C.G., Hatfield, J.L., Stanier, C.O., Filley, T.R., 2015. From soilscapes to landscapes: A landscape-oriented approach to simulate soil organic carbon dynamics in intensively managed landscapes. Journal of Geophysical Research: Biogeosciences 120(11), 2375-2401.

Patton, N.R., Lohse, K.A., Seyfried, M.S., Godsey, S.E., Parsons, S.B., 2019. Topographic controls of soil organic carbon on soil-mantled landscapes. Scientific Reports 9(1), 6390.

Peñuela, A., Javaux, M., Bielders, C.L., 2015. How do slope and surface roughness affect plot-scale overland flow connectivity? Journal of Hydrology 528, 192-205.

Polyakov, V.O., Lal, R., 2008. Soil organic matter and CO_2 emission as affected by water erosion on field runoff plots. Geoderma 143(1), 216-222.

Razali, N.M., Wah, Y.B., 2011. Power comparisons of shapiro-wilk, kolmogorov-smirnov, lilliefors and anderson-darling tests. Journal of statistical modeling and analytics 2(1), 21-33.

Reeves, D.W., 1997. The role of soil organic matter in maintaining soil quality in continuous cropping systems. Soil and Tillage Research 43(1-2), 131-167.

Rhoads, B.L., Lewis, Q.W., Andresen, W., 2016. Historical changes in channel network extent and channel planform in an intensively managed landscape: Natural versus human-induced effects. Geomorphology 252, 17-31.

Ritchie, J.C., McCarty, G.W., Venteris, E.R., Kaspar, T.C., 2007. Soil and soil organic carbon redistribution on the landscape. Geomorphology 89(1-2), 163-171.

Rosenbloom, N.A., Doney, S.C., Schimel, D.S., 2001. Geomorphic evolution of soil texture and organic matter in eroding landscapes. Global Biogeochemical Cycles 15(2), 365-381.

Rosenbloom, N.A., Harden, J.W., Neff, J.C., Schimel, D.S., 2006. Geomorphic control of landscape carbon accumulation. Journal of Geophysical Research: Biogeosciences 111(G1).

Ruehlmann, J., Körschens, M., 2009. Calculating the effect of soil organic matter concentration on soil bulk density. Soil Science Society of America Journal 73(3), 876-885.

Scharlemann, J.P.W., Tanner, E.V.J., Hiederer, R., Kapos, V., 2014. Global soil carbon: understanding and managing the largest terrestrial carbon pool. Carbon Management 5(1), 81-91.

Schiettecatte, W., Gabriels, D., Cornelis, W.M., Hofman, G., 2008. Enrichment of organic carbon in sediment transport by interrill and rill erosion processes. Soil Science Society of America Journal 72(1), 50-55.

Schloeder, C.A., Zimmerman, N.E., Jacobs, M.J., 2001. Comparison of methods for interpolating soil properties using limited data. Soil science society of America journal 65(2), 470-479.

Schwanghart, W., Jarmer, T., 2011. Linking spatial patterns of soil organic carbon to topography—a case study from south-eastern Spain. Geomorphology 126(1-2), 252-263.

Shi, Z., Fang, N., Wu, F., Wang, L., Yue, B., Wu, G., 2012. Soil erosion processes and sediment sorting associated with transport mechanisms on steep slopes. Journal of Hydrology 454, 123-130.

Shih, H.-M., Yang, C.T., 2009. Estimating overland flow erosion capacity using unit stream power. International Journal of Sediment Research 24(1), 46-62.

Six, J., Paustian, K., Elliott, E.T., Combrink, C., 2000. Soil Structure and Organic Matter I. Distribution of Aggregate-Size Classes and Aggregate-Associated Carbon. Soil Science Society of America Journal 64(2), 681-689.

Skopp, J., Jawson, M.D., Doran, J.W., 1990. Steady-state aerobic microbial activity as a function of soil water content. Soil Science Society of America Journal 54(6), 1619-1625.

Soane, B.D., 1990. The role of organic matter in soil compactibility: A review of some practical aspects. Soil and Tillage Research 16(1), 179-201.

Sollins, P., Homann, P., Caldwell, B.A., 1996. Stabilization and destabilization of soil organic matter: mechanisms and controls. Geoderma 74(1), 65-105.

Stenberg, B., Viscarra Rossel, R.A., Mouazen, A.M., Wetterlind, J., 2010. Chapter Five - Visible and Near Infrared Spectroscopy in Soil Science. In: D.L. Sparks (Ed.), Advances in Agronomy. Academic Press, pp. 163-215.

Stevens, A., Nocita, M., Tóth, G., Montanarella, L., van Wesemael, B., 2013. Prediction of soil organic carbon at the European scale by visible and near infrared reflectance spectroscopy. PloS one 8(6), e66409.

Thompson, S.E., Katul, G.G., Porporato, A., 2010. Role of microtopography in rainfall-runoff partitioning: An analysis using idealized geometry. Water Resources Research 46(7).

USDA, 1982. Soil Survey of Champaign County, Illinois.

USDA, 1996. Survey Laboratory Methods Manual, Soil Survey Investigations Report.

USDA, 2004. Soil Survey of Sangamon County, Illinois. Natural Resources Conservation Service.

Van Veen, J.A., Kuikman, P.J., 1990. Soil structural aspects of decomposition of organic matter by micro-organisms. Biogeochemistry 11(3), 213-233.

VandenBygaart, A.J., Gregorich, E.G., Angers, D.A., McConkey, B.G., 2007. Assessment of the lateral and vertical variability of soil organic carbon. Canadian Journal of Soil Science 87(4), 433-444.

Viscarra Rossel, R.A., 2008. ParLeS: Software for chemometric analysis of spectroscopic data. Chemometrics and Intelligent Laboratory Systems 90(1), 72-83.

Viscarra Rossel, R.A., Behrens, T., Ben-Dor, E., Brown, D.J., Demattê, J.A.M., Shepherd, K.D., Shi, Z., Stenberg, B., Stevens, A., Adamchuk, V., Aïchi, H., Barthès, B.G., Bartholomeus, H.M., Bayer, A.D., Bernoux, M., Böttcher, K., Brodský, L., Du, C.W., Chappell, A., Fouad, Y., Genot, V., Gomez, C., Grunwald, S., Gubler, A., Guerrero, C., Hedley, C.B., Knadel, M., Morrás, H.J.M., Nocita, M., Ramirez-Lopez, L., Roudier, P., Campos, E.M.R., Sanborn, P., Sellitto, V.M., Sudduth, K.A., Rawlins, B.G., Walter, C., Winowiecki, L.A., Hong, S.Y., Ji, W., 2016. A global spectral library to characterize the world's soil. Earth-Science Reviews 155, 198-230.

Viscarra Rossel, R.A., Walvoort, D.J.J., McBratney, A.B., Janik, L.J., Skjemstad, J.O., 2006. Visible, near infrared, mid infrared or combined diffuse reflectance spectroscopy for simultaneous assessment of various soil properties. Geoderma 131(1), 59-75.

Wacha, K., Papanicolaou, A., Giannopoulos, C., Abban, B., Wilson, C., Zhou, S., Hatfield, J., Filley, T., Hou, T., 2018. The Role of Hydraulic Connectivity and Management on Soil Aggregate Size and Stability in the Clear Creek Watershed, Iowa. Geosciences 8(12), 470.

Wacha, K.M., Papanicolaou, A.T., Abban, B.K., Wilson, C.G., Giannopoulos, C.P., Hou, T., Filley, T.R., Hatfield, J.L., 2020. The impact of tillage row orientation on physical and chemical sediment enrichment. Agrosystems, Geosciences Environment international.

Wang, X., Chen, Y., Guo, L., Liu, L., 2017. Construction of the Calibration Set through Multivariate Analysis in Visible and Near-Infrared Prediction Model for Estimating Soil Organic Matter. Remote Sensing 9(3).

West, T.O., Post, W.M., 2002. Soil organic carbon sequestration rates by tillage and crop rotation. Soil Science Society of America Journal 66(6), 1930-1946.

Wiesmeier, M., Urbanski, L., Hobley, E., Lang, B., von Lützow, M., Marin-Spiotta, E., van Wesemael, B., Rabot, E., Ließ, M., Garcia-Franco, N., Wollschläger, U., Vogel, H.-J., Kögel-Knabner, I., 2019. Soil organic carbon storage as a key function of soils - A review of drivers and indicators at various scales. Geoderma 333, 149-162.

Wijewardane, N.K., Ge, Y., Wills, S., Loecke, T., 2016. Prediction of Soil Carbon in the Conterminous United States: Visible and Near Infrared Reflectance Spectroscopy Analysis of the Rapid Carbon Assessment Project. Soil Science Society of America Journal 80(4), 973-982.

Wills, S., Loecke, T., Sequeira, C., Teachman, G., Grunwald, S., West, L.T., 2014. Overview of the US rapid carbon assessment project: sampling design, initial summary and uncertainty estimates, Soil carbon. Springer, pp. 95-104.

Wilson, C.G., Abban, B., Keefer, L.L., Wacha, K., Dermisis, D., Giannopoulos, C., Zhou, S., Goodwell, A.E., Woo, D.K., Yan, Q., Ghadiri, M., Stumpf, A., Pitcel, M., Lin, Y.-F., Marini, L., Storsved, B., Goff, K., Vogelgsang, J., Dere, A., Schilling, K.E., Muste, M., Blair, N.E., Rhoads, B., Bettis, A., Pai, H., Kratt, C., Sladek, C., Wing, M., Selker, J., Tyler, S., Lin, H., Kumar, P., Papanicolaou, A.N., 2018. The Intensively Managed Landscape Critical Zone Observatory: A Scientific Testbed for Understanding Critical Zone Processes in Agroecosystems. Vadose Zone Journal 17(1).

Wilson, C.G., Wacha, K.M., Papanicolaou, A.N., Sander, H.A., Freudenberg, V.B., Abban, B.K.B., Zhao, C., 2016. Dynamic Assessment of Current Management in an Intensively Managed Agroecosystem. Journal of Contemporary Water Research & Education 158(1), 148-171.

Woo, D.K., Kumar, P., 2017. Role of micro-topographic variability on the distribution of inorganic soil-nitrogen age in intensively managed landscape. Water Resources Research 53(10), 8404-8422.

Woo, D.K., Kumar, P., 2019. Impacts of Subsurface Tile Drainage on Age—Concentration Dynamics of Inorganic Nitrogen in Soil. Water Resources Research 55(2), 1470-1489.

Yan, Q., Le, P.V.V., Woo, D.K., Hou, T., Filley, T., Kumar, P., 2019. Three-Dimensional Modeling of the Coevolution of Landscape and Soil Organic Carbon. Water Resources Research 55(2), 1218-1241.

Yoo, K., Amundson, R., Heimsath, A.M., Dietrich, W.E., 2005. Erosion of upland hillslope soil organic carbon: Coupling field measurements with a sediment transport model. Global Biogeochemical Cycles 19(3).

Yu, Z., Lu, C., Cao, P., Tian, H., 2018. Long-term terrestrial carbon dynamics in the Midwestern United States during 1850–2015: Roles of land use and cover change and agricultural management. Global change biology 24(6), 2673-2690.

Zhao, L., Hou, R., Wu, F., Keesstra, S., 2018. Effect of soil surface roughness on infiltration water, ponding and runoff on tilled soils under rainfall simulation experiments. Soil and Tillage Research 179, 47-53.

Zou, Z., Zhao, J., Povey, M.J., Holmes, M., Mao, H., 2010. Variables selection methods in near-infrared spectroscopy. Anal Chim Acta 667(1-2), 14-32.

CHAPTER THREE

TRACKING AGGREGATE TURNOVER IN SITU UNDER RAINDROP IMPACT AND WETTING-DRYING CYCLES USING RARE EARTH ELEMENTS

Abstract: Soil aggregate formation and breakdown directly control SOC stabilization through the physical protection and/or exposure of organic matter. A rare earth element (REE) tracing approach was used to investigate the breakdown and formation processes of soil aggregates under natural conditions under raindrop impact and wetting-drying cycles. Four aggregate size classes (8-19 mm, extra-large macroaggregates; 2-8 mm, large macroaggregates; 0.075-2 mm, small macroaggregates; <0.075 mm, fines, namely silt + clay-sized fraction) from soil collected in the Goose Creek (IL) watershed were labeled with different REE tracers and broadcast over a 7.3 m × 5 m plot located in the same field where the soil was collected. Daily rainfall amount, soil water content, and CO_2 flux were measured by an eddy covariance flux tower near the field and were used to assess the responses of soil moisture and microbial activity to rain events. Additionally, the aggregate stability index (ASI) of the extra-large, large, and small macroaggregates were tested in the laboratory under 5 min of simulated rainfall with a 60-mm h^{-1} intensity. Small macroaggregates were found to have the highest ASI value (0.98 ± 0.01) and SOC concentration (3.01% ± 0.03%) compared to the other three fractions. Samples from the plots were collected on Day 3 and Day 26 after two series of rainfall events. Soil mass transfers between aggregate size fractions through breakdown and formation were quantified by following the REE redistribution into the other size fractions. The samples collected on Day 3 showed a greater proportion of aggregate breakdown occurred than aggregate formation across the four size fractions showing the prominent breakdown by raindrop impact. The samples collected on Day 26, following a drying-wetting cycle, showed there was a greater proportion of aggregate formation than breakdown between the four size fractions manifesting a dominated aggregate stabilization. The aggregate turnover times, reciprocal of aggregate turnover rate, increased as the time frame increased from 3 days to 26 days (3-8 vs. 53-110 days). Over the entire experiment, small macroaggregates turned over most rapidly (0.019 day^{-1}), and extra-large macroaggregates and fines turned over most slowly (0.009 day^{-1}). Our results expand the understanding and modeling of aggregate dynamics and SOC cycling under raindrop impact and climate change triggered wetting-drying cycles.
Keywords: Aggregate turnover, Rare earth elements, Raindrop impact, Wetting-drying, SOC

Introduction

Aggregates are fundamental units of soil architecture (Lin, 2012) that control carbon storage (Six et al., 2001b), water transport (Le Bissonnais, 1996), and gas exchange (Sexstone et al., 1985). Soil aggregates dynamically change in terms of size and structural arrangement through breaking or bonding under physical and biological processes (Oades, 1993; Six et al., 2004). Aggregate breakdown releases smaller soil particles that increase the accessibility of previously occluded and protected SOC to microbial attack (Gregorich et al., 1989; Hou et al., 2018; Rovira and Greacen, 1957). Conversely, aggregate formation brings together smaller particles and physically stabilizes and protects SOC within aggregates resulting in promising improvement of soil structure in agricultural soils (Kibblewhite et al., 2008; Six et al., 2000a).

Aggregates at the soil surface are frequently impacted by raindrops. Raindrop-induced forces overcome the bonds that hold together individual particles in aggregates (Le Bissonnais, 1996). Rainfall breaks the soil aggregates through the mechanisms of slaking and raindrop impact. Rainfall intensity, aggregate porosity, and antecedent soil moisture are major factors regulating these mechanisms (Le Bissonnais, 1996; Truman et al., 1990). Slaking is the miniature "explosion" of soil aggregates into smaller-sized microaggregates with the compression of entrapped air when rapidly wetted (Sutherland et al., 1996; Zaher et al., 2005). Meanwhile, raindrop impact causes the mechanical breakdown of soil aggregates by the kinetic energy of falling raindrops (the "hammering" effect), which leads to the peeling process producing smaller aggregates, as well as clay- and silt-sized particles (Ma et al., 2014; Vaezi et al., 2017). During a rain event, slaking predominates during the first millimeters of rain when the soil is relatively dry (until field capacity is reached), and afterward raindrop impact becomes more prevalent to fragment the prewetted aggregates (Legout et al., 2005; Shi et al., 2017).

Soil aggregates in the field are subject to alternating wetting and drying cycles as soil water content can vary greatly (20-40%) both during storm events (Cao et al., 2020; Peng et al., 2019) and between events (e.g., days). Short wetting-drying cycles (e.g., a few days' duration) may cause cracks in the soil due to clay swelling and shrinkage (Tang et al., 2011). In the longer term (e.g., months), the wetting-drying cycles are directly involved in the formation and stabilization of soil aggregates through physical processes or indirectly through their interaction with the accumulation of microbes and crop residues during growing seasons (Cosentino et al., 2006; Denef et al., 2001a; Utomo and Dexter, 1982). Cohesion increases in wetted soil, promoting the bonding together of soil particles through migration and cementing processes of soluble components (Kemper and Rosenau, 1984); when the wetted soil is dried, the particle orientation and location in aggregates may remain unaltered, leading to increased aggregate size and stability (Hadas, 1990; Rajaram and Erbach, 1999). Furthermore, microbes (e.g., bacterial, fungal) proliferate rapidly upon rewetting dry soil (Meisner et al., 2013; Navarro-García et al., 2012). These microbes serve as aggregating agents by producing extracellular polysaccharides and fungal hyphae that can bind together soil particles into aggregates (Chaney and Swift, 1986; Griffiths and Jones, 1965).

The breakdown and formation are part of the life cycle of aggregates (i.e., aggregate turnover), of which two processes are interdependent. However, the literature reviewed above focused separately on either the breakdown or the formation thus failing to disentangle the iterative process between aggregate breakdown and formation. In recent years, a small group of researchers has studied the aggregate turnover process using the rare earth elements (REE) as tracers (De Gryze et al., 2006; Peng et al., 2017; Plante et al., 1999; Wang et al., 2020), on account of their strong bonding capacity, low background concentration, and high detectability (Kimoto et al., 2006; Zhang et al., 2001). REE oxides can uniformly attach to soil aggregates regardless of size and do not affect microbial activity or the aggregate turnover process itself, which allows tracking of mass flow between aggregates by following the release/incorporation of REE from/into different size fractions (De Gryze et al., 2006; Peng et al., 2017).

Using the REE tracing, Peng et al. (2017) found that a greater amount of aggregates exchanged between neighboring size fractions and the addition of glucose increased aggregate turnover rates and soil respiration. Morris et al. (2019) reported that arbuscular mycorrhizal fungi increased large macroaggregate formation and slowed down large and small macroaggregate breakdown. Rahman et al. (2019) showed that corn residue incorporation led to a faster turnover of aggregates due to the decomposition of new organic matter. However, all these studies were conducted in the laboratory under controlled conditions and focused on the effects of biological processes on aggregate breakdown and formation. To date, the aggregate dynamics in the field where there is more involvement of physical processes (i.e., raindrop impact and wetting-drying cycles) remain unknown.

The purpose of the present study is to decipher soil aggregate dynamics in the field under the influence of raindrop impact and drying-wetting cycles using REE as tracers. Specific objectives are to (1) test the aggregate stability for various size fractions with simulated rainfall; (2) quantify the aggregate transfer paths and turnover rates by coupling the REE measurements and a mathematical model framework; (3) investigate the effects of raindrop impact and wetting-drying cycles on the observed breakdown and formation of soil aggregates. By addressing these objectives, this study expands the knowledge of aggregate turnover in field conditions and provides new insights into modeling aggregate dynamics and carbon cycling.

Materials and Methods

Site Description and Aggregate Preparation

This study was conducted in a field planted with corn in the Goose Creek watershed near De Land, IL (40°08'39.4"N, 88°36'37.0"W). The soil is a Sable silty clay loam (66% silt, 32% clay, and 2% sand) derived from Quaternary loess with a field capacity of 31% and permanent wilting point around 15% (Salter and Williams, 1965). The majority of rain falls in May and June, where heavy convectional storms coincide with the early growth of crop plants (Wilson et al., 2018).

In late April 2019, before planting, 32 kg of surface soil (within the top 5 cm) were collected carefully from the field using a hand shovel. The soil was immediately sealed in a plastic bag, placed in a 20-L bucket, and shipped overnight to the University of Tennessee in Knoxville, TN. The large soil clods were gently separated by hand to pass through a 19-mm sieve to remove stones, large residues, and earthworms. The soil was air-dried for five days and then dry sieved with a rotary sieve shaker at 30 rpm for five minutes and weighed to obtain the targeted particle size distribution based on gradations of 8 mm, 4.75 mm, 2 mm, 1.7 mm, 1.4 mm, 1.18 mm, 0.85 mm, 0.6 mm, 0.25 mm, and 0.075 mm. The dry mean weight diameter (DMWD) was calculated from the dry sieving using the following equation (Bavel, 1950):

$$\mathrm{DMWD} = \sum_{i=1}^{n} \bar{x}_i w_i \tag{3-1}$$

where $\bar{x}_i$ is the mean diameter of each size class (mm), w_i is the mass proportion of each size class, and *n* is the number of size classes over the whole soil.

The DMWD index reflects aggregate properties and higher DMWD suggests stronger soil particle cohesion in aggregates (Skidmore and Layton, 1992). The sieved soils were recombined into four size fractions, including extra-large macroaggregates (8-19 mm), large macroaggregates (2-8 mm), small macroaggregates (0.075-2 mm), and fines (<0.075 mm, silt + clay sized fraction), herein as X, L, S, and F fractions, respectively.

Aggregate Stability Index Determination

The initial aggregate stability of the X, L, and S fractions was tested in the laboratory using simulated rainfall following the procedure described in Wacha et al. (2018) and Hou et al. (2018). Specifically, 30-50 g of X, L, and S macroaggregates were evenly distributed atop 8-, 2- and 0.075-mm sieves with catch pans below each to collect the slaked material. The samples were exposed to 5 min of simulated rainfall with a 60-mm h^{-1} intensity (Figure C-1). The rainfall was generated by a Norton ladder multiple intensity rainfall simulator designed by the National Soil Erosion Research Lab of the U.S. Department of Agriculture – Agricultural Research Service. The rainfall simulator has an aluminum frame (2.5 m [h] × 2.7 m [l] × 1.5 m [w]) with oscillating VeeJet nozzles suspended on the top (Figure C-1a). Water was continuously pumped from a tank to the nozzles with controlled pressure to provide spherical raindrops in a median diameter of 2.25-2.75 mm and a terminal velocity of 6.8-7.7 m s^{-1}, which mimic the natural distribution and force of raindrops for a heavy thunderstorm in the U.S. Midwest (Abban et al., 2017). After each 5-min rainfall, the slaked aggregates, which were washed through the sieve, were transferred into pre-weighed cups and oven-dried at 60°C for 24 h. The aggregate stability index (ASI) was calculated using the following equation (Hou et al., 2018; Wacha et al., 2018):

$$ASI = \frac{\mathrm{M}_r}{\mathrm{M_t}} = \frac{\mathrm{M_t} - \mathrm{M_s}}{\mathrm{M_t}} \tag{3-2}$$

where M_t is the dry mass of total aggregate sample (g); M_s is the dry mass of soil that passed through the sieve upon raindrop disruption (g; Figure C-1d); M_r is the dry mass of soil that remained on the sieve and are resistant to raindrop breakdown (g; Figure C-1b).

REE Labeling of Soil Aggregates

Four REE powders, purchased from the People's Republic of China, were used to tag different aggregate size classes with a different REE assigned to each size fraction (Ytterbium, Yb → X; Erbium, Er → L; Gadolinium, Gd → S; Samarium, Sm → F). The purity of each REE oxide was >99.9%. The median diameter (D_{50}) of the powders ranged from 2.19 to 3.61 μm, and the density between 7 and 9 g cm^{-3}. The background concentrations of the four REEs in the collected field soil were all less than 10 ppm.

The REE powders were sorbed to their assigned aggregate fractions in a mass ratio of 1:10 (REE: Soil), using the repeated wet-dry cycle method in Polyakov et al. (2004). Each aggregate fraction was initially distributed evenly over an aluminum pan (60 cm [l] × 30 cm [w] × 2.54 cm [h]). The soil was misted with distilled water to 15% of soil weight. The REE powder was then sprinkled over the moist soil and gently mixed with the soil aggregates using a spatula. The mixture of aggregates and REE was allowed to air-dry for 24 h at room temperature before repeating. This wet-dry procedure was repeated five times to secure the bonding of REE with aggregates. Subsamples of ~15 g were saved for determining the baseline REE concentration of the tagged aggregates. The four labeled aggregate fractions were finally recombined to match the aggregate size distribution determined with dry sieving, as mentioned above (i.e., 43% X, 39% L, 16% S, and 2% F).

Aggregate Application and Soil Sampling

On May 29, 2019 (Day 0), the REE labeled aggregates were uniformly broadcast over a rectangular plot located in the sampled field using a calibrated 56-cm wide lawn spreader. This was one week after planting, so the plants had not emerged yet. The plot was 7.3 m [l] × 5 m [w] with a 0.6% slope. The longer side of the plot aligned with the cornrows and the flow pathways (Figure 3-1a). During the experiment, 70 mm of rainfall was delivered to the field in three distinct periods (Day 0 – Day 2; Day 14 – Day 15; Day 21 – Day 26). Soil sample collection from the tagged plot occurred on Day 3 and Day 26 after 3 and 7 rain events. Five samples were collected along three downslope transects at equal 1.8 m spacing. Surface soil samples were carefully collected in a uniform volume (12.8 cm × 9.2 cm × 1 cm deep) using a sharp knife without affecting the soil structure. Each soil sample was bagged and stored in a cooler and brought immediately to the laboratory in Knoxville, TN. The soil samples were oven-dried at 60°C for 24 h and then separated into the same four size fractions (X, L, S, and F) as before labeling using an orbital shaker at 30 rpm. Each aggregate fraction was crushed into fine powders using a wooden rolling pin. Subsamples of ~15 g were used to measure the SOC concentration with visible and near-infrared spectroscopy (Chapter 2). A 2-g subsample was taken for REE analysis.

Field Measurements and Rain Power Determination

Over the one month in situ experiment, the rainfall amount, volumetric soil water content, and CO_2 flux were measured every 15 min by an eddy covariance flux tower (Campbell

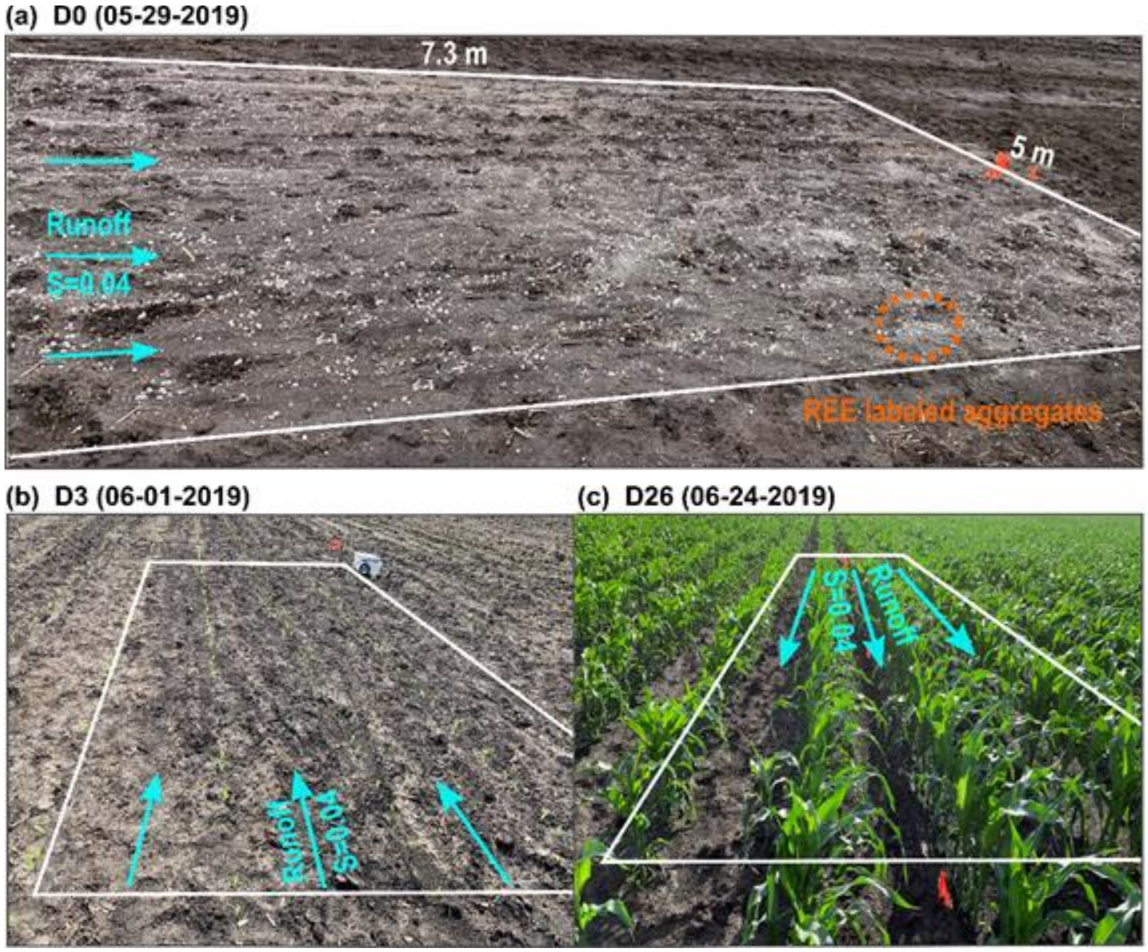

Figure 3-1. Plan view of the field plot from different angles on days (a) 0, (b) 3, and (c) 26. The cyan arrows denote the runoff directions.

Scientific, Inc.), which was 2 km northeast of this field. The CO_2 flux was used as a proxy to assess the microbial activity in the soil. During the inter-rain periods, most of the days were sunny with temperatures ranging between 16-28 °C. The corn plants evolved from the seed germination to the emergence of eight leaves. Images of the corn plants were taken periodically on days 0, 3, 22, 23, 24, 26, 27, 28, 29, and the proportions of the plot surface covered by corn plants were determined using the ImageJ software (NIH). A strong power-law relationship ($y = 0.57x^{1.36}$, R^2=0.99, P<0.0001) was obtained between the days of the experiment (independent variable, x) and the proportion of the plot surface covered by corn plants (dependent variable, y), allowing this equation to be used to estimate the corn plant coverage for the days without images (Figure C-2).

Rain power (R, W m^{-2}), defined as the effective raindrop kinetic energy transferred to the soil particles, was calculated using the Gabet and Dunne (2003) formula, where the effect of plant cover on dissipating rain power was taken into account:

$$R = \frac{\rho I v^2 (1 - C_c)\cos\theta}{2} \qquad \text{3-3}$$

where ρ is water density (998 kg m^{-3} for 22 °C temperature), I is rainfall intensity (m s^{-1}), v is raindrop velocity (m s^{-1}), C_c is the proportion of the surface plot covered by corn plants, θ is the plot slope in degrees.

The raindrop velocity was determined as a function of rainfall intensity (Schmidt, 1992):

$$v = 6.6I^{0.07} \qquad \text{3-4}$$

REE Analyses

The REEs were extracted from a subsample of each aggregate fraction by acid digestion following ASTM 3050B (USEPA, 1996). A 2-g soil sample was placed in a 250-mL glass beaker and 10 mL of 70 wt% HNO^3 was added. The mixture was refluxed in a water bath at 85°C for 2 h with a ribbed watch glass on top of the beaker to prevent REE loss from evaporation. After cooling to less than 70°C, 2 mL of distilled water was added, followed by the slow addition of 3 mL of 30 wt% H^2O^2 to remove organic material. After effervescence subsided, another 7 mL of 30 wt% H^2O^2 was added, and the solution was refluxed in an 85°C water bath for 2 h. Then, 5 mL of 36 wt% HCl were added and the solution was refluxed at 85°C for 2 h in the water bath. After a 24 h waiting period at room temperature, the solution was filtered through 47-mm Whatman filter paper, eluting with 5 mL of distilled water. The final 10-15 mL sample extract was transferred into a conical sterile polypropylene centrifuge tube and sealed with parafilm. The concentrations of REEs in the sample solution were analyzed on an inductively coupled plasma mass spectrometry (ICP-MS) Agilent 8900 ICP-QQQ (Santa Clara, CA) at the Arizona Laboratory for Emerging Contaminants (ALEC) with a detection limit of 5×10^{-5} ppm.

Aggregate Turnover

This study tracked the mass flow out of X, L, and S fractions following six potential breakdown pathways (a-f) and the mass flow into X, L, and S fractions following six potential formation pathways (g-l; Figure C-3). The aggregate transfers along each pathway from time t_1 to t_2 can be described in a discrete transfer matrix $K_{(t_2-t_1)}$ according to Peng et al. (2017):

$$K_{(t_2-t_1)} = \begin{bmatrix} 1-a-d-f & i & k & l \\ a & 1-i-b-e & h & j \\ d & b & 1-k-h-c & g \\ f & e & c & 1-l-j-g \end{bmatrix} \quad 3\text{-}5$$

where a to l are the changes of proportions of aggregates falling into sizes X, L, S, and F from time t_1 to t_2.

The four aggregate size fractions were assumed to be labeled homogeneously by different REEs and the transfer matrix $K_{(t_2-t_1)}$ of aggregates can be calculated from the changes of REE mass from time t_1 to t_2:

$$K_{(t_2-t_1)} = M_{REE(t_2)} M^{-1}_{REE(t_1)} \quad 3\text{-}6$$

where $M_{REE(t_1)}$ is the mass of REE in each size fraction at time t_1 (g) and $M_{REE(t_2)}$ is the mass of REE in each size fraction at time t_2 (g).

To determine the mass of REEs that remained in each aggregate size fraction over the plot on each sampling date, the plot (7.3 m [l] × 5 m [w]) was divided into 15 subplots centered on the sampling locations. We assume that each aggregate size fraction was uniformly distributed over each subplot and had the same REE concentration as the aggregates at the subplot's center. Thus, the total mass of REEs in each aggregate size fraction in the whole tagged plot at time t can be calculated as the summation of REEs mass from the 15 subplots:

$$M_{REE(t)} = \sum_{i=1}^{15} \frac{M_{AGG.(t)} C_{REE(t)} A_{subplot(i)}}{A_{sample}} \quad 3\text{-}7$$

where $M_{REE(t)}$ is the mass of REEs in each aggregate size fraction at time t (g), $C_{REE(t)}$ is the concentration of REE in each aggregate size fraction (ppm) and calculated as the measured concentration of REE subtracted by the background concentration of REE in untagged soils, $M_{AGG.(t)}$ is the mass of each aggregate size fraction (g), $A_{subplot(i)}$ is the area of subplot i (m^2), and A_{sample} is the area of soil sampling (121.6 cm^2).

The mass of each aggregate size fraction can be described as a vector:

$$M_{AGG.(t)} = \begin{bmatrix} X_t \\ L_t \\ S_t \\ F_t \end{bmatrix} \tag{3-8}$$

where, e.g., X_t is the mass of extra-large macroaggregates at time t (g).

Due to the occurrence of mass transfer between the four aggregate fractions during the experiment, each aggregate fraction could have four REE tracer signatures on each sampling date. Therefore, the concentration of REE at time t, $C_{REE(t)}$, can be described as a matrix:

$$C_{REE(t)} = \begin{bmatrix} [Yb_X] & [Er_X] & [Gd_X] & [Sm_X] \\ [Yb_L] & [Er_L] & [Gd_L] & [Sm_L] \\ [Yb_S] & [Er_S] & [Gd_S] & [Sm_S] \\ [Yb_F] & [Er_F] & [Gd_F] & [Sm_F] \end{bmatrix} \tag{3-9}$$

where, e.g., $[Yb_X]$ is the concentration of Yb in extra-large macroaggregates (ppm) at time t.

The product of $M_{AGG.(t)}C_{REE(t)}$ can be described as:

$$M_{AGG.(t)}C_{REE(t)} = \begin{bmatrix} X_t[Yb_X] & X_\mathrm{t}[Er_X] & X_\mathrm{t}[Gd_X] & X_\mathrm{t}[Sm_X] \\ L_\mathrm{t}[Yb_L] & L_\mathrm{t}[Er_L] & L_\mathrm{t}[Gd_L] & L_\mathrm{t}[Sm_L] \\ S_\mathrm{t}[Yb_S] & S_\mathrm{t}[Er_S] & S_\mathrm{t}[Gd_S] & S_\mathrm{t}[Sm_S] \\ F_\mathrm{t}[Yb_F] & F_\mathrm{t}[Er_F] & F_\mathrm{t}[Gd_F] & F_\mathrm{t}[Sm_F] \end{bmatrix} \tag{3-10}$$

The turnover rate (TR, day^{-1}) of each aggregate fraction over the experiment from time t_1 to t_2 is calculated using the following equation:

$$TR(X) = \frac{|a_{t_1} + d_{t_1} + f_{t_1} - \left(a_{t_2} + d_{t_2} + f_{t_2}\right)|}{t_2 - t_1} \tag{3-11}$$

$$TR(L) = \frac{|i_{t_1} + b_{t_1} + e_{t_1} - \left(i_{t_2} + b_{t_2} + e_{t_2}\right)|}{t_2 - t_1} \tag{3-12}$$

$$TR(S) = \frac{|k_{t_1} + h_{t_1} + c_{t_1} - (k_{t_2} + h_{t_2} + c_{t_2})|}{t_2 - t_1} \tag{3-13}$$

$$TR(F) = \frac{|l_{t_1} + j_{t_1} + g_{t_1} - (l_{t_2} + j_{t_2} + g_{t_2})|}{t_2 - t_1} \tag{3-14}$$

for more information on the transfer pathways and the Peng et al. (2017) aggregate turnover model, see Appendix A.

Statistical Analyses

Analysis of variance (ANOVA) with Tukey's HSD (honestly significant difference) test was performed at each sampling date to identify the differences among the means of measured variables (aggregate size distribution, DMWD, and SOC concentration) across the four aggregate size fractions. Tukey's HSD test was applied at a given aggregate size fraction to assess the differences among the means of size distribution and DMWD across sampling dates. Independent samples t-test was used to identify the differences between SOC concentration on Day 3 and Day 26. All tests were implemented with IBM SPSS Statistics 27 at a significance level of 0.05.

Results

Relationship between Rainfall, Soil Water Content, and CO_2 Flux

As noted above, over the 26-day experiment, 70 mm of rainfall was delivered to the field in three distinct periods: Day 0 – Day 2, Day 14 – Day 15, and Day 21 – Day 26 (Figure 3-2a). The first period consisted of three scattered rain events providing a total of 0.051 W m^{-2} of rain power on the soil particles. The heaviest rainfall occurred on Day 0 (the night following the aggregate broadcast) with the highest intensity of 18.29 mm h^{-1} and rain power of 0.02 W m^{-2} (Table B-1). In the second period, two rain events exerted a total of 0.062 W m^{-2} of rain power on the soil particles. The heaviest rainfall occurred on Day 14 with the highest intensity of 34.56 mm h^{-1} and rain power of 0.033 W m^{-2} (Table B-1). The third series of rainfall comprised five small events exerting a total of 0.057 W m^{-2} of rain power on the soil particles. The heaviest rain in this period occurred on Day 21 with the highest rainfall intensity of 12.19 mm h^{-1} and rain power of 0.008 W m^{-2} (Table B-1).

Both soil water content and soil CO_2 fluxes spiked following each rain event (Figure 3-2b). There was a plateau of soil water content in the first rain period (0-3 days), ranging between 32-35% before gradually decreasing to the field capacity by Day 5 (31%). In the subsequent dry period, the soil water content continued decreasing until it reached the lowest value of 23% and then rebounded up to the field capacity immediately following the rain on Day 14. During the third rain period (21-26 days), the soil water content fluctuated slightly above the field capacity (31-36%), where the peaks were in concert with the rainfall. The REE-labeled aggregates in the field consequently underwent a wetting phase between Day 0 – Day 3, a drying phase between Day 4-Day 14, and a rewetting phase between Day 15 - Day 26. The CO_2 flux was constantly near zero during the dry periods but spiked immediately following the rainfall events (Figure 3-2b). The CO_2 fluxes in the rain periods of Day 0 – Day 3 and Day 21 – Day 26 were dominated by positive values (10 to 150 mg m^{-2} s^{-1}) where the soil water content was around 37%, indicating that CO_2 emission by soil and plant respirations is greater than CO_2 storage through photosynthesis. The CO_2 fluxes during the rain period of Day14-Day15 were dominated by negative values (-7 to -58 mg m^{-2} s^{-1}) where the soil water content was less than 31%, indicating that the CO_2 storage is greater than CO_2 release.

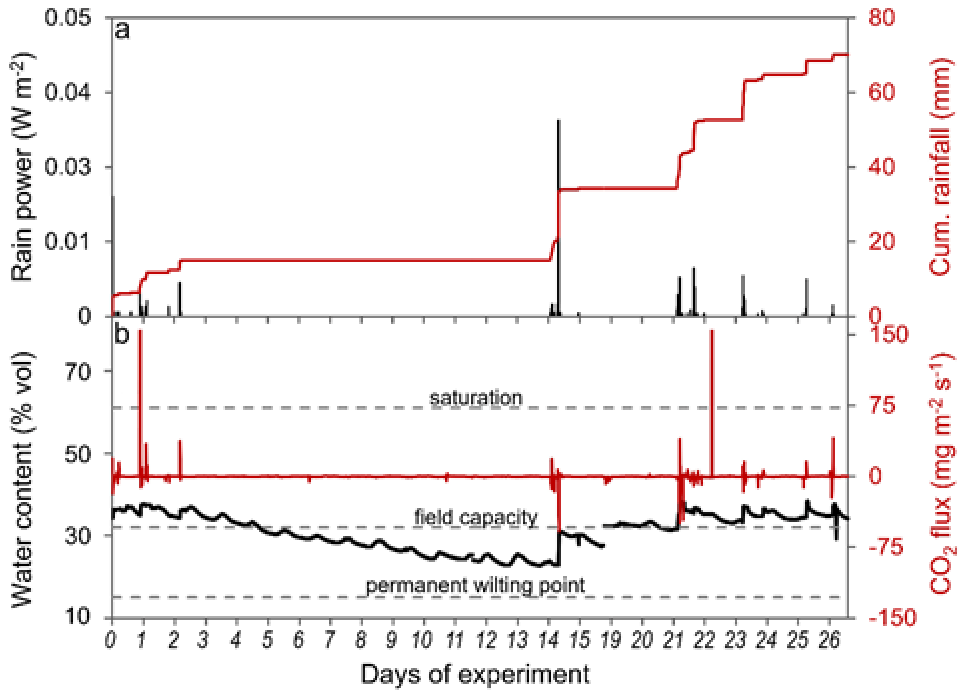

Figure 3-2. Rain power, cumulative rainfall, volumetric soil water content, and CO_2 fluxes daily at the 5-cm soil depth of the experiment site. Saturation was determined based on the average soil bulk density measured in this field; field capacity and permanent wilting point were obtained from Salter and Williams (1965) for silty cay loam soils.

Aggregate Size Distribution

The aggregate size distribution and DMWD of the bulk soil across the sampling period are shown in Figure 3-3. The proportion of extra-large macroaggregates in the bulk sample decreased from 43% on Day 0 to 37% on Day 3 ($P = 0.303$) and then increased significantly to 52% on Day 26 ($P = 0.008$). Likewise, the proportion of large macroaggregates decreased significantly from 39% on Day 0 to 24% on Day 3 ($P = 0.001$) then increased to 32% on Day 26 ($P = 0.064$). Conversely, the proportion of small macroaggregates in the bulk sample increased initially from 16% on Day 0 to 37% on Day 3 ($P < 0.0001$) and then dropped back to 16% on Day 26. Finally, the proportion of the fines was < 2% on all sampling dates. Comparing to the decreased mass proportion with decreasing aggregate sizes on Day 0 (i.e., X>L>S>F), the measured distribution of the mass proportion was altered on Day 3 with the small macroaggregates having the highest proportion, followed closely by the extra-large macroaggregates, then the large macroaggregates and the fines. The distribution on Day 26 was similar to that on Day 0. The DMWD of the bulk soil decreased significantly from an initial value of 7.9 mm on Day 0 to 6.6 mm on Day 3 ($P = 0.01$) and then increasing to 8.7 mm on Day 26 ($P < 0.0001$).

Aggregate Transfers

The relative aggregate fraction transfers were examined using the REE mass changes over the sampling period and the model by Peng et al. (2017) (Figure 3-4). In terms of aggregate breakdown, there were proportionally higher transfers on Day 3 (17% ± 12%) than on Day 26 (3% ± 2.5%). These transfers were observed to be higher between neighboring size fractions than between non-neighboring size fractions. For aggregate formation, there was less incorporation of smaller macroaggregates into larger macroaggregates on Day 3 (11% ± 2%) than on Day 26 (26% ± 8%). However, the incorporation of fines into larger aggregate sizes was greater on Day 3 (29% ± 19%) than on Day 26 (8% ± 6%). On Day 26 (Figure 3-4b), the small macroaggregates and fines had higher incorporation into extra-large macroaggregates than into their neighboring size fractions on Day 3 (Figure 3-4a). Overall, extra-large, large, and small macroaggregates exhibited higher transfers through breakdown (21-40%) than through formation (6-13%) on Day 3, while on Day 26, the formation transfers were higher (Table 3-1). Additionally, extra-large macroaggregates had the greatest mass changes through both breakdown and formation, followed by large macroaggregates and small macroaggregates (Table 3-1).

The efficacy of REEs in tracking the aggregate transfers was verified by comparing the modeled and measured aggregate size distribution (Figure 3-5). Regardless of the aggregate size, a global linear relationship (close to the 1:1 line; $R^2=0.798$; $P<0.01$) was obtained, indicating that REEs can be used as an efficacious tracer for studying aggregate dynamics in the field conditions. Across the four aggregate size fractions, REEs performed better as tracers for predicting the extra-large, large, and small macroaggregate dynamics than in predicting the fine particle dynamics.

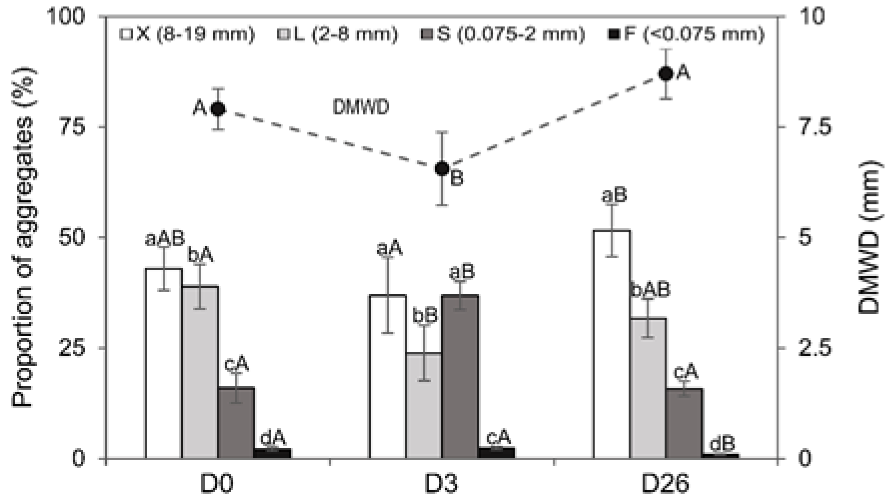

Figure 3-3. Mass proportion of the four aggregate fractions and DMWD of the whole soil on days 0, 3, and 26 of the experiment. Different lowercase letters denote significant differences at P<0.05 among aggregate fractions on the same sampling date. Different uppercase letters denote significant differences at P<0.05 among sampling dates for the same aggregate fraction.

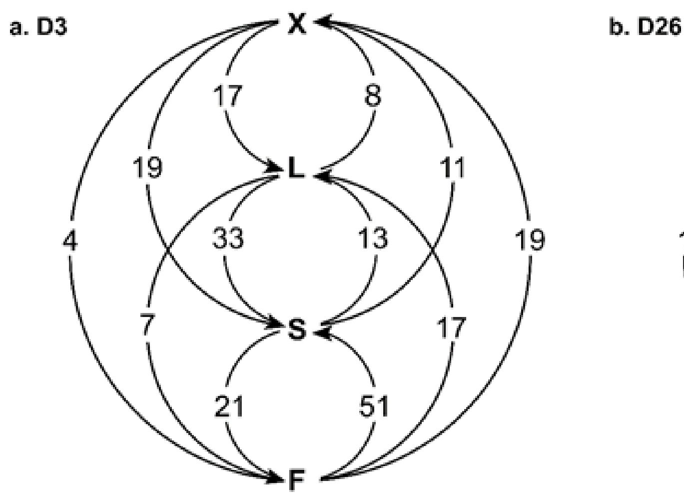

Figure 3-4. The cumulative transfers between the four aggregate fractions along the breakdown and formation pathways on Day 3 and Day 26. X, L, S, and F indicate the extra-large macroaggregates (8-19 mm), large macroaggregates (2-8 mm), small macroaggregates (0.075-2 mm), and fines (<0.075 mm). Values in arrows are % of the mass of REEs in this size fraction relative to its initial mass at the start of the experiment on Day 0.

Table 3-1. Cumulative changes in proportions of each aggregate fraction through breakdown and formation processes and the turnover time of the four aggregate fractions.

Aggregate fractions	Breakdown (%)		Formation (%)		Turnover rate (day^{-1})		Turnover time (day)	
	D3	D26	D3	D26	D3	D26	D3	D26
X (8-19 mm)	39	24	13	42	0.131	0.009	8	106
L (2-8 mm)	40	5	6	7	0.161	0.014	6	70
S (0.075-2 mm)	21	1	7	0.4	0.151	0.019	7	53
F (<0.075 mm)					0.288	0.009	3	110

The F fraction (<0.075 mm) could not be considered in the breakdown and formation processes because no fractions smaller than F were investigated in this study.

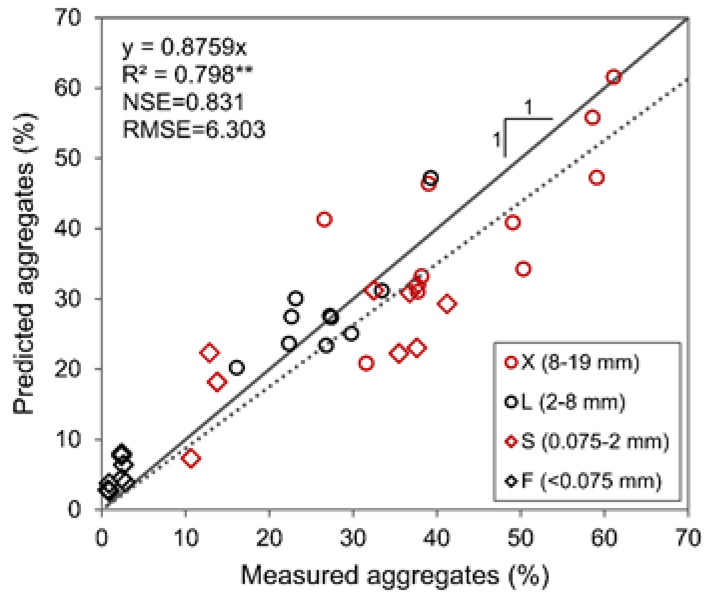

Figure 3-5. Relationship between the predicted aggregate class distribution based on the proportion of REEs transfers between any two aggregate size fractions and the measured aggregate class distribution from dry sieving.

The aggregate turnover rates decreased significantly over the sampling period (Table 3-1). The turnover rates ranged from 0.131 to 0.288 day^{-1} during the first 3-day time frame and from 0.009 to 0.019 day^{-1} over the entire 26-day time frame. The aggregate turnover time, which is the reciprocal of the aggregate turnover rate, increased as the sampling period increased. In the first 3-day time frame, the aggregate turnover times ranged from 3-8 days with a small difference among the four size fractions. Over the 26-day time frame, the turnover times increased in the order of small macroaggregates (53 days) < large macroaggregates (70 days) < extra-large macroaggregates (106 days) < fines (110 days).

SOC Distribution in Aggregates

The mean SOC concentration in extra-large macroaggregates decreased significantly from 2.78% on Day 3 to 2.63% on Day 26 ($P = 0.003$; Figure 3-6). No significant changes in SOC concentrations were observed in large macroaggregates, small macroaggregates, and fines from Day 3 to Day 26 ($P > 0.05$; Figure 3-6). As a result, the size-weighted SOC concentration was slightly lower on Day 26 (2.71%) than on Day 3 (2.84%). On a given sampling date, small macroaggregates (3.01% ± 0.03%) had significantly higher ($P < 0.01$) SOC concentration than extra-large macroaggregates, large macroaggregates, and fines (2.68% ± 0.03%), indicating the preferential accumulation of SOC in small macroaggregates.

Discussion

Aggregate Dynamics and Effects of Raindrop Impact and Wetting-Drying

Aggregate dynamics include breakdown, formation, and stabilization. The mechanisms behind these processes have been mainly studied in the laboratory under controlled conditions. To the best of our knowledge, the present study is the first study that directly deciphers aggregate breakdown and formation interactions under field conditions using the trade-off of REE between different aggregate size fractions. Past incubation studies have focused on the role of microbes in aggregate dynamics (Martens, 2000), neglecting the importance of physical processes such as raindrop impacts, runoff, and wetting-drying cycles (Six et al., 2004). The tagged aggregates that were applied to the field in this study underwent series of rainfall impacts during a wetting-drying-wetting cycle. The aggregates broke down more than combined during the first 3 days as they were exposed to persistent impacts by raindrops with nearly no protection from the corn plants (< 1.5% coverage). The swelling behavior of clay upon wetting may also cause the disintegration of aggregates as the clay (32%) and water (32-35%) status of the studied soil was within the reported soil swelling limit (clay 30-65%; water 20-40%) by Meisina (2006).

In contrast to what was observed on Day 3, there was higher incorporation of smaller-sized aggregates into larger aggregates, especially into the extra-large macroaggregates on Day 26. The increased DMWD of the bulk soil on Day 26 also indicates more formation

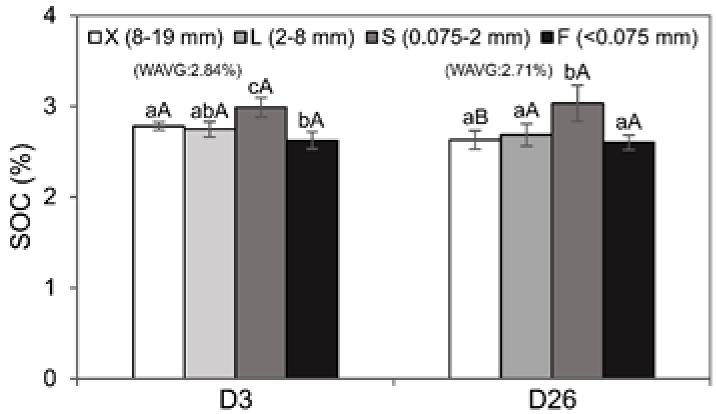

Figure 3-6. SOC concentration in the four aggregate fractions on days 3 and 26 of the experiment. Different lowercase letters denote significant differences at $P<0.05$ among aggregate fractions on the same sampling date. Different uppercase letters denote significant differences at $P<0.05$ between sampling dates for the same aggregate fraction.

of larger aggregates. Although the aggregates experienced dissipated rain power resulting from the growing corn plants, the higher aggregate formation is likely driven by the complex interactions between observed wetting-drying events and the dynamics of microbial communities and their aggregating agents (Cosentino et al., 2006). Shrinking and cracking may occur in the pre-swollen soil as they dried between Day 4 – Day 14, promoting new aggregate formation (Tang et al., 2011). The soil water content continued to decrease during the period until it reached 23%, where clay shrinkage is likely to occur according to the reported shrinking limit of 10-20% for water (Meisina, 2006; Mishra et al., 2008). Consistent with previous studies (Borken et al., 2003; Meisner et al., 2013; Navarro-García et al., 2012), the subsequent rainfall rewetting between Day 15 – Day 26 induced multiple pulses of CO_2 release suggesting increased microbial activities and crop plant respiration, mobilizing carbon physically protected in aggregates, and releasing polysaccharides and other exudates (Borken and Matzner, 2009; Liang et al., 2003; Manzoni et al., 2012), all of which in turn increase aggregate formation and stabilization through adsorption or physical gluing of soil particles into aggregates according to the reported shrinking limit of 10-20% for water (Meisina, 2006; Mishra et al., 2008). Consistent with previous studies (Borken et al., 2003; Meisner et al., 2013; Navarro-García et al., 2012), the subsequent rainfall rewetting between Day 15 – Day 26 induced multiple pulses of CO_2 release suggesting increased microbial activities, mobilizing carbon physically protected in aggregates, and releasing polysaccharides and other exudates (Borken and Matzner, 2009; Liang et al., 2003; Manzoni et al., 2012), all of which in turn increase aggregate formation and stabilization through adsorption or physical gluing of soil particles into aggregates (Chaney and Swift, 1986). Particularly, the CO_2 flushes were triggered at a water content of 37%, which falls in the reported range of 25-37%, where most microbial populations are likely to have the maximum activity responses (Manzoni et al., 2012).

Variation in Aggregate Turnover across the Size Fractions

The amount of soil exchange between the four aggregate size fractions varied within the sampling period, demonstrating the dynamism of these processes. Consistent with previous laboratory incubation studies (Peng et al., 2017; Wang et al., 2020), greater portions of extra-large and large macroaggregates were observed to disintegrate into lower-level size groups compared to small macroaggregates, indicating that extra-large and large macroaggregates break down more easily than small macroaggregates upon the impacts of rainfall. The aggregate stability index (ASI) tests with simulated rainfall produced similar values as other studies in the region (e.g., Wacha et al., 2018) confirming these observations, as extra-large and large macroaggregates (0.81 ± 0.16; 0.94 ± 0.01) had lower ASI values on average than small macroaggregates (0.98 ± 0.01; Figure 3-7). The ASI values reflect the ability of aggregates to withstand disruptive forces of raindrop impact and other authors also found that large macroaggregates are more vulnerable to raindrop breakdown than small macroaggregates (Hou et al., 2018). The

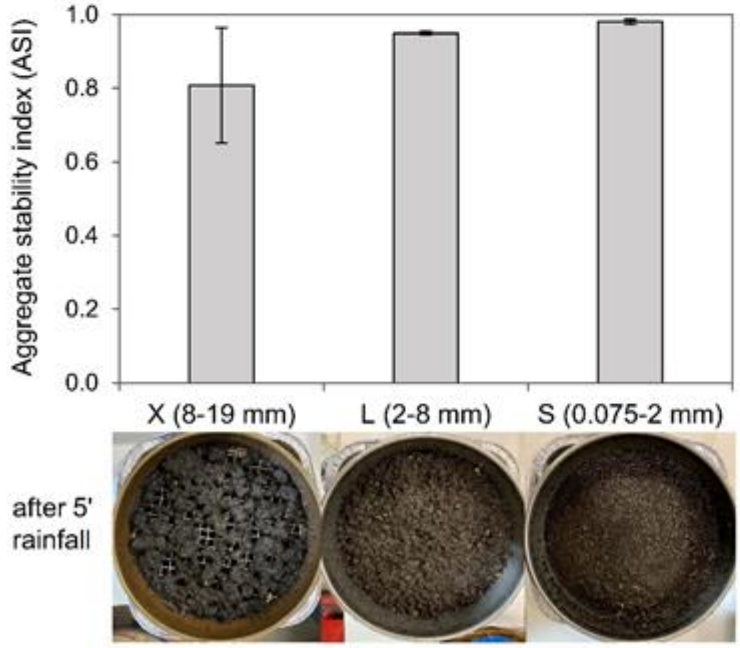

Figure 3-7. Comparison of aggregate stability index (ASI) and retained material of extra-large (8-19 mm), large (2-8 mm), and small (0.075-2 mm) macroaggregates.

differences in stability against the raindrop breakdown between large and small macroaggregates are rooted in their different soil particle composition and binding agents (Oades and Waters, 1991; Tisdall and Oades, 1982) as large macroaggregates are small macroaggregate clusters loosely held together by roots and fungal strands resulting in an unstable structure (Blanchart et al., 2004); while small macroaggregates are composed of microaggregates and fines that are glued more persistently by cations, bacterial, microbial and plant exudates.

Aggregate turnover rate integrates both breakdown and formation rates (De Gryze et al., 2006; Peng et al., 2017). The aggregate turnover times over the entire experiment ranged from 53-110 days, which are broadly in accordance with reported values (e.g., 19-95 days by Plante et al. (2002); 30-88 days by De Gryze et al. (2006); 54-130 days by Peng et al. (2017); and 41-168 days by Wang et al. (2020)). Our results showed that the turnover rates of all aggregate size fractions decreased dramatically on Day 26 compared to on Day 3, indicating aggregate stabilization. Other studies also revealed decreasing aggregate turnover rates over time and the decreasing trends follow an exponential decay (De Gryze et al., 2006; Peng et al., 2017; Wang et al., 2020). Although the first series of rain events reduced the amount of extra-large and large macroaggregates, they were likely to become slake-resistant after a relatively long drying-wetting cycle due to the presence of larger corn plants and more rain power reduction (Denef et al., 2001b). In addition to time, our results demonstrated that the aggregate turnover rate is size-dependent. Small macroaggregates had the fastest turnover rate amongst the four studied size fractions due to the more active microbial activities (Jiang et al., 2018). The fast turnover rate of small macroaggregates has also been reported in previous laboratory incubations (De Gryze et al., 2006; Peng et al., 2017; Rahman et al., 2019) and field experiments (Jastrow, 1996; Kay et al., 1988; Plante et al., 2002).

Relation to Carbon Dynamics

There is a consensus that aggregate turnover regulates SOC dynamics by controlling carbon release and storage in different size fractions (De Gryze et al., 2006; Segoli et al., 2013; Six et al., 2001a; Six et al., 2000b). The significantly higher SOC in smaller macro-aggregates may be partly responsible for the greater aggregate stability measured with the simulated rainfall (Figure 3-7), and similar results were reported by other researchers (Abid and Lal, 2008; Angers et al., 1997; de Tombeur et al., 2018; Elliott, 1986; Six et al., 2000c). The abundant SOC in smaller macroaggregates is primarily ascribed to their large surface area and strong binding agents (cations, bacterial, microbial and plant exudates), which can hold organic material tightly and withstand disruptive forces (Oades, 1984; Papanicolaou et al., 2015; Tisdall and Oades, 1982). Hou et al. (2018) found that raindrop-stable small macroaggregates contain more than double the SOC portion than slaked ones, which is the opposite of that observed for large macroaggregates. The relatively fast turnover rate of small macroaggregates may also promote carbon accumulation through increased microbial anabolism and new carbon mineralization

(Liang et al., 2017; Six et al., 2004). Despite this understanding, only small changes of SOC concentration were observed in all aggregate size fractions from Day 3 to Day 26, implying a stable state of SOC over the experiment, which is probably because the 26-day time frame is not long enough to capture SOC changes as the turnover time of SOC is generally months to a few years (Metherell, 1993).

Limitations and Implications

One limitation in this study is that mobilization of the aggregates by runoff was not considered. Although the rainfall was relatively light, the runoff was visually limited, and the field is relatively flat, about 40% of the applied REE-labeled aggregates were mobilized and deposited downslope (Table B-2). The dynamics of the downslope aggregates could not reasonably be considered because the mobilized material likely distributed nonuniformly in space, leading to difficulties in determining aggregate dynamics through REE tracing. Additionally, a small portion of aggregate fragments may have transported vertically into the soil column beyond the sampling depth of 1 cm as cracks present on the surface or blown away by the wind (field observation). Nonetheless, our results indicate that enough REE-tagged material remained in the source plot to track the aggregate dynamics. The most likely mobilized particles were the slaked finer particles, which would underestimate the proportions within the breakdown processes but not affect the incorporation proportions. Furthermore, we could not collect more soil samples between Day 3 and Day 26, especially after the second series of rain events, owing to inconvenient transportation and workforce shortage. Last, the system is not static, and differences in rainfall characteristics and plant cover may also play a role. In the future, more measurements at shorter time intervals are needed to obtain a more reliable estimate of aggregate turnover times, as also suggested by De Gryze et al. (2006).

Conclusions

The present study has investigated the interchangeable breakdown and formation of soil aggregates in the field following rain events and wetting-drying cycles using REE tracing and supported with simulated rainfall tests and eddy flux tower measurements. A net breakdown occurred in the larger aggregate size fractions following an initial series of rain events due to disruptive forces of raindrop impact and air slaking, which led to a decreased amount of larger macroaggregates and increased amounts of small macroaggregates and fines. After a subsequent dry period and another two series of rain events, there was a net formation of extra-large and large macroaggregates suggesting aggregation due to increased particle binding caused by clay shrinkage upon drying and microbial activity flushes upon rewetting. As a result, aggregate turnover rates decreased with increasing time. The ASI values increased as the aggregate size class decreased because of the type of binding agents prevalent in the different classes. The more involvement of microbial activity in smaller macroaggregates resulted in a faster turnover rate than larger macroaggregates. Additionally, small macroaggregates contained the highest SOC concentration among the studied size fractions, ascribed to their higher aggregate stability and faster turnover rate which induced a fast storage rate. For the first time, this study realized applying a laboratory-established REE tracing and modeling approach to the field condition and provides new insights into understanding and modeling aggregate structural dynamics under diverse environmental stressors such as raindrop impact and weather-controlled wetting-drying cycles.

Acknowledgments

This research was supported by the National Science Foundation for the IML-CZO project [grant number EAR1331906], a multi-institutional collaborative effort. The REE concentrations were analyzed with ICP-MS by the Arizona Laboratory for Emerging Contaminants (ALEC) at the University of Arizona, Tucson, AZ. The authors would like to thank Dr. Andrew Stumpf from the Illinois State Geological Survey and Dr. Bruce Rhoads from the University of Illinois Urbana-Champaign for assisting the field experiment. The first author was part of the China-UT EcoPartnership Scholars Program and is grateful for the support from the China Scholarship Council.

References

Abban, B.K.B., Papanicolaou, A.N., Giannopoulos, C.P., Dermisis, D.C., Wacha, K.M., Wilson, C.G., Elhakeem, M., 2017. Quantifying the changes of soil surface microroughness due to rainfall impact on a smooth surface. Nonlin. Processes Geophys. 24(3), 569-579.

Abid, M., Lal, R., 2008. Tillage and drainage impact on soil quality: I. Aggregate stability, carbon and nitrogen pools. Soil and Tillage Research 100(1), 89-98.

Angers, D.A., Recous, S., Aita, C., 1997. Fate of carbon and nitrogen in water-stable aggregates during decomposition of 13C15N-labelled wheat straw in situ. European Journal of Soil Science 48(2), 295-300.

Bavel, V., 1950. Mean weight-diameter of soil aggregates as a statistical index of aggregation 1. Soil Science Society of America Journal 14(C), 20-23.

Blanchart, E., Albrecht, A., Brown, G., Decaens, T., Duboisset, A., Lavelle, P., Mariani, L., Roose, E., 2004. Effects of tropical endogeic earthworms on soil erosion. Agriculture, Ecosystems Environment international 104(2), 303-315.

Borken, W., Davidson, E.A., Savage, K., Gaudinski, J., Trumbore, S.E., 2003. Drying and wetting effects on carbon dioxide release from organic horizons. Soil Science Society of America Journal 67(6), 1888-1896.

Borken, W., Matzner, E., 2009. Reappraisal of drying and wetting effects on C and N mineralization and fluxes in soils. Global Change Biology 15(4), 808-824.

Cao, Q., Song, X., Wu, H., Gao, L., Liu, F., Yang, S., Zhang, G., 2020. Mapping the response of volumetric soil water content to an intense rainfall event at the field scale using GPR. Journal of Hydrology 583, 124605.

Chaney, K., Swift, R.S., 1986. Studies on aggregate stability. I. Re-formation of soil aggregates. Journal of Soil Science 37(2), 329-335.

Cosentino, D., Chenu, C., Le Bissonnais, Y., 2006. Aggregate stability and microbial community dynamics under drying–wetting cycles in a silt loam soil. Soil Biology and Biochemistry 38(8), 2053-2062.

De Gryze, S., Six, J., Merckx, R., 2006. Quantifying water-stable soil aggregate turnover and its implication for soil organic matter dynamics in a model study. European Journal of Soil Science 57(5), 693-707.

de Tombeur, F., Sohy, V., Chenu, C., Colinet, G., Cornelis, J.-T.J.F.i.E.S., 2018. Effects of Permaculture Practices on Soil Physicochemical Properties and Organic Matter Distribution in Aggregates: A Case Study of the Bec-Hellouin Farm (France). 6, 116.

Denef, K., Six, J., Bossuyt, H., Frey, S.D., Elliott, E.T., Merckx, R., Paustian, K., 2001a. Influence of dry–wet cycles on the interrelationship between aggregate, particulate organic matter, and microbial community dynamics. Soil Biology and Biochemistry 33(12-13), 1599-1611.

Denef, K., Six, J., Paustian, K., Merckx, R., 2001b. Importance of macroaggregate dynamics in controlling soil carbon stabilization: short-term effects of physical disturbance induced by dry–wet cycles. Soil Biology and Biochemistry 33(15), 2145-2153.

Elliott, E., 1986. Aggregate Structure and Carbon, Nitrogen, and Phosphorus in Native and Cultivated Soils 1. Soil science society of America journal 50(3), 627-633.

Gabet, E.J., Dunne, T., 2003. Sediment detachment by rain power. Water Resources Research 39(1), ESG-1.

Gregorich, E.G., Kachanoski, R.G., Voroney, R.P., 1989. Carbon mineralization in soil size fractions after various amounts of aggregate disruption. Journal of Soil Science 40(3), 649-659.

Griffiths, E., Jones, D., 1965. Microbiological aspects of soil structure. Plant and Soil 23(1), 17-33.

Hadas, A., 1990. Directional strength in aggregates as affected by aggregate volume and by a wet/dry cycle. Journal of Soil Science 41(1), 85-93.

Hou, T., Berry, T.D., Singh, S., Hughes, M.N., Tong, Y., Thanos Papanicolaou, A.N., Wacha, K.M., Wilson, C.G., Chaubey, I., Filley, T.R., 2018. Control of tillage disturbance on the chemistry and proportion of raindrop-liberated particles from soil aggregates. Geoderma 330, 19-29.

Jastrow, J.D., 1996. Soil aggregate formation and the accrual of particulate and mineral-associated organic matter. Soil Biology and Biochemistry 28(4), 665-676.

Jiang, Y., Qian, H., Wang, X., Chen, L., Liu, M., Li, H., Sun, B., 2018. Nematodes and microbial community affect the sizes and turnover rates of organic carbon pools in soil aggregates. Soil Biology and Biochemistry 119, 22-31.

Kay, B.D., Groenevelt, P.H., Angers, D.A., Baldock, J.A., 1988. Quantifying the influence of cropping history on soil structure. Canadian Journal of Soil Science 68(2), 359-368.

Kemper, W.D., Rosenau, R.C., 1984. Soil Cohesion as Affected by Time and Water Content1. Soil Science Society of America Journal 48(5), 1001-1006.

Kibblewhite, M.G., Ritz, K., Swift, M.J., 2008. Soil health in agricultural systems. Philosophical Transactions of the Royal Society B: Biological Sciences 363(1492), 685-701.

Kimoto, A., Nearing, M.A., Zhang, X.C., Powell, D.M., 2006. Applicability of rare earth element oxides as a sediment tracer for coarse-textured soils. CATENA 65(3), 214-221.

Le Bissonnais, Y., 1996. Aggregate stability and assessment of soil crustability and erodibility: I. Theory and methodology. European Journal of Soil Science 47(4), 425-437.

Legout, C., Leguedois, S., Le Bissonnais, Y., 2005. Aggregate breakdown dynamics under rainfall compared with aggregate stability measurements. European Journal of Soil Science 56(2), 225-238.

Liang, C., Das, K.C., McClendon, R.W., 2003. The influence of temperature and moisture contents regimes on the aerobic microbial activity of a biosolids composting blend. Bioresource Technology 86(2), 131-137.

Liang, C., Schimel, J.P., Jastrow, J.D., 2017. The importance of anabolism in microbial control over soil carbon storage. Nature Microbiology 2(8), 17105.

Lin, H., 2012. Chapter 2 - Understanding Soil Architecture and Its Functional Manifestation across Scales. In: H. Lin (Ed.), Hydropedology. Academic Press, Boston, pp. 41-74.

Ma, R.-M., Li, Z.-X., Cai, C.-F., Wang, J.-G., 2014. The dynamic response of splash erosion to aggregate mechanical breakdown through rainfall simulation events in Ultisols (subtropical China). Catena 121, 279-287.

Manzoni, S., Schimel, J.P., Porporato, A., 2012. Responses of soil microbial communities to water stress: results from a meta-analysis. Ecology 93(4), 930-938.

Martens, D.A., 2000. Plant residue biochemistry regulates soil carbon cycling and carbon sequestration. Soil Biology and Biochemistry 32(3), 361-369.

Meisina, C., 2006. Characterisation of weathered clayey soils responsible for shallow landslides. Natural Hazards and Earth System Science 6(5), 825-838.

Meisner, A., Bååth, E., Rousk, J., 2013. Microbial growth responses upon rewetting soil dried for four days or one year. Soil Biology and Biochemistry 66, 188-192.

Metherell, A.K., 1993. CENTURY soil organic matter model environment: agroecosystem version 4.0. USDA-ARS.

Mishra, A.K., Dhawan, S., Rao, S.M., 2008. Analysis of swelling and shrinkage behavior of compacted clays. Geotechnical and Geological Engineering 26(3), 289-298.

Morris, E.K., Morris, D., Vogt, S., Gleber, S.-C., Bigalke, M., Wilcke, W., Rillig, M., 2019. Visualizing the dynamics of soil aggregation as affected by arbuscular mycorrhizal fungi. The ISME journal 13(7), 1639-1646.

Navarro-García, F., Casermeiro, M.Á., Schimel, J.P., 2012. When structure means conservation: Effect of aggregate structure in controlling microbial responses to rewetting events. Soil Biology and Biochemistry 44(1), 1-8.

Oades, J., Waters, A., 1991. Aggregate hierarchy in soils. Soil Research 29(6), 815-828.

Oades, J.M., 1984. Soil organic matter and structural stability: mechanisms and implications for management. Plant and Soil 76(1-3), 319-337.

Oades, J.M., 1993. The role of biology in the formation, stabilization and degradation of soil structure. In: L. Brussaard, M.J. Kooistra (Eds.), Soil Structure/Soil Biota Interrelationships. Elsevier, Amsterdam, pp. 377-400.

Papanicolaou, A.N.T., Wacha, K.M., Abban, B.K., Wilson, C.G., Hatfield, J.L., Stanier, C.O., Filley, T.R., 2015. From soilscapes to landscapes: A landscape-oriented approach to simulate soil organic carbon dynamics in intensively managed landscapes. Journal of Geophysical Research: Biogeosciences 120(11), 2375-2401.

Peng, X., Zhu, Q., Zhang, Z., Hallett, P.D., 2017. Combined turnover of carbon and soil aggregates using rare earth oxides and isotopically labelled carbon as tracers. Soil Biology Biochemistry 109, 81-94.

Peng, Z., Smith, C., Stovin, V., 2019. Internal fluctuations in green roof substrate moisture content during storm events: Monitored data and model simulations. Journal of Hydrology 573, 872-884.

Plante, A., Feng, Y., McGill, W., 2002. A modeling approach to quantifying soil macroaggregate dynamics. Canadian Journal of Soil Science 82(2), 181-190.

Plante, A.F., Duke, M.J.M., McGill, W.B., 1999. A tracer sphere detectable by neutron activation for soil aggregation and translocation studies. Soil Science Society of America Journal 63(5), 1284-1290.

Polyakov, V., Nearing, M., Shipitalo, M., 2004. Tracking sediment redistribution in a small watershed: implications for agro-landscape evolution. Earth Surface Processes and Landforms: The Journal of the British Geomorphological Research Group 29(10), 1275-1291.

Rahman, M.T., Liu, S., Guo, Z.C., Zhang, Z.B., Peng, X.H., 2019. Impacts of residue quality and N input on aggregate turnover using the combined 13C natural abundance and rare earth oxides as tracers. Soil and Tillage Research 189, 110-122.

Rajaram, G., Erbach, D.C., 1999. Effect of wetting and drying on soil physical properties. Journal of Terramechanics 36(1), 39-49.

Rovira, A.D., Greacen, E.L., 1957. The effect of aggregate disruption on the activity of microorganisms in the soil. Australian Journal of Agricultural Research 8(6), 659-673.

Salter, P.J., Williams, J.B., 1965. THE INFLUENCE OF TEXTURE ON THE MOISTURE CHARACTERISTICS OF SOILS. Journal of Soil Science 16(2), 310-317.

Schmidt, J., 1992. Modelling long-term soil loss and landform change, Overland Flow. CRC Press, pp. 404-429.

Segoli, M., De Gryze, S., Dou, F., Lee, J., Post, W.M., Denef, K., Six, J., 2013. AggModel: A soil organic matter model with measurable pools for use in incubation studies. Ecological Modelling 263, 1-9.

Sexstone, A.J., Revsbech, N.P., Parkin, T.B., Tiedje, J.M., 1985. Direct measurement of oxygen profiles and denitrification rates in soil aggregates 1. Soil science society of America journal 49(3), 645-651.

Shi, P., Thorlacius, S., Keller, T., Keller, M., Schulin, R., 2017. Soil aggregate breakdown in a field experiment with different rainfall intensities and initial soil water contents. 68(6), 853-863.

Six, J., Bossuyt, H., Degryze, S., Denef, K., 2004. A history of research on the link between (micro) aggregates, soil biota, and soil organic matter dynamics. Soil Tillage Research 79(1), 7-31.

Six, J., Carpentier, A., van Kessel, C., Merckx, R., Harris, D., Horwath, W.R., Lüscher, A., 2001a. Impact of elevated CO_2 on soil organic matter dynamics as related to changes in aggregate turnover and residue quality. Plant and Soil 234(1), 27-36.

Six, J., Elliott, E., Paustian, K., 2000a. Soil macroaggregate turnover and microaggregate formation: a mechanism for C sequestration under no-tillage agriculture. Soil Biology and Biochemistry 32(14), 2099-2103.

Six, J., Elliott, E.T., Paustian, K., 2000b. Soil macroaggregate turnover and microaggregate formation: a mechanism for C sequestration under no-tillage agriculture. Soil Biology and Biochemistry 32(14), 2099-2103.

Six, J., Guggenberger, G., Paustian, K., Haumaier, L., Elliott, E.T., Zech, W., 2001b. Sources and composition of soil organic matter fractions between and within soil aggregates. 52(4), 607-618.

Six, J., Paustian, K., Elliott, E.T., Combrink, C., 2000c. Soil Structure and Organic Matter I. Distribution of Aggregate-Size Classes and Aggregate-Associated Carbon. Soil Science Society of America Journal 64(2), 681-689.

Skidmore, E.L., Layton, J.B., 1992. Dry-Soil Aggregate Stability as Influenced by Selected Soil Properties. 56(2), 557-561.

Sutherland, R.A., Watung, R.L., El-Swaify, S.A., 1996. Splash transport of organic carbon and associated concnetration and mass enrichment ratios for an Oxisol, Hawail. Earth Surface Processes and Landforms 21(12), 1145-1162.

Tang, C.-S., Cui, Y.-J., Shi, B., Tang, A.-M., Liu, C., 2011. Desiccation and cracking behaviour of clay layer from slurry state under wetting–drying cycles. Geoderma 166(1), 111-118.

Tisdall, J.M., Oades, J.M., 1982. Organic matter and water-stable aggregates in soils. Journal of soil science 33(2), 141-163.

Truman, C.C., Bradford, J.M., Ferris, J.E., 1990. Antecedent Water Content and Rainfall Energy Influence on Soil Aggregate Breakdown. 54(5), 1385-1392.

USEPA, 1996. Method 3050B Acid Digestion of Sediments, Sludges, and Soils 1.0 Scope and Application. Washington DC, USA.

Utomo, W.H., Dexter, A.R., 1982. Changes in soil aggregate water stability induced by wetting and drying cycles in non-saturated soil. Journal of Soil Science 33(4), 623-637.

Vaezi, A.R., Ahmadi, M., Cerdà, A., 2017. Contribution of raindrop impact to the change of soil physical properties and water erosion under semi-arid rainfalls. Science of The Total Environment 583, 382-392.

Wacha, K., Papanicolaou, A., Giannopoulos, C., Abban, B., Wilson, C., Zhou, S., Hatfield, J., Filley, T., Hou, T., 2018. The Role of Hydraulic Connectivity and Management on Soil Aggregate Size and Stability in the Clear Creek Watershed, Iowa. Geosciences 8(12), 470.

Wang, X., Yin, L., Dijkstra, F.A., Lu, J., Wang, P., Cheng, W., 2020. Rhizosphere priming is tightly associated with root-driven aggregate turnover. Soil Biology and Biochemistry, 107964.

Wilson, C.G., Abban, B., Keefer, L.L., Wacha, K., Dermisis, D., Giannopoulos, C., Zhou, S., Goodwell, A.E., Woo, D.K., Yan, Q., Ghadiri, M., Stumpf, A., Pitcel, M., Lin, Y.-F., Marini, L., Storsved, B., Goff, K., Vogelgsang, J., Dere, A., Schilling, K.E., Muste, M., Blair, N.E., Rhoads, B., Bettis, A., Pai, H., Kratt, C., Sladek, C., Wing, M., Selker, J., Tyler, S., Lin, H., Kumar, P., Papanicolaou, A.N., 2018. The Intensively Managed Landscape Critical Zone Observatory: A Scientific Testbed for Understanding Critical Zone Processes in Agroecosystems. Vadose Zone Journal 17(1).

Zaher, H., Caron, J., Ouaki, B., 2005. Modeling Aggregate Internal Pressure Evolution following Immersion to Quantify Mechanisms of Structural Stability. Soil Science Society of America Journal 69(1), 1-12.

Zhang, X., Friedrich, J., Nearing, M.A., Norton, L., 2001. Potential use of rare earth oxides as tracers for soil erosion and aggregation studies. Soil Science Society of America Journal 65(5), 1508-1515.

CHAPTER FOUR

RESIDUE COVER EFFECTS ON INTERRILL EROSION AND SIZE SELECTIVITY OF ERODED AGGREGATES IN LOW-GRADIENT FIELDS

Abstract: Residue cover is well known for reducing soil erosion in agricultural lands. However, a better understanding of flow hydraulics and sediment characteristics under various amounts of residue cover would help optimize the use of crop residue for soil conservation. Simulated rainfall experiments (60 mm h^{-1}; 2-hr) on four field plots in Central Illinois were used to evaluate the effects of residue cover on runoff, erosion, particle size distributions, and SOC enrichment ratios in eroded sediments. The experimental conditions included conventional tillage without residue (CT0), no-till with 5% soybean residue (NTS5), no-till with 40% soybean-corn mixture (NTM40), and no-till with 65% corn residue (NTC65). The results affirmed that higher amounts of residue (i.e., NTC65) are best for reducing runoff (i.e., flow depth, flow velocity, stream power, and transport capacity) and soil loss, in this case, by more than two orders of magnitude compared to CT0. NTS5 was least effective in controlling erosion, producing 20% higher runoff and 7% higher soil loss than CT0. NTM40 reduced soil loss by one order of magnitude compared to CT0 but failed to inhibit runoff due to the poor quality of existing soybean residues. The particle size distributions of eroded sediments in all cases consisted of about 97% fine particles (<0.25 mm), evidencing the pronounced size selection of transport by shallow overland flow. The measured ER_{SOC} ranged from 1.3-8.1, which increased as the intensity of soil loss decreased. This study improved the understanding of flow characteristics and sediment transport processes in low-gradient agricultural environments.
Keywords: Runoff hydraulics, Size selectivity, ER_{SOC}, Residue cover, Rainfall simulations, Low-gradient fields

Introduction

Soil quality degradation by water erosion reduces crop yields and threatens food security (Brown, 1981; Pimentel, 2006). In the intensively managed landscapes (IMLs) of the Midwestern US, more than one-third of farmland (~0.4 million km^2) has lost its carbon-rich topsoil due to erosion, resulting in a 6% reduction of corn and soybean yields and losses of $3 billion for farmers every year (Thaler et al., 2021). The soil erosion in IMLs is exacerbated by intensive tillage and residue removal (Papanicolaou et al., 2015). Intensive tillage disrupts soil aggregates and the removal of crop residues exposes weakened soil particles to direct raindrop impacts leading to high soil loss by surface runoff (Elliott, 1986; Wacha et al., 2018).

It has been recognized that reduced tillage and no-till practices, which leave crop residue at the land surface, can effectively curb soil erosion (Bradford and Huang, 1994; Jin et al., 2008; Klik and Rosner, 2020). No-till practices enhance soil aggregation and soil structural development, thereby increasing the soil's resistance to raindrops and runoff (Arshad et al., 1999; Barthes and Roose, 2002; Bronick and Lal, 2005). Meanwhile, crop residue shields surface soils from raindrop detachment (Arsenault and Bonn, 2005; Cogo et al., 1984; Jin et al., 2009), as well as alters the hydraulic properties of overland flow (i.e., flow depth, flow velocity, flow regime, stream power, shear stress, and resistance) and the sediment transport capacity of runoff (Finkner et al., 1989; Guo et al., 2018). A number of studies have served to quantify these benefits; for example, a laboratory experiment by Leys et al. (2010) showed that runoff depth decreased significantly as the residue cover increased from 15% to 45%. Further, Gilley and Kottwitz (1995) measured flow resistance on various crop residues and found that the Darcy-Weisbach friction factor tripled due to the addition of cotton residue. Finally, Shi et al. (2013) conducted rainfall simulation experiments to study residue cover effects on erosion and reported that the stream power decreased by two orders of magnitude and the soil loss decreased by ten times when the residue coverage increased from 15% to 90%. Collectively, these studies provide strong evidence that residue cover can reduce the erosive power of runoff and consequent soil loss. However, these studies were carried out either in laboratory flumes or on steep slopes where concentrated rill flow dominates. To date, little attention has been paid to residue cover effects on runoff and soil erosion processes in low-gradient fields where interrill shallow flow predominates.

Selective transport of small soil particles is more prominent in interrill erosion because the shallow overland flow has insufficient energy to transport large particles (Farenhorst and Bryan, 1995; Govers, 1985; Lu et al., 1988). As such, the particle size distribution of eroded sediments tends to be finer than that of the source soil (Alberts et al., 1980; Liu et al., 2019; Massey and Jackson, 1952a). Additionally, the transported fine particles often contain higher SOC than non-transported large particles due to a large specific surface area (Papanicolaou et al., 2015; Wacha et al., 2020). This observation has been quantified by the enrichment ratio of SOC, ER_{SOC}, which is defined as the ratio of SOC concentration in the eroded sediments to that in the contributing soils (Avnimelech and McHenry, 1984). Considerable studies have investigated the enrichment ratio of SOC in sediments under various rainfall intensity, slope gradient, and soil properties and found that the ER_{SOC} (1.5-5) increased with decreasing intensity of soil erosion (Avnimelech and McHenry, 1984; Ghadiri and Rose, 1991; Hu et al., 2013; Nie et al., 2015; Schiettecatte et al., 2008). Though these studies provide valuable information on ER_{SOC} and soil erosion, little is known about ER_{SOC} in the low-gradient environment under different tillage and residue cover treatments.

The purpose of this study is to investigate the effects of tillage and residue cover on runoff erosion processes and size-selective transport of soil aggregates in a low-gradient agricultural system. Simulated rainfall experiments were carried out in four field plots in Central Illinois, which present different tillage and residue coverage levels. The specific objectives are to (1) compare the general hydraulic characteristics of runoff, transport capacity, and total soil loss of various aggregate size fractions between the four treatments and (2) examine the temporal variations of runoff discharge, sediment concentration, the particle size distributions of eroded sediments, and ERSOC under the different treatments. By addressing these objectives, this study provides important insights into understanding flow characteristics and selective transport of soil aggregates in residue cover affected low-gradient environments.

Materials and Methods

Experimental Plots

The simulated rainfall experiments for this study were conducted on four agricultural plots located in the Upper Sangamon River Basin, Central Illinois. The four experimental plots differed substantially in tillage states at present and the proportions of surface area covered by crop residues (Figure 4-1), including conventional tillage without residue (CT0), no-till with 5% soybean [*Glycine max*] residue (NTS5), no-till with 40% soybean-corn residue mixture (NTM40), and no-till with 65% corn [*Zea mays*] residue (NTC65). The areal percentages of the plot surface covered by residue were estimated by segmenting the residues from field images using the ImageJ software (Figure C-4). The four plots were uniform in terms of downslope curvature and had similar slope gradients (0.05-2.44%), soil type (silty clay loam), and soil properties (Table 4-1), which allow for examining the effects of different tillage practices and residue cover on runoff characteristics and soil loss under simulated rainfall.

Plot CT0, in Goose Creek (40° 8'55.89"N, 88°35'27.93"W), was disked one week before the rainfall simulation so it was clear of residue. Plot NTS5 was near Wildcat Slough (40°22'27.40"N, 88°11'37.90"W) and was sparsely covered by a small number of soybean stubbles (5%). Though this field was tilled in the previous fall, the present soil surface was hard and relatively smooth at the time of the rainfall simulation experiment, which is likely due to soil consolidation during the winter and early spring (Eltner et al., 2015). Therefore, this plot was considered as analogous as no-till in this study. Plot NTM40 was on the hilltop of Wildcat (40°22'30.10"N, 88°11'36.50"W) with high portions of soybean stubbles mixed with a small amount of highly decomposed corn stalks (40%). Plot NTC65 was situated at the farmland in Saybrook (40°26'39.49"N, 88°28'48.61"W) and was managed as no-till with even year soybean and odd year corn rotations. During the rain simulation, the plot surface was covered by a dense portion of corn stalks, leaves, and bare corn cobs (65%).

Rainfall Simulation and Sample Collection

Runoff and soil loss were monitored from the four plots during experiments conducted in mid-April 2016 (Figure 4-1) following the procedure described in Wacha et al. (2020). Each rainfall test was run for 120 min with constant 60 mm h^{-1} intensity to ensure both runoff and sediment fluxes reached steady-state conditions (Wacha et al., 2020). Rainfall was applied to each plot using Norton ladder rainfall simulators designed by the USDA-ARS National Erosion Research Laboratory. Figure 4-1a shows the setup for all experimental runs conducted for this study. For each test, three rainfall simulators were mounted in series over the experimental plot covering an effective rainfall area of 7 m

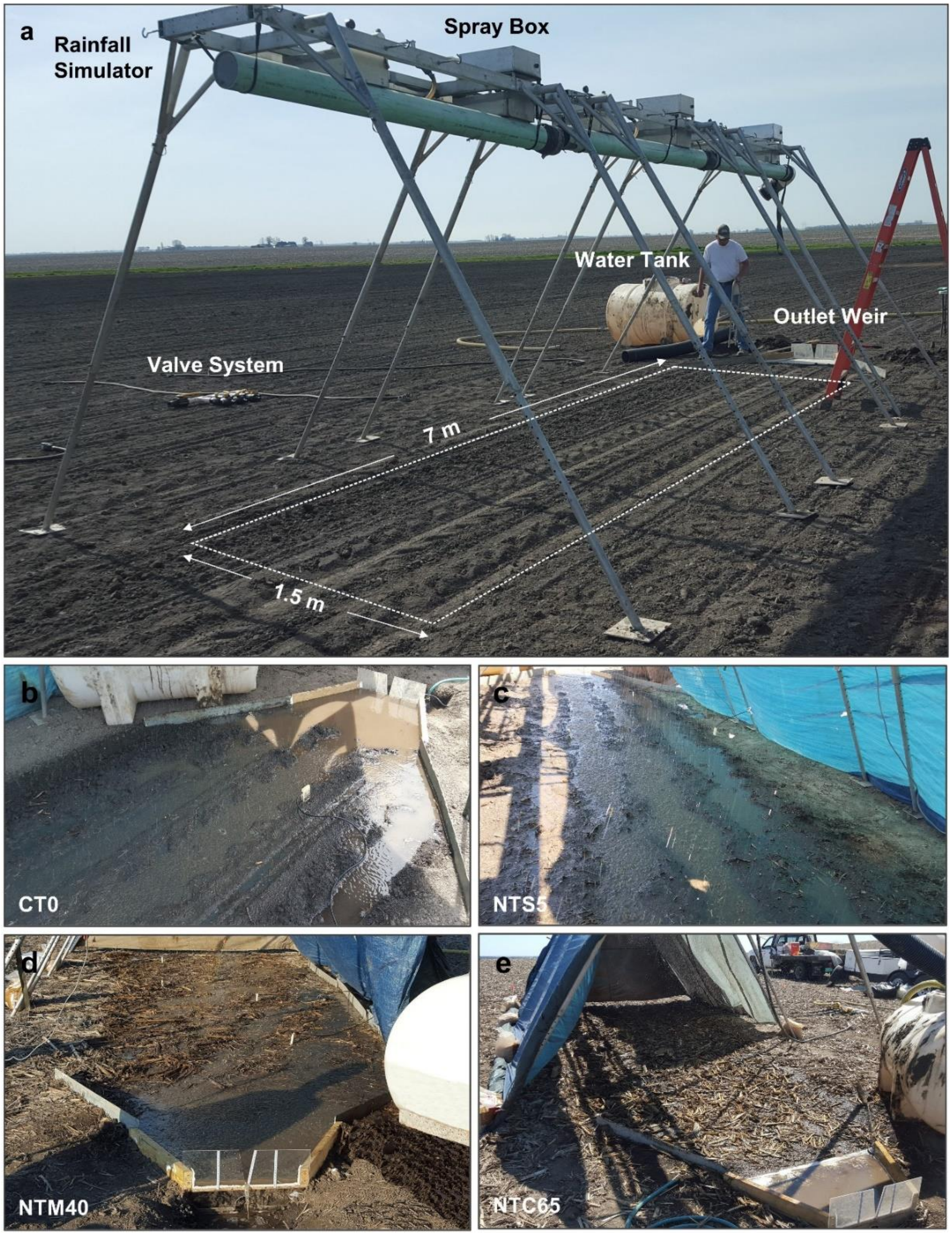

Figure 4-1. (a) Overview of the experimental setup in the field and images of the rainfall plots under different tillage practices and residue cover: (b) conventional till without residue (CT0); (c) no-till with 5% soybean residue (NTS5); (d) no-till with 40% soybean and corn mixture (NTM40); and (e) no-till with 65% corn residue (NTB65).

Table 4-1. Experimental conditions of the field rainfall simulations.

Plot code	Current state of tillage	Residue type	Residue Cover (%)	Slope gradient (%)	Bulk density (g cm^{-3})	SOC (%)	Soil texture (%)		
							Sand	Silt	Clay
CT0	Conventional till	None	0	0.50	1.00	2.79	5	71	24
NTS5	No-till	Soybean	5	1.25	1.29	2.64	18	58	24
NTM40	No-till	Soybean-corn	40	2.00	1.16	2.24	15	58	27
NTC65	No-till	Corn	65	2.44	1.34	1.94	21	56	23

long by 1.5 m wide. Six oscillating VeeJet nozzles were suspended approximately 2.5 m above the plot surface to ensure that the terminal velocity of natural rainfall was reached. Water was continuously pumped from a water tank with constant pressure to the nozzles, which provided uniform spherical raindrops in a median diameter of 2.5 mm and a terminal velocity of 7.25 m s^{-1}. A 20° V-notch weir was installed at the downslope end of the plot for runoff monitoring and water-sediment sample collection. The windward sides of the rainfall simulators were tarped to minimize wind disturbances to rainfall. Flow depths at the weir outlet were recorded every five minutes, followed by immediately collecting runoff samples using 1000-mL wide-mouth plastic bottles. The samples were stored in coolers and transported overnight to the laboratory in Knoxville, TN, for analysis.

Sample Analyses

The runoff samples were weighed and gently shaken to resuspend the settled sediments without disrupting aggregates. The water-sediment mixture was passed through a stack of 2-mm and 0.25-mm sieves to separate the sediments into three size fractions: large macroaggregates (>2mm), small macroaggregates (0.25-2 mm), and fines (<0.25 mm). The fractionated particles were stored in separate cups and oven-died at 60°C for 24 h. The dry weight of each size fraction was measured to calculate the sediment concentration of each particle size. The three aggregate fractions were ultimately recombined and the total SOC concentrations were measured with the Sercon Ltd. (Crewe, UK) flash combustion elemental analyzer described in Hou et al. (2018).

Calculations

<u>Rain Power</u>

Soil detachment by raindrop impact is the first step of soil erosion (Bielders and Grymonprez, 2010). When a raindrop strikes soil, the raindrop kinetic energy is transferred to soil particles and water on the surface, detaching soil particles and displacing water. However, on a residue-covered surface, the raindrops can be intercepted by residues and thus have essentially zero velocity reaching the soil surface leading to no capacity to detach soil (Gabet and Dunne, 2003). Therefore, the rain power (R, W m^{-2}) was determined for each experimental run to describe the amount of effective energy transferred to the soil particles affected by different residue coverages (Gabet and Dunne, 2003):

$$R = \frac{\rho I v^2 (1 - C_r) \cos\theta}{2} \tag{4-1}$$

where ρ is water density (assumed to be a constant value of 1000 kg m^{-3} at 10 ℃), I is the rainfall intensity (1.6×10^{-5} m s^{-1}), v is the terminal velocity of raindrops (7.25 m s^{-1}), C_r is the proportion of the plot surface covered by crop residue, θ is the plot slope (degrees).

Runoff Hydraulic Parameters

The transport of soil particles by rain-induced runoff is the second step of soil erosion, which is strongly influenced by the hydraulics characteristics of overland flow (Abrahams and Parsons, 1994; Emmett, 1970). To evaluate the effects of residue cover on soil erosion, runoff discharge, flow depth, stream power, hydraulic shear stress, flow velocity, Reynolds number, Froude number, the Darcy-Weisbach friction, and the Manning's roughness were studied according to previous studies (Guo et al., 2018; Shi et al., 2013).

The runoff discharge (Q, m^3 s^{-1}) was calculated using the following equation for V-notch weir (Sturm, 2001):

$$Q = 1.55 \times \tan(\frac{\theta_w}{2})\, H_w^{2.5} \tag{4-2}$$

where H_w is the flow height above the bottom of the notch (m) and θ_w is the notch angle (20°).

The average flow depth (h, m) was calculated as follows:

$$h = \frac{(Q_{t+1} - Q_t)t}{A} \tag{4-3}$$

where Q_{t+1} is the runoff discharge at time $t + 1$, Q_t is the runoff discharge at time t, t is the time interval (s), and A is the plot area (10.5 m^2).

The stream power (ω, W m^{-2}) and hydraulic shear stress (τ, Pa) were calculated as (Govers, 1990):

$$\omega = \frac{\gamma S Q}{W} \tag{4-4}$$

$$\tau = \gamma h S \tag{4-5}$$

where γ is the specific weight of water (kg m^{-2} s^{-2}) and calculated as $\gamma = \rho g$, where ρ is water density (kg m^{-3}), g is the gravitational acceleration (9.81 m s^{-2}), S is the slope gradient, h is the average flow depth (m), and W is the plot width (1.5 m).

The average flow velocity (V, m s^{-1}) can be determined as:

$$V = \frac{\omega}{\tau} \tag{4-6}$$

The Reynolds number (Re) and Froude number (Fr) were calculated to reflect the flow regime (Abrahams et al., 1986):

$$Re = \frac{Vh}{v} \tag{4-7}$$

$$Fr = \frac{V}{\sqrt{gh}} \tag{4-8}$$

where V is the average flow velocity (m s^{-1}), h is the average flow depth (m), v is the kinematic viscosity(assumed to be a constant value of $1.3 \times 10^{-6}\ m^2 s^{-1}$ at 10 ℃).

The Darcy-Weisbach friction factor (f) and Manning's roughness coefficient (n, m$^{-1/3}$ s) were calculated to determine flow resistance:

$$f = \frac{8ghS}{V^2} \tag{4-9}$$

$$n = \frac{h^{\frac{2}{3}}\sqrt{S}}{V} \tag{4-10}$$

where g is the gravitational acceleration (m s^{-2}), S is the slope gradient, h is the average flow depth (m), and V is the average flow velocity (m s^{-1}).

<u>Sediment Transport Capacity</u>

To evaluate whether a soil particle will move or settle under certain runoff, the sediment transport capacity (T_c, g m^{-1} s^{-1}) of the shallow overland flow was estimated for each aggregate size fraction using the Yalin equation (Papanicolaou et al., 2015):

$$\frac{T_c}{(SG_i)d_i\rho_w^{0.5}\tau^{0.5}} = 0.635\delta[1 - \frac{1}{\beta}\ln(1+\beta)] \tag{4-11}$$

$$\beta = 2.45(SG_i)^{-0.4}(\tau_c^*)^{0.5}\delta \tag{4-12}$$

$$\delta = \frac{\tau^*}{\tau_c^*} - 1\ (when\ \tau^* < \tau_c^*, \delta = 0) \tag{4-13}$$

$$\tau^* = \frac{\tau}{\rho_w(SG_i - 1)gd_i} \tag{4-14}$$

where SG_i is the particle specific gravity of size fraction i (i denotes >2 mm, 0.25-2 mm, and <0.25 mm fractions), d_i is the medium particle diameter of size fraction i (m) and approximated using the empirical equations described in Papanicolaou et al. (2015), ρ_w is water density (g m^{-3}), τ is the hydraulic shear stress (Pa), τ_c^* is the dimensionless critical shear stress from Shields Diagram, $\tau^*$is the dimensionless hydraulic shear stress, β and δ are dimensionless parameters reflecting soil properties.

<u>Enrichment Ratio of SOC</u>

For determining SOC loss by erosion, the SOC enrichment in sediment compared to source area soil, expressed as the enrichment ratio (ER_{SOC}), was calculated using the following formula (Massey and Jackson, 1952b):

$$ER_{SOC} = \frac{SOC_{sediment}}{SOC_{source}} \tag{4-15}$$

where $SOC_{sediment}$ is the SOC concentration (%) in the sediments collected at the weir outlet and SOC_{source} is the SOC concentration (%) in the plot source soils. ER_{SOC} > 1 indicates SOC accumulation in the eroded sediments and ER_{SOC} < 1 indicates SOC depletion in the eroded sediments.

Results

General Characteristics of Rain Power, Runoff, and Soil Loss

The residue cover presence influenced rain power, general runoff hydraulics, and soil loss, as shown in Table 4-2. The rain power consistently decreased with increasing residue cover. The residue cover of 5, 40, and 65% reduced the rain power by 5, 50, and 66%, respectively, compared to the bare soil case. Conversely, the runoff responded differently to the various surface conditions. The runoff coefficients (defined as the percentage of rainfall converted into overland flow during an event) were relatively high, ranging from 0.5 to 0.7 in the bare soil (CT0) and low-medium residue cover (NTS5 and NTM40) plots. For the high residue cover plot (NTC65), the runoff coefficient was two orders of magnitudes (0.01) lower than other plots. Likewise, the average flow depth (h) was highest under NTM40 (5.27 mm), medium under CT0 and NTS5 (3.28 mm), and lowest under NTC65 (0.14 mm). The average flow velocity (h) was higher under CT0, NTS5, and NTM40 (0.023 ± 0.001 m s^{-1}) than under NTC65 (0.013 m s^{-1}). Correspondingly, the Reynolds number (Re) was highest under NTM40 (94), medium under CT0 and NTS5 (57 ± 4), and lowest under CT65 (1.3). The Froude numbers (Fr) were generally low in all cases, varying from 0.10 to 0.39.

The stream power (ω) was generally low, with a highest observed value of 0.0241 W m^{-2} for NTM40 and the lowest value of 0.0004 W m^{-2} for NTC65 (Table 4-2). Similarly, the hydraulic shear stress (τ) varied from 0.034 to 1.035 Pa with the highest value for NTM40 and lowest value for NTC65. The Darcy-Weisbach friction (f) and the Manning's roughness (n) showed increasing trends with increasing residue cover except for the NTC65 case, which had the smallest f and n values. The estimated sediment transport capacity by flow from the CT0 plot ranged from 0.02 to 3 g m^{-1} s^{-1} with the highest transport rate observed for the smallest particles. The transport capacity of flow from the NTS5 plot was six times higher compared to CT0, which had the highest value of 12.26 g m^{-1} s^{-1} for fines particles (< 0.25 mm) and the lowest value of 2.83 g m^{-1} s^{-1} for small macroaggregates (0.25-2 mm). The runoff from the NTM40 plot possessed the highest transport capacity on all size fractions, which had the highest value of 63.2 g m^{-1} s^{-1} for large macroaggregates and the lowest value of 45.39 g m^{-1} s^{-1} for small macroaggregates. In contrast, the NTC65 flow only can transport fine particles with a small capacity of 0.03 g m^{-1} s^{-1}. Consequently, the cumulative soil loss from each plot was in the rank of NTS5 (2281 g) > CT0 (2131 g) > NTM40 (843 g) > NTC65 (16 g), in which fine particles accounted for 97% of the total lost soil.

Table 4-2. Rainfall simulation results of rain power, hydraulic parameters of overland flow, sediment transport capacity, and the cumulative loss of each aggregate size fractions for the experimental plots.

Plot code	R (W m^{-2})	RC	h (mm)	V (m s^{-1})	ω (W m^{-2})	τ (Pa)	Re	Fr	f	n ($m^{-1/3}$ s)	T_c (g m^{-1} s^{-1})			CSL (g)		
											>2 mm	0.25-2 mm	<0.25 mm	>2 mm	0.25-2 mm	<0.25 mm
CT0	0.44	0.5	3.27	0.024	0.0038	0.160	59	0.14	2.34	0.66	0.02	0.20	3.00	54	31	2045
NTS5	0.42	0.6	3.28	0.022	0.0086	0.399	54	0.13	5.63	1.18	6.32	2.83	12.26	47	15	2219
NTM40	0.22	0.7	5.27	0.023	0.0241	1.035	94	0.10	15.2	1.84	63.2	45.39	51.97	0.3	5.2	823
NTC65	0.15	0.01	0.14	0.013	0.0004	0.034	1.3	0.39	1.99	0.35	0.00	0.00	0.03	0.2	0.2	15.5

Note: R, rain power; RC, runoff coefficient; h, average flow depth; V, average flow velocity; ω, stream power; τ hydraulic shear stress; Re, Reynolds number; Fr, Froude number; f, Darcy-Weisbach friction factor; n, Manning's roughness coefficient; T_c, sediment transport capacity; CSL, cumulative soil loss.

Temporal Variation of Runoff Discharge and Sediment Concentration

Figure 4-2 illustrates the temporal variations in runoff discharge and sediment concentration under various tillage and residue cover treatments. The tilled plot with bare soil (CT0) and the no-till plots with low-medium residue cover (NTS5 and NTM40) exhibited similar runoff processes and patterns with three distinct stages: the period from the start of rainfall to runoff initiation, the period from runoff initiation to peak runoff, and the period of steady-state (Figure 4-2a). For CT0, the runoff increased fast during the 11 to 63 min of rainfall before slowly approaching the steady state. The runoff discharge under NTM40 increased faster than CT0 during the 12 to 58 min of rainfall followed by the steady-state of 148 ± 7 cm^3 s^{-1}. The runoff discharge regarding NTS5 increased rapidly during the 13 to 47 min of rainfall with a subsequent steady state of 85 ± 8 cm^3 s^{-1}. For the no-till plot with high residue cover (NTC65), the runoff discharge was consistently low throughout the rainfall simulation (2.1 ± 0.6 cm^3 s^{-1}).

The sediment concentration patterns varied based on tillage practices and residue cover (Figure 4-2b). The tilled plot with bare soil (CT0) and the no-till plot with 5% residue cover (NTS5) produced high sediment concentrations during the first few minutes of runoff and then decreased to a constant level 3.5 g L^{-1}. In contrast, the no-till plots with 40% (NTM40) and 65% (NTC65) residue cover led to consistently low sediment concentrations during the entire rainfall simulation (1.3 ± 0.5g L^{-1}).

Temporal Variation of Particle Size Distribution and ER_{SOC}

Figure 4-3 shows the temporal variations in eroded sediment particle size (expressed as a relative proportion) under the four treatments. The fine particles (< 0.25 mm) comprised the highest proportion of sediments varying between 92 and 99% throughout all rainfall simulations, regardless of different treatments. The percentages of small (0.25-2 mm) and large (> 2 mm) macroaggregates in all cases were less than 10% during the rainfall and exhibited smaller temporal variations under CT0 than under other treatments.

The ER_{SOC} in sediments differed greatly between the different treatments during the simulated rainfall (Figure 4-4). Under both CT0 and NTS5, the ER_{SOC} in sediments exhibited similar values and patterns varying slightly around the mean of 1.6. The maximum ER_{SOC} values in CT0 and NTS5 sediments were 2.2 and 1.9, respectively, and occurred at 102 min of the rainfall. The ER_{SOC} in NTM40 sediments initially decreased and then increased to a steady-state (2.7-3.4) followed by a sudden decrease around 75 min and a return to steady-state. Under NTM40, the minimum ER_{SOC} was 2.0 occurring at 19 min of the rainfall and the maximum ER_{SOC} was 4.0 occurring at the end of rainfall. For NTC65, the ER_{SOC} in sediments varied largely during the simulated rainfall, which initially decreased rapidly from the maximum value of 8.1 to the minimum value of 3.3 and then increased gradually and leveled off around 6.5. Overall, the mean ER_{SOC} in all sediments followed this order of statistical significance ($p < 0.0001$): CT0 = NTS5 (1.6 ± 0.2) < NTM40 (3.0 ± 0.5) < NTC65 (5.6 ±1.7) (Figure 4-4).

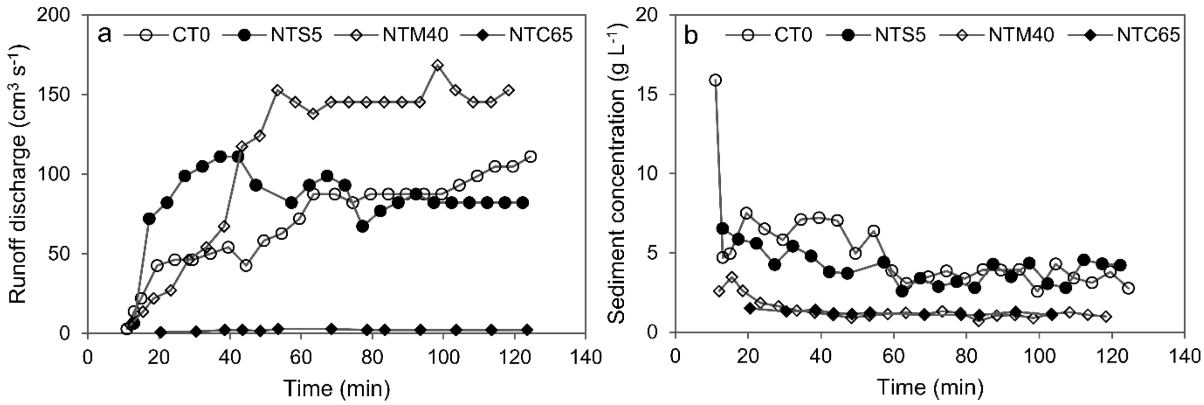

Figure 4-2. Temporal changes of (a) runoff discharge and (b) sediment concentration under different tillage practices and residue cover. The meaning of the different plot codes is given in Table 4-1.

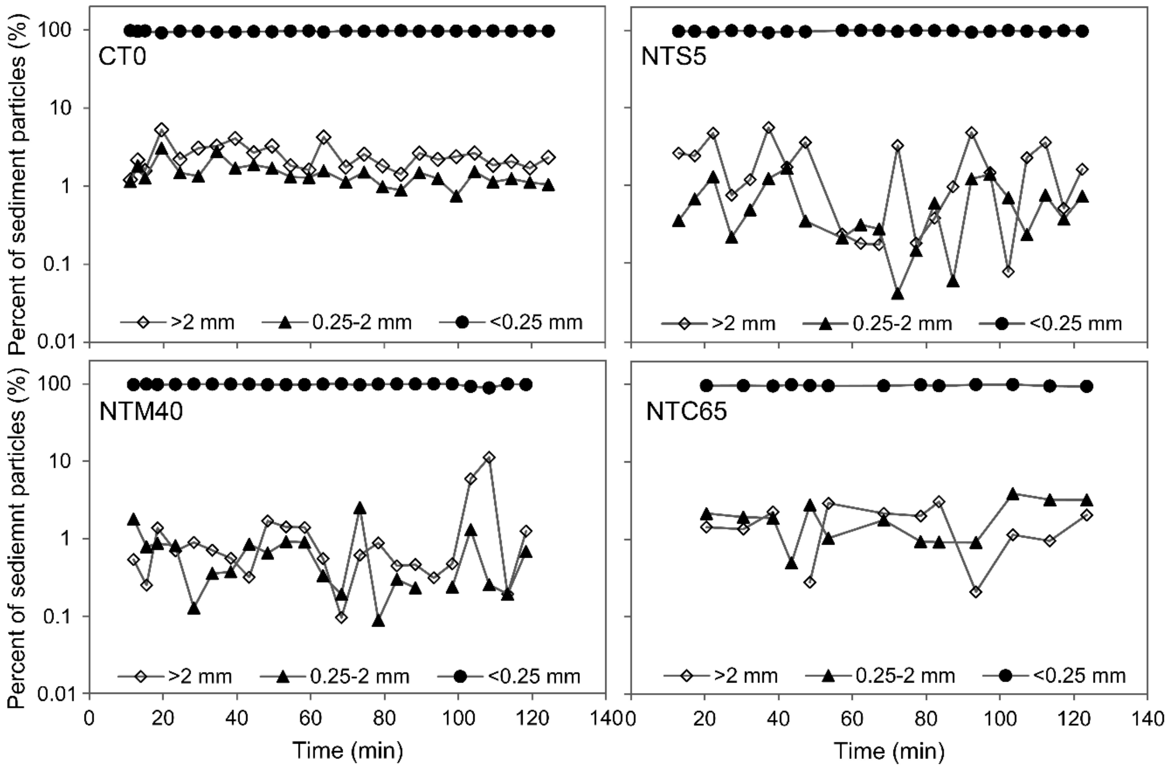

Figure 4-3. Temporal changes of the percentage of eroded sediment particles under different tillage practices and residue cover (note: a based-10 log scale is used for the y-axes).

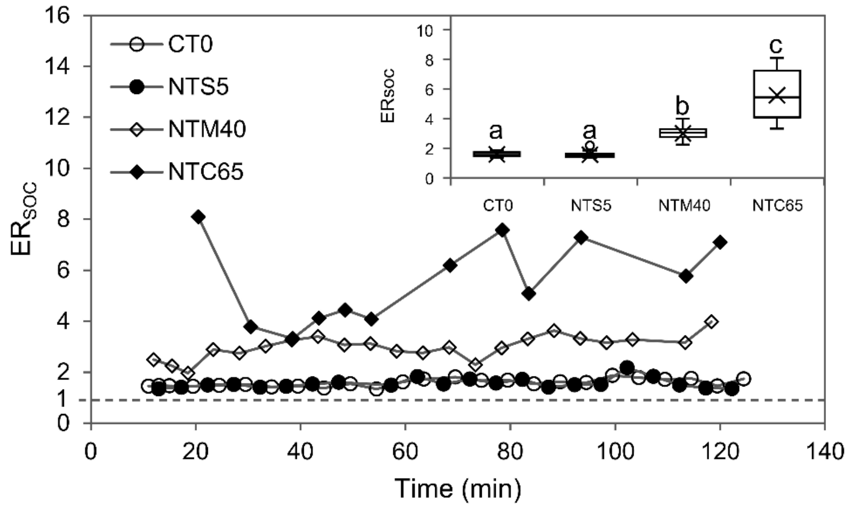

Figure 4-4. Temporal changes of the enrichment ratio of SOC (ER$_{SOC}$) under different tillage practices and residue cover. The boxplot in the upper right corner shows the mean ('x' mark) and range of ER$_{SOC}$ values for different tillage practices and residue cover. Different letters represent significant differences in mean values between the treatments ($P < 0.05$).

Relationship between Flow Resistance, Sediment Concentration, and ER_{SOC}

The relation between instantaneous Darcy-Weisbach friction factor and total sediment concentration was explored to identify the dominant erosive processes involved (Figure 4-5a). Under the bare (CT0) and low-medium (NTS5 and NTM40) residue cover, a negative correlation existed between the Darcy-Weisbach friction and sediment concentration. For the high residue cover case (NTC65), the relationship between the Darcy-Weisbach friction and sediment concentration was not clear as the sediment concentration was steadily low. The relationship between the sediment concentration and ER_{SOC} was also examined to identify the selective SOC enrichment process in the eroded sediments (Figure 4-5b). Generally, the ER_{SOC} decreased as the sediment concentration increased, but the trend was variable between treatments. As residue cover increased, a milder drop in ER_{SOC} was noted.

Discussion

Effects of Residue Cover on Rain Power and Runoff Hydraulics

Erosion control effectiveness depends on the surface conditions induced by particular management practices such as residue cover (Wischmeier, 1973). Consistent with previous studies (Guo et al., 2018; Jin et al., 2009; Laflen and Colvin, 1981), our results showed that the total soil loss decreased significantly with increasing residue cover. Residue cover reduces soil erosion in two ways. The first is by reducing the direct impact of raindrops on the soil surface in proportion to the percentage of the surface covered by residue (Cogo et al., 1984). This can be observed herein as the decreasing rain power seen with increasing residue coverage during the four rainfall simulations. According to the rainfall simulation experiments by Gabet and Dunne (2003), the decreased rain power by residue cover can significantly reduce soil detachment rates as the raindrop kinetic energy imposed on soil particles is attenuated.

Second, the residue on the surface influences the hydraulic characteristics of overland flow, which dictates the sediment transport capacity of runoff. Our results showed that the Reynolds numbers were <100 (1.3-94) and Froude numbers were <1 (0.10-0.39) for all experimental runs, indicating the laminar and subcritical flow regimes (Lawrence, 1997). Parsons et al. (1994) also reported a low range of Reynolds number (0.43-4.8) for flow through a rough surface (i.e., grassland). The Darcy-Weisbach friction factor varied from 1.99 to 15.2, which fell in the range commonly reported in the literature of 0.1 to 20 for residue- or vegetation-covered surface (Abrahams et al., 1986; Gilley and Kottwitz, 1995; Lawrence, 1997). Interestingly, the stream power, shear stress, and transport capacity in NTS5 and NTM40 were higher compared to CT0 regardless of their higher percentage of residue cover. This is probably because of the existing small and highly decomposed soybean residues in the NTS5 and NTM40 plots, which created less roughness than the tillage-induced roughness in the CT0 plot. This finding demonstrated that the efficacy of residue on reducing erosive runoff power is influenced not only by the

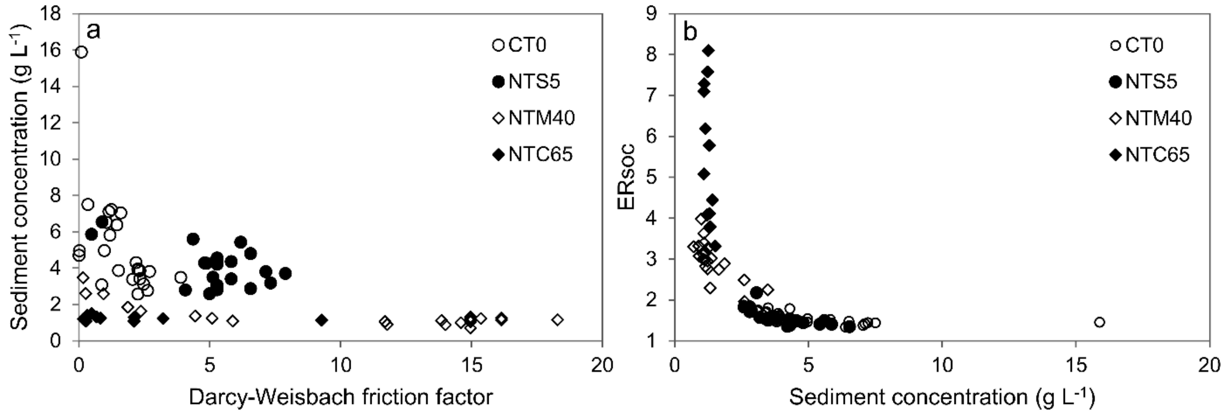

Figure 4-5. (a) Darcy-Weisbach friction factor versus sediment concentration and (b) sediment concentration versus the enrichment ratio of SOC (ER_{SOC}) for different tillage practices and residue cover.

surface cover proportions but also by the size and quality of residue.

Effects of Tillage and Residue on Runoff Generation and Sediment Transport

For the no-till plot covered by highly decomposed soybean-corn residues (NTM40), the runoff discharge remained high because surface soil pores were shielded and rainfall infiltration was low (Freebairn and Gupta, 1990). The soybean residues can be easily moved by runoff due to their small size and lightweight, thus failing to reduce runoff velocity and power (Cogo et al., 1984). However, the total soil loss from NTM40 was two times lower than from those with little or no residue (NTS5 and CT0), owing to the reduced soil detachment rates and few loose particles available for transport (Bradford and Huang, 1994). For the no-till plot with high corn residue (NTC65), the runoff discharge was two orders of magnitude lower than that of NTM40, which is due to rainfall interception by corn residues (i.e., bare corn cobs, stalks, and leaves) and runoff ponding behind large residue pieces (Bradford and Huang, 1994). The soil loss from NTC65 dropped by one order of magnitude because low detached particles available for transport, low stream power to transport and deposition of sediments in the residue pieces created small reservoirs. This result demonstrated that corn residue is more effective in reducing both runoff and soil loss than soybean residue, as also suggested by other researchers (Cogo et al., 1984; Ketcheson and Stonehouse, 1983); thus, the type of residue cover appears to be of importance along with the percent residue cover.

Under little (NTS5) and no (CT0) residue covered cases, the runoff discharge from NTS5 was twice higher than that from CT0 during the first 40 min of rainfall, which is due to lower infiltration rates in the compacted surface and clogging of pores by raindrop splash (A. Fattah and K. Upadhyaya, 1996; Zhang et al., 2019). The runoff discharge was lower under CT0 because of greater tillage-induced surface roughness and water storage in the rut depressions (M. Mohamoud et al., 1990). The raised rainfall infiltration rates through the loose soil column could also cause the observed lower runoff discharge at the early stage (Arshad et al., 1999; Carretta et al., 2021). The steady-state runoff discharge was about the same under NTS5 and CT0 because surface sealing is primarily responsible for infiltration and runoff rates at the late stage of simulated rainfall (Bradford and Huang, 1994). Theoretically, the NTS5 no-tilled soil should have higher aggregate stability than the CT0 tilled soil. However, this superiority of NTS5 seems offset by its higher early-stage runoff rates, resulting in slightly higher sediment concentration and total soil loss than CT0. These findings revealed that removing crop residues from the no-till system could result in as high as or higher soil loss than those obtained with conventional tillage practices since the smooth soil surface with inadequate residue cover will seal and crust, enhancing runoff generation and soil transport (Bradford and Huang, 1994).

Effects of Residue Cover on Size Selectivity of Transport

The particle size distributions of the eroded sediments from the four plots were dominated by fine particles (>95%), indicating that the transport processes are highly size-selective regardless of surface conditions. This is likely due to the generally low slope gradients of the four plots (0.5-2.44%; Table 4-1), which generally produce low stream power (0.0002-0.0181 W m^{-2}; Table 4-2) that can only mobilize microaggregates and silt/clay-sized particles. The ER_{SOC} was in the range of 1.3-8.1, which is consistent with the reported range of 0.74-6.2 in literature (Martínez-Mena et al., 2002; Papanicolaou et al., 2015; Schiettecatte et al., 2008). The negative relationship between ER_{SOC} and sediment flux (Figure 4-5b) was also reported by previous research (Ghadiri and Rose, 1991; Hu et al., 2013; Jin et al., 2009; Schiettecatte et al., 2008). Massey and Jackson (1952b) pointed that the erosive processes are more selective for SOC (namely high ER_{SOC}) when the amount of soil material eroded is low, which is the case of NTC65 where only small amounts of SOC-enriched fine particles (0.03 g m^{-1} s^{-1}) were mobilized (Table 4-2). Additionally, the observed large temporal variation of ER_{SOC} under the low soil loss case of NTC65 was also reported by Cogle et al. (2002), indicating high uncertainty of sediment delivery under residue-induced low runoff events.

Conclusions

This study investigated the rain power, runoff hydraulic characteristics, and size-selective transport of soil aggregates using simulated rainfall on four low-gradient plots with variable levels of tillage and residue cover, including conventional tillage without residue (CT0), no-till containing 5% soybean residue (NTS5), no-till containing 40% soybean-corn mixture (NTM40), and no-till containing 65% corn residue (NTC65). As expected, the estimated rain power decreased with increasing residue cover percentage, and the overland flow from all plots was in the laminar and subcritical regimes. The high percent of large corn residues in the NTC65 plot produced flow with the lowest flow depth, flow velocity, stream power, and transport capacity, resulting in the lowest soil loss and highest ER_{SOC}. The NTS5 plot exhibited similar flow hydraulic characteristics and soil loss as the CT0 plot, indicating that removing residue cover from the no-till system could result in substantial soil erosion due to increased runoff from crusting and sealing. About 97% of the eroded sediments were fine particles (0.25 mm), suggesting the pronounced transport selectivity of the shallow interrill flow. The measured ER_{SOC} values increased as the intensity of soil erosion decreased, which can be attributed to residue cover. Overall, this study systematically investigated the flow characteristics and selective transport of soil aggregates under various levels of tillage and residue cover. Insights were gained which improved the understanding of aggregate transport processes in low-gradient environments, an understudied contest, and provided important insights into improving agricultural management to control erosion and maintain soil health. The simulated rainfall is limited to the plot scale, which cannot fully capture aggregate and SOC transport processes on a larger scale. Future studies should explore the aggregate transport distance and SOC redistribution processes at the field scale under natural rainfall conditions.

Acknowledgments

This research was supported by the National Science Foundation [grant number EAR1331906] for the IML-CZO program, a multi-institutional collaborative effort. We would like to thank Dr. Achilleas Tsakiris and Christos Giannopoulos for conducting the field rainfall experiments and laboratory sediment analyses. The first author was part of the China-UT EcoPartnership Scholars Program and is grateful for the support from the China Scholarship Council.

References

A. Fattah, H., K. Upadhyaya, S., 1996. Effect of Soil Crust and Soil Compaction on Infiltration in a Yolo Loam Soil. Transactions of the ASAE 39(1), 79-84.

Abrahams, A., Parsons, A., Luk, S.-H., 1986. Resistance to overland flow on desert hillslopes. Journal of Hydrology 88(3-4), 343-363.

Abrahams, A.D., Parsons, A.J., 1994. Hydraulics of interrill overland flow on stone-covered desert surfaces. Catena 23(1-2), 111-140.

Alberts, E.E., Moldenhauer, W.C., Foster, G., 1980. Soil Aggregates and Primary Particles Transported in Rill and Interrill Flow 1. Soil Science Society of America Journal 44(3), 590-595.

Arsenault, É., Bonn, F., 2005. Evaluation of soil erosion protective cover by crop residues using vegetation indices and spectral mixture analysis of multispectral and hyperspectral data. Catena 62(2-3), 157-172.

Arshad, M.A., Franzluebbers, A.J., Azooz, R.H., 1999. Components of surface soil structure under conventional and no-tillage in northwestern Canada. Soil and Tillage Research 53(1), 41-47.

Avnimelech, Y., McHenry, J.R., 1984. Enrichment of Transported Sediments with Organic Carbon, Nutrients, and Clay. Soil Science Society of America Journal 48(2), 259-266.

Barthes, B., Roose, E., 2002. Aggregate stability as an indicator of soil susceptibility to runoff and erosion; validation at several levels. Catena 47(2), 133-149.

Bielders, C.L., Grymonprez, B., 2010. Raindrop Impact: A Neglected but Potentially Major Contributor to Particle Mobilization in Soils. 74(5), 1446-1456.

Bradford, J.M., Huang, C.-h., 1994. Interrill soil erosion as affected by tillage and residue cover. Soil tillage Research 31(4), 353-361.

Bronick, C.J., Lal, R., 2005. Soil structure and management: a review. Geoderma 124(1), 3-22.

Brown, L.R., 1981. World population growth, soil erosion, and food security. Science, 995-1002.

Carretta, L., Tarolli, P., Cardinali, A., Nasta, P., Romano, N., Masin, R., 2021. Evaluation of runoff and soil erosion under conventional tillage and no-till management: A case study in northeast Italy. CATENA 197, 104972.

Cogle, A., Rao, K., Yule, D., Smith, G., George, P., Srinivasan, S., Jangawad, L.J.S.U., Management, 2002. Soil management for Alfisols in the semiarid tropics: erosion, enrichment ratios and runoff. 18(1), 10-17.

Cogo, N., Moldenhauer, W., Foster, G., 1984. Soil loss reductions from conservation tillage practices. Soil Science Society of America Journal 48(2), 368-373.

Elliott, E., 1986. Aggregate Structure and Carbon, Nitrogen, and Phosphorus in Native and Cultivated Soils 1. Soil science society of America journal 50(3), 627-633.

Eltner, A., Baumgart, P., Maas, H.-G., Faust, D., 2015. Multi-temporal UAV data for automatic measurement of rill and interrill erosion on loess soil. Earth Surface Processes and Landforms 40(6), 741-755.

Emmett, W.W., 1970. The hydraulics of overland flow on hillslopes, 662. US Government Printing Office.

Farenhorst, A., Bryan, R.B., 1995. Particle size distribution of sediment transported by shallow flow. CATENA 25(1), 47-62.

Finkner, S., Hearing, M., Foster, G., Gilley, J.E., 1989. A simplified equation for modeling sediment transport capacity. Transactions of the ASAE 32(5), 1545-1550.

Freebairn, D.M., Gupta, S.C., 1990. Microrelief, rainfall and cover effects on infiltration. Soil and Tillage Research 16(3), 307-327.

Gabet, E.J., Dunne, T., 2003. Sediment detachment by rain power. Water Resources Research 39(1), ESG-1.

Ghadiri, H., Rose, C.W., 1991. Sorbed Chemical Transport in Overland Flow: II. Enrichment Ratio Variation with Erosion Processes. Journal of Environmental Quality 20(3), 634-641.

Gilley, E.J., Kottwitz, R.E., 1995. Darcy-Weisbach Roughness Coefficients for Surfaces with Residue and Gravel Cover. Transactions of the ASAE 38(2), 539-544.

Govers, G., 1985. Selectivity and transport capacity of thin flows in relation to rill erosion. Catena 12(1), 35-49.

Govers, G., 1990. Empirical relationships for the transport capacity of overland flow. IAHS publication Catena 189, 45-63.

Guo, Z., Ma, M., Cai, C., Wu, Y., 2018. Combined effects of simulated rainfall and overland flow on sediment and solute transport in hillslope erosion. Journal of soils and sediments 18(3), 1120-1132.

Hu, Y., Fister, W., Kuhn, N.J., 2013. Temporal variation of SOC enrichment from interrill erosion over prolonged rainfall simulations. Agriculture Ecosystems & Environment 3(4), 726-740.

Jin, K., Cornelis, W., Gabriels, D., Baert, M., Wu, H., Schiettecatte, W., Cai, D., De Neve, S., Jin, J., Hartmann, R., 2009. Residue cover and rainfall intensity effects on runoff soil organic carbon losses. Catena 78(1), 81-86.

Jin, K., Cornelis, W.M., Gabriels, D., Schiettecatte, W., De Neve, S., Lu, J., Buysse, T., Wu, H., Cai, D., Jin, J., 2008. Soil management effects on runoff and soil loss from field rainfall simulation. Catena 75(2), 191-199.

Ketcheson, J., Stonehouse, D., 1983. Conservation tillage in Ontario. Journal of Soil Water Conservation 38(3), 253-254.

Klik, A., Rosner, J., 2020. Long-term experience with conservation tillage practices in Austria: Impacts on soil erosion processes. Soil and Tillage Research 203, 104669.

Laflen, J., Colvin, T., 1981. Effect of crop residue on soil loss from continuous row cropping. ransactions of the ASAE 24(3), 605-0609.
Lawrence, D.S.L., 1997. Macroscale surface roughness and frictional resistance in overland flow. Earth Surface Processes and Landforms 22(4), 365-382.
Leys, A., Govers, G., Gillijns, K., Berckmoes, E., Takken, I., 2010. Scale effects on runoff and erosion losses from arable land under conservation and conventional tillage: The role of residue cover. Journal of Hydrology 390(3), 143-154.
Liu, L., Li, Z., Xiao, H., Wang, B., Nie, X., Liu, C., Ni, L., Wang, D., 2019. The transport of aggregates associated with soil organic carbon under the rain-induced overland flow on the Chinese Loess Plateau. 44(10), 1895-1909.
Lu, J.Y., Cassol, E.A., Foster, G.R., Neibling, W.H., 1988. Selective transport and deposition of sediment particles in shallow flow. Transactions of the ASAE 31(4), 1141-1147.
M. Mohamoud, Y., K. Ewing, L., W. Boast, C., 1990. Small Plot Hydrology: I. Rainfall Infiltration And Depression Storage Determination. Transactions of the ASAE 33(4), 1121-1131.
Martínez-Mena, M., Alvarez Rogel, J., Castillo, V., Albaladejo, J., 2002. Organic carbon and nitrogen losses influenced by vegetation removal in a semiarid mediterranean soil. Biogeochemistry 61(3), 309-321.
Massey, H., Jackson, M., 1952a. Selective Erosion of Soil Fertility Constituents 1. Soil Science Society of America Journal 16(4), 353-356.
Massey, H.F., Jackson, M.L., 1952b. Selective Erosion of Soil Fertility Constituents. Soil Science Society of America Journal 16(4), 353-356.
Nie, X., Li, Z., He, J., Huang, J., Zhang, Y., Huang, B., Ma, W., Lu, Y., Zeng, G., 2015. Enrichment of organic carbon in sediment under field simulated rainfall experiments. Environmental earth sciences 74(6), 5417-5425.
Papanicolaou, A.N.T., Wacha, K.M., Abban, B.K., Wilson, C.G., Hatfield, J.L., Stanier, C.O., Filley, T.R., 2015. From soilscapes to landscapes: A landscape-oriented approach to simulate soil organic carbon dynamics in intensively managed landscapes. Journal of Geophysical Research: Biogeosciences 120(11), 2375-2401.
Parsons, A.J., Abrahams, A.D., Wainwright, J., 1994. On determining resistance to interrill overland flow. Water Resources Research 30(12), 3515-3521.
Pimentel, D., 2006. Soil erosion: a food and environmental threat. Environment, development sustainability 8(1), 119-137.
Schiettecatte, W., Gabriels, D., Cornelis, W., Hofman, G., 2008. Enrichment of organic carbon in sediment transport by interrill and rill erosion processes. Soil Science Society of America Journal 72(1), 50-55.
Shi, Z.H., Yue, B.J., Wang, L., Fang, N.F., Wang, D., Wu, F.Z., 2013. Effects of Mulch Cover Rate on Interrill Erosion Processes and the Size Selectivity of Eroded

Sediment on Steep Slopes. Soil Science Society of America Journal 77(1), 257-267.

Sturm, T.W., 2001. Open channel hydraulics. McGraw-Hill, New York.

Thaler, E.A., Larsen, I.J., Yu, Q., 2021. The extent of soil loss across the US Corn Belt. Proceedings of the National Academy of Sciences 118(8), e1922375118.

Wacha, K., Papanicolaou, A., Giannopoulos, C., Abban, B., Wilson, C., Zhou, S., Hatfield, J., Filley, T., Hou, T., 2018. The Role of Hydraulic Connectivity and Management on Soil Aggregate Size and Stability in the Clear Creek Watershed, Iowa. Geosciences 8(12), 470.

Wacha, K.M., Papanicolaou, A.T., Abban, B.K., Wilson, C.G., Giannopoulos, C.P., Hou, T., Filley, T.R., Hatfield, J.L., 2020. The impact of tillage row orientation on physical and chemical sediment enrichment. Agrosystems, Geosciences Environment international.

Wischmeier, W.H., 1973. Conservation tillage to control water erosion, pp. 133-141.

Zhang, Y., Zhao, Q., Cao, Z., Ding, S., 2019. Inhibiting Effects of Vegetation on the Characteristics of Runoff and Sediment Yield on Riparian Slope along the Lower Yellow River. Sustainability 11(13), 3685.

CHAPTER FIVE

QUANTIFYING AGGREGATE TRANSPORT DISTANCES TO UNDERSTAND SOIL ORGANIC CARBON REDISTRIBUTION USING RARE EARTH ELEMENT TRACERS

Abstract: Quantifying transport distances of soil aggregates is essential for understanding the fate of soil organic carbon (SOC) on the landscape. In this study, natural soil aggregates were separated into four size classes (8-19 mm, extra-large macroaggregates; 2-8 mm, large macroaggregates; 0.075-2 mm, small macroaggregates; <0.075 mm, fines) and tagged with rare earth elements (REE). The tagged aggregates were placed in plots that drained to a major flowpath in a field with freshly planted corn in the Goose Creek, IL, watershed. Surface soil samples were collected both within and downslope of each tagged plot following 70 mm rainfall which fell over ten events within 26 days. The transport distances of the different aggregate size fractions were determined by coupling the REE concentrations with existing diffusion and exponential transport models. The REE concentrations declined rapidly with downslope distance in the upper slope and were well represented by the exponential model. The predicted transport distances for all aggregate size fractions in this location were less than 1.5 cm, as rain splash and interill shallow flow were the dominant transport mechanisms. Conversely, the observed trend of REE concentrations at the toe-slope versus downslope distance was better described by the diffusion model, with predicted transport distances greater than 15 cm. This is attributed to higher slope gradients resulting in higher runoff amounts and more erosion. Variable transport distances were found based on aggregate size. The longest distances of transport were found for small macroaggregates (1.33-117 cm) due to the combination of their small size and low density from high SOC concentrations, inducing a low settling velocity. Finally, the shortest transport distances were observed for extra-large macroaggregates (0.97-36 cm) due to their larger size and higher density and consequently higher settling velocity. The measured SOC concentrations of the bulk soil increased with increasing distances downslope. These results expand the understanding and modeling of process-based soil erosion and SOC redistribution and stress the importance of aggregate sizes and topographic characteristics on soil transport distances.
Keywords: Soil aggregates, Transport distance, Rare earth element, Rainfall, Diffusion model, Exponential model, SOC redistribution

Introduction

Soil erosion consists of a sequence of steps including raindrop detachment, transport by overland flow, and deposition, which can collectively be quantified as a transport distance from the eroding source to the depositional sink (Dunne et al., 2010; Nearing et al., 1999; Polyakov and Nearing, 2003). Nonetheless, very few studies of the transport distance of soil particles have been undertaken. Transport distances dictate the spatial patterns of redistributed SOC over the landscape (Hu et al., 2016; Hu and Kuhn, 2014). This is essential information for process-based soil erosion and SOC transport models (Parsons et al., 2004; Wainwright et al., 2008a) and for locating erosion control practices to improve soil health (Burroughs Jr and King, 1989; Kuhn et al., 2009).

Transport distance is strongly affected by particle size (Kirkby, 2010; Kuhn et al., 2009) with a widely ascribed inverse relationship between particle size and settling velocity (Hairsine and Rose, 1991; Heng et al., 2011). Hu et al. (2016) studied the transport distance of soil aggregates along a slope after rainfall events. They found that larger aggregates were mainly distributed on the upper slope (implying shorter transport distances) and smaller aggregates were on the lower slope (implying longer transport distances). Additionally, the smaller particles carry with them more organic matter than larger particles (Hu and Kuhn, 2016; Nie et al., 2014; Schiettecatte et al., 2008), which may cause the commonly observed high SOC concentration in the downslope and low SOC concentration in the upslope (Hu et al., 2016; Kirkels et al., 2014; Papanicolaou et al., 2015). However, the studies mentioned above made inferences on travel distances of soil aggregates based upon their depositional locations which failed to yield information on their actual transport distances in field settings.

Over the past two decades, the use of rare earth elements (REEs) as tracers has increased for determining sediment source (Stevens and Quinton, 2008; Zhu et al., 2011), erosion rates (Lei et al., 2006; Liu et al., 2004; Zhang et al., 2008), and spatial patterns of soil redistribution (Polyakov et al., 2009; Polyakov and Nearing, 2004; Szabó et al., 2020). Conversely, the use of REEs to assess transport distance is relatively rare. REEs are good tracers due to their low concentration in natural soils, high adsorption capacity, noninterference with particle movement, and high detection sensitivity (Zhang et al., 2001; Zhang et al., 2003), which allow researchers to track the movement of single particles or aggregated soils across landscapes. Matisoff et al. (2001) placed different REE-tagged soils at the upper, middle, and lower slopes for determining soil transport distances after a thunderstorm event. However, Matisoff et al. (2001) used uniformly sized soil particles. Likewise, soil tagging using one tracer for all aggregate sizes could cause underestimation or overestimation of transport distance from a given area as finer soil fractions are preferentially eroded and travel longer distances. In comparison, coarser soil fractions tend to deposit fast and travel shorter distances.

In this study, natural soils were labeled with multi-REEs based on four size fractions and then applied to the upper-, mid-, and toe-slopes of the field to address the nonuniform transport issue of soil aggregates. Soil samples along the transport pathways were collected for REE analyses following a series of rainfall events. The objectives were to (1) quantify the transport distances of the four aggregate size fractions within each topographic position by coupling the REE concentrations and existing transport models and (2) investigate the resulting downslope patterns of SOC concentrations within each topographic position. By addressing these objectives, this study presents a new technique to assess aggregate transport distance based on their sizes and provides insights into relationship of transport distance and the interplay of aggregate sizes and topographic characteristics.

Materials and Methods

Site Description

This study was conducted in an agricultural field (0.085-km^2) located in the Goose Creek watershed near De Land, Illinois (40°08'39.4"N, 88°36'37.0"W; Figure 5-1a). This region was a product of the Wisconsin glaciation period (~25-75 ka), which left it with a low-relief landscape and large quantities of fine-grained materials in the soil (Anders et al., 2018). The soil classified as a Sable silty clay loam (fine-silty, mixed, superactive, mesic Typic Endoaquolls), containing 66% silt, 32% clay, 2% sand, and 3% SOC (USDA-NRCS SSURGO). Because of the high amounts of silt and clay, soil crusting is likely to occur following rain events, which reduces water infiltration and induces erosion through increased runoff (Bissonnais and Singer, 1992). The field had a slope of 0.15% on average with a 300-m long main flowpath running parallelly to the tillage contours (east-west flow) in the upper part and perpendicularly (north-south flow) in the lower part (Figure 5-1b). This study focused on the lower part where more concentrated overland flow would like to occur and more pronounced aggregate transport was expected (Figure 5-1c).

The average annual precipitation in this location was 1000 mm with the majority occurring in spring and early summer when this study was performed. During this time, heavy convectional storms prevailed in conjunction with tilled surface soil exposure to raindrops and runoff without canopy protection, resulting in severe topsoil loss by erosion. Soil erosion rate in this field has not been previously determined, but our (unpublished) preliminary modeling results using the Revised Universal Soil Loss Equation showed that the erosion rate in May and June of 2017 and 2018 was 0.28 ± 0.09 kg m^{-2} yr^{-1} on average, which was less than the soil tolerance value of 13 kg m^{-2} yr^{-1} for this type of soil (Harshbarger and Swanson, 1964).

Aggregate Preparation and Application

Three positions were selected along the lower part of the main flowpath following the steepest line of descent, designated as the upper-, mid-, and toe-slopes. About 30 kg of soils were collected from each position in October 2018 after harvest and again in April 2019 before planting (Figure 5-1c). The soils were air-dried and separated into four aggregate size fractions by dry sieving: extra-large macroaggregates (8-19 mm, X), large macroaggregates (2-8 mm, L), small macroaggregates (0.075-2 mm, S), and fines (<0.075 mm, F). Each aggregate size fraction was labeled with a different REE powder using the repeated wetting-drying method (Polyakov et al., 2004): Ytterbium, Yb → X, Erbium, Er → L, Gadolinium, Gd → S, and Samarium, Sm → F. The four REE-labeled aggregate fractions from each slope position were ultimately recombined to match the aggregate size distribution determined with dry sieving (Figure 5-2). Details of the aggregate separation, REE properties, and aggregate labeling were described in Chapter 3.

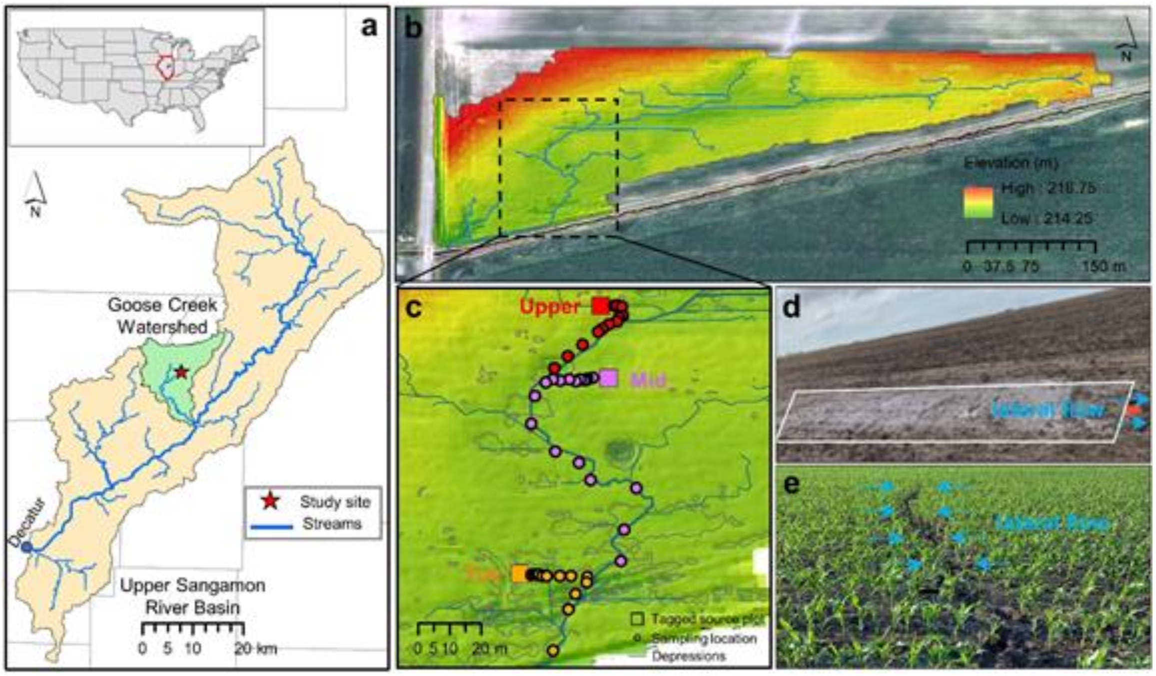

Figure 5-1. (a) Location of the study site in the Goose Creek watershed of the Upper Sangamon River Basin in central Illinois, USA**;** (b) Map of elevation and flowpaths of the agricultural field where the experiment was conducted; (c) Map of the rare earth element tagged source plots (square) and soil sampling transects (dots) at the upper-, mid-, and toe-slopes. Gray polygons denote the locally topographical depressions; (d) Side view of a tagged plot at the upper slope right after the aggregate application (May 29, 2019); (e) Field image of the main flowpath 22 days (June 20, 2019) after the aggregate application. Cyan arrows denote directions of the lateral flow delivering to the main flowpath.

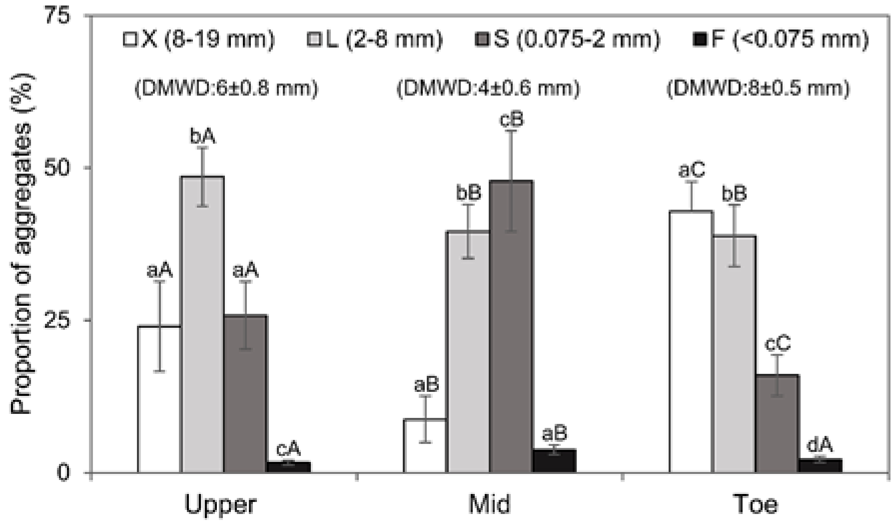

Figure 5-2. The initial mass proportion of the four aggregate size fractions in the soil used to tag the source plots at the upper-, mid-, and toe-slopes. Different lowercase letters denote significant differences at $P < 0.05$ among aggregate size fractions at the same slope location. Different uppercase letters denote significant differences at $P < 0.05$ among slope locations for the same aggregate size fraction.

On May 29, 2019 (Day 0), about 20 kg of REE-labeled aggregates were uniformly broadcast over the rectangular plots at the upper-, mid-, and toe-slopes (Figure 5-1c), using a 56-cm wide lawn spreader. The longer side of each plot was aligned with the cornrows, which ran perpendicularly to the main flowpath (Figure 5-1d and e). The three tagged plots differed slightly in dimensions and local slope gradients (Table 5-1). The toe slope plot was surrounded by more topographic depressions than the upper- and mid-slope plots (Figure 5-1c). One week before applying the labeled aggregates, the field was disked and planted with corn and left with about 5% decomposed corn residue. Over the subsequent study period, the corn plants evolved from seed germination to a maximum height of 30 cm, leading to aggregate exposure to raindrop impacts and overland flow wash (particularly early in the study).

Sample Collection and Analyses

On June 24, 2019 (Day 26), after three periods of rain, surface soil samples were collected in a uniform volume (12.8 cm × 9.5 cm × 1 cm deep) both within and downslope from the lower edge of each tagged plot at logarithmically increasing distances from 5-10 cm to 13-78 m perpendicular to and then along the main flowpath (Figure 5-1c). Soil samples along the transport pathways were particularly collected from those intermittent depositional patches (Figure 5-3). Rainfall was measured every 15 min by an eddy covariance flux tower (Campbell Scientific, Inc.) which was 2 km northeast of the field. Over the 26 days, ten rain events occurred in three distinct periods (Day 0 – Day 2; Day 14 – Day 15; Day 21 – Day 26), totaling 70 mm of rainfall. Shallow sheet flow was observed in the cornrows and the main flowpaths during extreme rainfall events.

The soil collected was air-dried and then crushed to less than 2 mm using a wooden rolling pin. The REEs were extracted from a 2-g subsample using acid digestion (USEPA, 1996). The concentrations of the REEs were measured on an inductively coupled plasma mass spectrometry (ICP-MS) Agilent 8900 ICP-QQQ (Santa Clara, CA) at the Arizona Laboratory for Emerging Contaminants (see the extraction of REEs detailed in Chapter 3). Subsamples of ~15 g were used to determine the SOC concentration using the visible and near-infrared spectroscopy (Chapter 2).

Soil Transport Models

Models of soil transport in the agricultural context have different underpinnings. One approach to represent soil particle transport on hillslope, such as soil creep, is to use a diffusion model (Dietrich et al., 2003; Heimsath et al., 1997; McKean et al., 1993). Bedload transport is often described as combined advection-dispersion processes (Schumer et al., 2009; Lajeunesse et al., 2018). A particle entrained by the flow especially by shallow flow can repeatedly settle back to the bed, where they can remain trapped for a long time before moving with flow again. This behavior is analogous to the diffusive motion (Fathel et al., 2016). Mathematical models describing rainsplash transport in interrilll erosion has been formulated as an exponential equation ((Van Dijk et al., 2002; Van Dijk et al., 2003;

Table 5-1. Characteristics of the tagged source plots at the upper-, mid-, and toe-slopes.

Slope location	Length (m)	Width (m)	Slope (%)	Flowpath length (m)	Aggregate applied (kg)
Upper	9.0	2.4	0.4	27	22
Mid	7.9	1.8	0.1	78	20
Toe	7.3	5.0	0.6	30	21

Figure 5-3. Field images showing (a) the depositional patches of sediments and (b) soil sample collection from these patches using a rectangular metal frame (12.8 cm long by 9.5 cm wide).

Wainwright et al., 2008a). In this studied low-gradient field, transport of the REE-labeled aggregates may occur by rainsplash and by shallow flow entrainment. As a consequence, both diffusion and exponential models were used to describe the transport of aggregates to permit comparisons of aggregate transport distances calculated with both models and identifications of governing mechanisms of transport.

The diffusion model assumes that aggregate transport can be mathematically described as simple and one-dimensional diffusion according to Matisoff et al. (2001):

$$\frac{\partial C}{\partial t} = D_p \frac{\partial^2 C}{\partial x^2} \quad \text{5-1}$$

where *C* is the REE concentration (ppm), t is time (s), D_p is the particle diffusion coefficient ($cm^2\ s^{-1}$), and x is the downslope distance (m). Eq. 5-1 can be solved with a Gaussian function:

$$C(x,t) = C_0 + \frac{(C_m - C_0)}{\sigma\sqrt{2\pi}} \exp\,[\frac{(x-\mu)^2}{2\sigma^2}] \quad \text{5-2}$$

where C_m is the maximum concentration of REE (ppm) in tagged soil, C_0 is the background concentration of REEs (ppm) in untagged soils, μ is the downslope position of the maximum tracer concentration (the transport distance (cm) of the entire center of mass of the tagged aggregates), σ is the spread of the peak concentration and represents the transport distance (cm) caused by particle diffusion. In this study, σ was determined by fitting Eq. 5-2 to the REE concentration *versus* distance data.

The exponential model assumes that aggregate transport can be described also as an exponential function of distance (Matisoff et al., 2001):

$$C(x) = C_0 + (C_m - C_0)\exp(-kx) \quad \text{5-3}$$

where $C(x)$ is the REE concentration (ppm) in the eroded soil at downslope distance x (m), C_0 is the background concentration of REEs (ppm) in untagged soils, C_m is the REE concentration (ppm) at the source, and $1/k$ is the characteristic transport distance (cm), which was determined by fitting Eq.5-3 to the REE concentration *versus* distance data.

Results

Rainfall

As noted in the “sample collection and analyses” section, 70 mm of rain fell in the field in three distinct periods (Day 0 – Day 2; Day 14 – Day 15; Day 21 – Day 26, see Figure 5-4). In the first period, a 4-h event occurred less than 7 hours after the aggregate broadcast providing 10 mm of rainfall with a maximum intensity of 18.29 mm h^{-1} (Table 5-2). This was followed over the next two days with two scattered, light events producing 4 mm of rainfall. The second period consisted of a single 19 mm thunderstorm (5.25-h) occurred

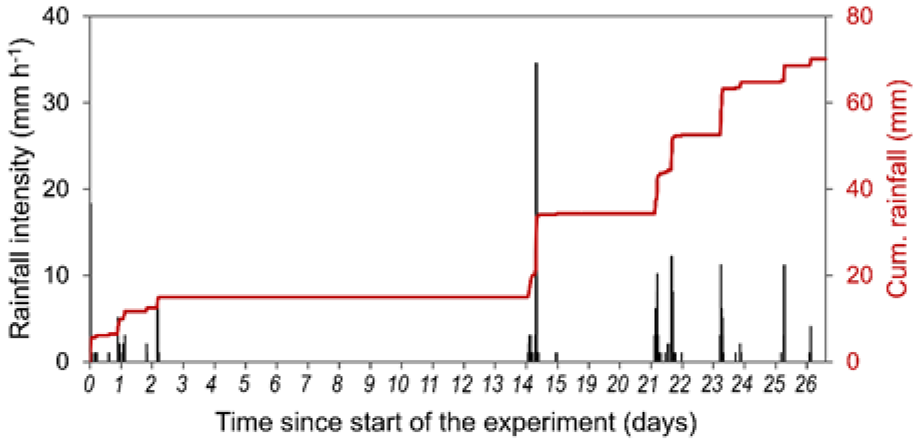

Figure 5-4. Rainfall intensity and cumulative rainfall over the study period. Data on 16-18 days are missing. Detailed characteristics of the rainfall events are given in Table 5-2.

Table 5-2. Rain events and their characteristics over the study period.

Rain event	Date	Exp. time (d)	Duration (h)	Rainfall amount (mm)	Max. intensity (mm h^{-1})
R1	5/29	0	4.00	9.91	18.29
R2	5/30	1	1.00	1.78	3.05
R3	5/31	2	1.00	2.54	6.10
R4	6/12	14	5.25	19.05	34.56
R5	6/13	15	0.25	0.25	1.02
R6	6/19	21	3.75	13.46	12.19
R7	6/20	22	1.25	4.83	8.13
R8	6/22	24	1.25	1.52	2.03
R9	6/23	25	0.75	3.81	11.18
R10	6/24	26	0.75	1.52	4.06

14 days after the broadcast with a maximum intensity of 34.56 mm h^{-1} (the largest event during the study). The third period of rainfall comprised five small events accumulating 25 mm of rainfall with a maximum intensity of 12.19 mm h^{-1}. In total, June 2019 was a particularly dry month in which 82 mm of precipitation fell compared to the June 2015-2020 monthly average of 124 mm. As such, less soil movement than normal was expected.

Aggregate Transport Distance along the Slope

Figure 5-5 shows the REE concentration versus distance data for all transects at the upper-, mid-, and toe-slopes and their curve fits for the diffusion model (black line; Eq.5-2) and the exponential model (red line; Eq.5-3). The coefficients of determination (R^2) and root-mean-square deviation (RMSE) of the model fits and the calculated transport distances of aggregate fractions are presented in Table 5-3. In all cases, the REE concentrations were at their peak near the tagged soil origin, decreased rapidly downslope, and neared background concentrations further from the tagged locations. However, the specific curve fits for each slope position differed slightly. At the upper slope (Figure 5-5a, b, c, and d), all REE concentrations showed a cliff-like decline to background concentrations moving from the tagged location to downslope untagged locations. For this plot, the trends were better described by the exponential model (R2=0.99; RMSE=0.34-1.14) than by the diffusion model (R^2 = 0.04-0.09; RMSE=117-864). At the mid-slope, the Yb and Sm concentrations versus distance (Figure 5-5e and h) were similar in form to those at the upper slope, which were better represented by the exponential model (R^2= 0.86-0.99; RMSE=2.65-17) than by the diffusion model (R^2=0.06-0.32; RMSE=37-140). Conversely, Er and Gd concentrations versus distance (Figure 5-5f and g) fitted slightly better to the diffusion model (R^2 = 0.87-0.88) than to the exponential model (R^2=0.77-0.85). Finally, at the toe slope (Figure 5-5i, j, k, and l), all REE concentrations raised to peak values 28-114 cm downslope from the tagged location and then dropped rapidly to background levels further down the flow pathway. Here, the REE concentrations were better characterized by the diffusion model (R^2=0.82-0.99) than by the exponential model (R^2=0.26-0.56).

Particle transport distances were determined for each plot based on the model shown to better fit the field data. At the upper slope, particle transport distances derived from the exponential model ranged from 0.97 cm to 1.46 cm (Table 5-3). At the mid-slope, particle transport distances derived from the exponential model were 2 cm for extra-large macroaggregates, 98 cm for large macroaggregates, 117 cm for small macroaggregates, and 103 cm for fines. At the toe slope, transport distances obtained from the diffusion model were 15 cm for extra-large macroaggregates, 26 cm for large macroaggregates, 38 cm for small macroaggregates, and 23 cm for fines. Overall, at all slope positions, transport distances were the greatest for small macroaggregates (52 ± 59 cm) and the smallest for extra-large macroaggregates (6 ± 8 cm). Large macroaggregates (42 ± 50 cm) and fines (42 ± 54 cm) had intermediate and similar transport distances. For a given

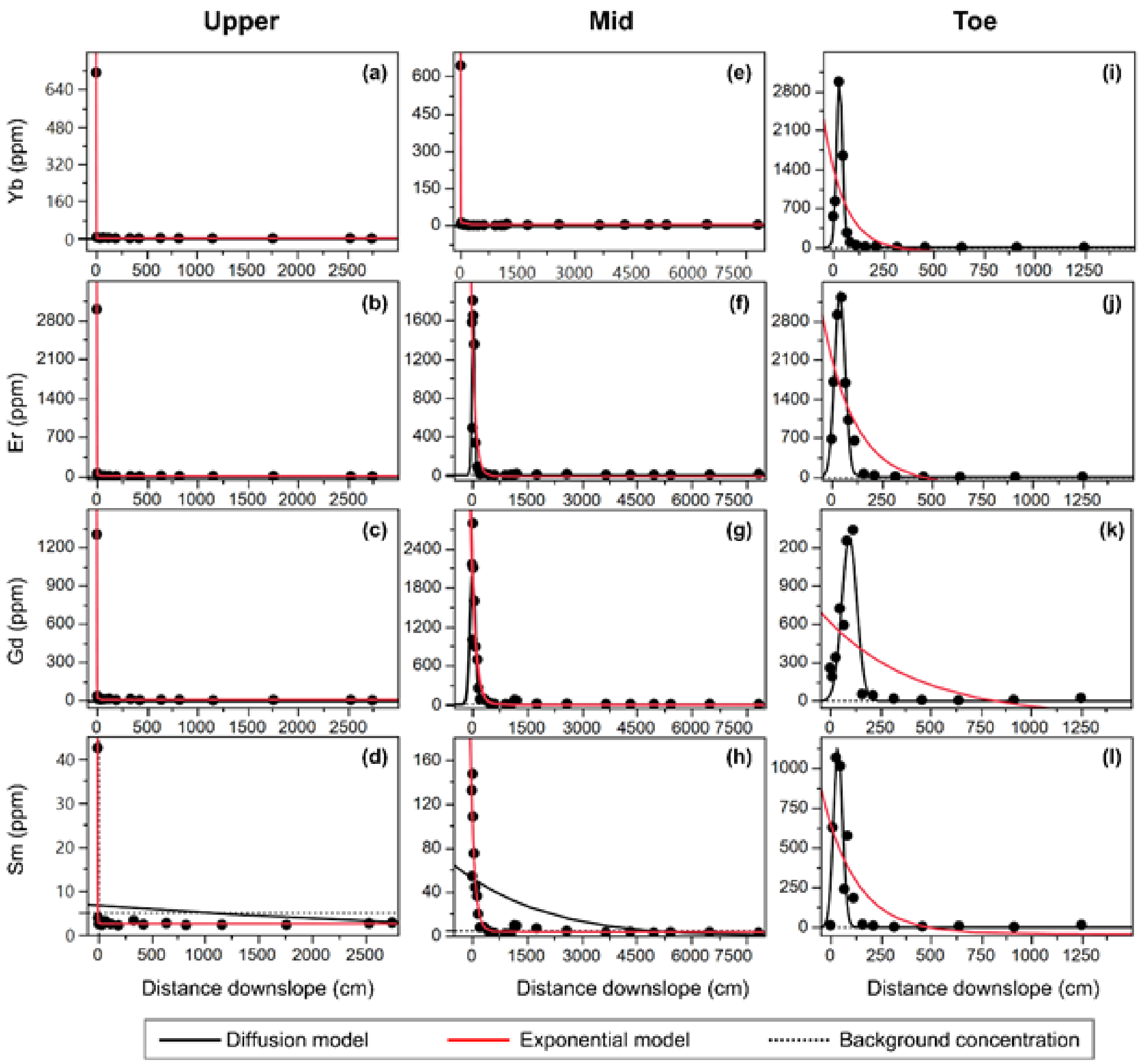

Figure 5-5. Concentrations of the four rare earth tracers along each of the downslope transects at the upper-, mid-, and toe-slopes (dots), diffusion model fits (black lines), exponential model fits (red lines), and background concentrations of the rare earth element in untagged soils (dash lines). Downslope distances are sampling distances measured from the lower end of the tagged soil plot. Calculated transport distances are given in Table 5-3.

Table 5-3. Diffusion and exponential model fits and calculated transport distances of the four aggregate size fractions at the upper-, mid-, and toe-slope locations [a].

Slope location	REE	Assigned aggregates	R^2		RMSE		Transport distance (cm)	
			Diffusion model	Exponential model	Diffusion model	Exponential model	Diffusion model [b]	Exponential model [c]
Upper	Yb	X	0.08	**0.99**	205	**1.14**	3931	**0.97**
	Er	L	0.08	**0.99**	864	**6.16**	3093	**1.22**
	Gd	S	0.09	**0.99**	375	**4.19**	3643	**1.33**
	Sm	F	0.04	**0.99**	117	**0.34**	8472	**1.46**
Mid	Yb	X	0.06	**0.99**	140	**2.65**	27972	**2.00**
	Er	L	**0.87**	0.77	**226**	299	**36**	98
	Gd	S	**0.88**	0.85	**297**	333	**73**	117
	Sm	F	0.32	**0.86**	37	**17**	5556	**103**
Toe	Yb	X	**0.99**	0.39	**108**	726	**15**	106
	Er	L	**0.97**	0.56	**213**	809	**26**	163
	Gd	S	**0.88**	0.26	**175**	429	**38**	486
	Sm	F	**0.82**	0.43	**177**	320	**23**	173

[a] Model fits are shown in solid lines for the diffusion model and dashed lines for the exponential model in Figure 5-5. [b] Transport distance =σ. [c] Transport distance=1/k. X, L, S, and F indicate the extra-large macroaggregates (8-19 mm), large macroaggregates (2-8 mm), small macroaggregates (0.075-2 mm), and fines (<0.075 mm). Bold numbers mark the model with a better fit.

size fraction, transport distance at the mid-slope was generally the longest (80 ± 53 cm), followed by those at the toe slope (26 ± 10 cm). No significant translocations were found in the four fractions at the upper slope (1.25 ± 0.21 cm).

Spatial Distribution of Eroded SOC

The relationships between the SOC concentrations of eroded aggregates and the distances downslope for the upper-, mid-, and toe-slope transects are shown in Figure 5-6. In all cases, the SOC concentrations increased with increasing distances downslope from the tagged source plots. This increasing trend was found to be more significant at the toe slope (R^2 = 0.36) than at the mid-slope (R^2 = 0.17) and the upper slope (R^2 = 0.05). The toe-slope transect (2.74 ± 0.14 %) had a slightly higher SOC concentration on average than the mid-slope (2.54 ± 0.11 %) and the upper-slope (2.48 ± 0.07 %).

Discussion

It is generally accepted that natural soils are eroded as individual particles and as aggregates, for which different physical characteristics lead to variable transport distances (Bonniwell et al., 1999; Wacha et al., 2018). The use of multi-REEs to differentially tag aggregate size fractions permits tracing the dynamic transport of soil aggregates and disentangles differences in transport distances. Tagging natural soils from the test locations minimized the differences in particle size, particle density, and SOC content compared to untagged soil (Matisoff et al., 2001). Therefore, the tagged aggregates are expected to have similar behavior as the untagged aggregates during erosional transport. With this expectation, the results of the experiments reported above, to the best of our knowledge, provide the first actual transport distances for four consecutive aggregate size fractions at the field scale under natural rainfall conditions.

The REE concentrations in the four aggregate fractions at the upper slope decreased precipitously to background concentrations downslope from the plot, being best described mathematically by the exponential model. These findings are consistent with those reported for rain splash transport (Van Dijk et al., 2003; Van Dijk et al., 2002), in which the spatial distribution of transported particles from a point source is described by an exponential decay function. In this study, raindrop detachment and interrill flow are likely to be the main mechanisms for aggregate transport in the upper slope because the slope gradient (0.4%) is very low and concentrated overland flow may be absent (especially during light events) or too weak to mobilize the soil particles (Hairsine and Rose, 1991). Other distribution functions such as the gamma distribution have been suggested for representing the transport distances for particles in interrill flow (Hassan et al., 1991; Wainwright et al., 2008b). The exponential distribution provides a special case of the gamma distribution with most sediments traveling a short distance before settling (Parsons and Stromberg, 1998).

In contrast to what is observed in the upper slope, the REE concentrations *versus* distance data at the toe-slope were well represented by the diffusion model, consistent

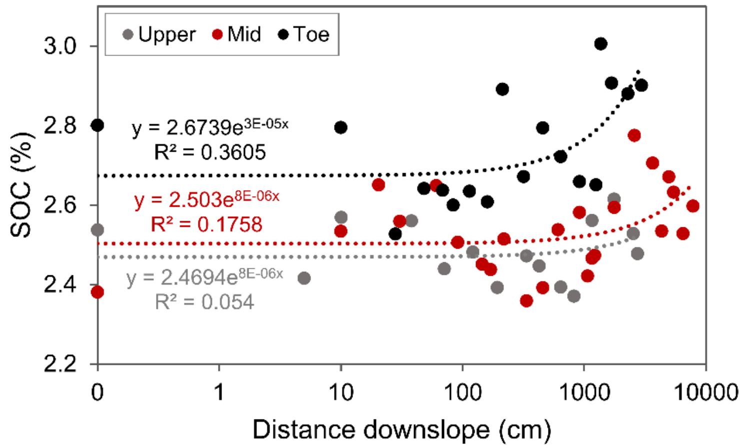

Figure 5-6. The relationship between SOC concentration of eroded aggregates and downslope distance for the upper-, mid-, and toe-slopes transects.

with results from Matisoff et al. (2001) for the same topographic position. The diffusion model has commonly been used to characterize soil creep (Furbish et al., 2017; Roering et al., 1999). It is likely that aggregates at the toe slope slide slowly along the bed surface under low slope induced shallow weak flow, which propagates downslope movement of aggregates analogously as diffusion. Aggregate transport at the mid-slope exhibited both exponential and diffusion characteristics, indicating that aggregate movement at the mid-slope is in transition from rainsplash-dominated transport to shallow runoff-dominated transport (Papanicolaou et al., 2015).

The transport distance predicted by the models generally decreased with increasing aggregate sizes (Table 5-3), which broadly follows the trend reported for coarse sand particles by previous studies (Parsons and Stromberg, 1998; Parsons et al., 1998). Transport distance is rooted in size governed settling velocity, in which larger aggregates settle faster, resulting in shorter transport distance, and smaller aggregates settle slower, leading to longer transport distance (Hairsine et al., 1999; Shi et al., 2012). This can also be supported by the widely observed finer aggregate size distribution in eroded sediments compared to source soil (Alberts et al., 1980). In this study, the fines (namely silt- and clay-sized particles) at the toe slope surprisingly had a shorter transport distance (23 cm) than the small macroaggregates (38 cm), which seems to conflict with the theory of finer particles traveling longer distances than coarser particles. This is probably due to the extremely low mass proportion of fines in the tagged soil (2%; Figure 5-2). On the other hand, small macroaggregates could be the easiest fraction to transport (Liu et al., 2019; Sutherland et al., 1996) as they have the highest SOC concentration and resultant low density (Ruehlmann and Körschens, 2009; Chapter 3).

The aggregate transport distances from the mid- and toe-slope plots were greater than those at the upper-slope plot, likely due to the smaller slope gradients on the summit top than on the mid- and toe-slope faces. The combination of greater slope gradients and the consequent greater amount of fast-moving runoff would result in longer transport distances (Papanicolaou et al., 2018). The primary depositional sites are the local depressions at the toe slope and the grass buffer strips on the edge of the field (Figure 5-1b and c), although a few depressions at the mid-slope could also collect some soil in transit. Overall, the results of this study indicate that transport distances of the aggregates in the fields are short. The relatively short study period (about one month) and light events could be the reason of the observed short distances of transport.

There is a consensus that erosional transport of soil redistributes a large quantity of SOC over the landscape (Doetterl et al., 2016; Kirkels et al., 2014; Zhang et al., 2006), and the site of SOC deposition depends on the transport distances of the soil aggregates containing the SOC (Hu and Kuhn, 2016). Consistent with other researchers (Hu et al., 2016; Li et al., 2018; Yoo et al., 2006), SOC concentrations in the eroded aggregates were found to increase with increasing downslope distance from the tagged sites. These results demonstrate the impact of transport distances on the spatial patterns of SOC redistribution. The observed high SOC concentrations in the downslope far from the tagged sources are likely to be associated with those fractions with long travel distances, which was found herein to be the small macroaggregates (Table 5-3). This is supported by the previous work in Chapter 3 on soils from the same location, in which small macroaggregates were found to contain the highest SOC concentration. A considerable number of studies have also shown the preferential accumulation of SOC in macro- and micro-aggregates due to their large specific surface area and strong binding agents of microbial and plant exudates (An et al., 2010; Oades, 1984; Six et al., 2000). Therefore, the SOC-enriched small macroaggregates appear to be highly influential in this landscape as they are preferentially eroded and transported long distances before coming to rest, effectively reshaping the spatial distribution of SOC.

Conclusions

This study investigated the transport distances of soil aggregates within three hillslope topographic positions in an agricultural field following a series of rainfall events using rare earth elements (REEs) tracing and established transport models. In all instances, REE concentrations decreased rapidly downslope, from peak concentrations near the locations where the tagged soils were placed, to background concentrations just down gradient. In the upper slope, this rapid drop-off in REEs concentrations was well represented by the exponential model, and the predicted transport distances for all aggregate size fractions are very short (0.97-1.46 cm). This was attributed to the small local slope gradients, rain splash, and interill shallow flow being the dominant transport mechanisms. However, in the toe-slopes, the REEs concentration profiles were better described by the diffusion model, and the predicted transport distances (15-38 cm) are longer than those in the upper slope. Soil transport at the mid-slope exhibited both diffusion and exponential characteristics dependent on sizes and had the largest transport distance variations (2-103 cm). This is attributable to the greater local slope gradients and the consequent greater amount of high-velocity runoff. Meanwhile, the analogous soil creeps induced by the combination of low slopes and rainfall (which is better represented by diffusion models) could have caused aggregates to migrate. Finally, consistent with the literature, the transport distances at given slope positions varied with aggregate size. The longest distances of transport were found for small macroaggregates (52 ± 59 cm), which, although counterintuitive, was attributed to their combination of small size and having the highest SOC concentration of any of the particle size groups. The shortest transport distances were found for extra-large macroaggregates (6 ± 8 cm) because of their large size and consequently fast settling velocity. The varying transport distances of the eroded aggregates regulate the spatial patterns of SOC redistribution, in which the SOC concentrations increased with increasing distances downslope. For the first time, this study quantified the actual transport distances for various aggregate size fractions in the field under natural rainfall conditions, providing invaluable insights into modeling process-based soil and SOC redistribution by accounting for the interplaying effects of aggregate sizes and local topographic characteristics. Future studies will explore the possibility of the applied material traveling into neighboring streams through rills and gullies.

Acknowledgments

This research was supported by the National Science Foundation for the IML-CZO project [grant number EAR1331906], a multi-institutional collaborative effort. The REE concentrations were analyzed with ICP-MS by the Arizona Laboratory for Emerging Contaminants (ALEC) at the University of Arizona, Tucson, AZ. The authors would like to thank Dr. Andrew Stumpf from the Illinois State Geological Survey and Dr. Bruce Rhoads from the University of Illinois Urbana-Champaign for assisting the field experiment. The first author was part of the China-UT EcoPartnership Scholars Program and is grateful for the support of the China Scholarship Council.

References

Alberts, E.E., Moldenhauer, W.C., Foster, G., 1980. Soil Aggregates and Primary Particles Transported in Rill and Interrill Flow 1. Soil Science Society of America Journal 44(3), 590-595.

An, S., Mentler, A., Mayer, H., Blum, W.E.H., 2010. Soil aggregation, aggregate stability, organic carbon and nitrogen in different soil aggregate fractions under forest and shrub vegetation on the Loess Plateau, China. CATENA 81(3), 226-233.

Anders, A.M., Bettis III, E.A., Grimley, D.A., Stumpf, A.J., Kumar, P., 2018. Impacts of Quaternary History on Critical Zone Structure and Processes: Examples and a Conceptual Model From the Intensively Managed Landscapes Critical Zone Observatory. Frontiers in Earth Science 6, 24.

Bissonnais, Y.L., Singer, M.J., 1992. Crusting, Runoff, and Erosion Response to Soil Water Content and Successive Rainfalls. Soil Science Society of America Journal 56(6), 1898-1903.

Burroughs Jr, E.R., King, J.G., 1989. Reduction of soil erosion on forest roads.

Cheng, N.-S., 2002. Exponential formula for bedload transport. ournal of Hydraulic Engineering 128(10), 942-946.

Dietrich, W.E., Bellugi, D.G., Sklar, L.S., Stock, J.D., Heimsath, A.M., Roering, J.J., 2003. Geomorphic transport laws for predicting landscape form and dynamics. Geophysical Monograph-American Geophysical Union Geological Society of America Bulletin 135, 103-132.

Doetterl, S., Berhe, A.A., Nadeu, E., Wang, Z., Sommer, M., Fiener, P., 2016. Erosion, deposition and soil carbon: A review of process-level controls, experimental tools and models to address C cycling in dynamic landscapes. Earth-Science Reviews 154, 102-122.

Dunne, T., Malmon, D.V., Mudd, S.M., 2010. A rain splash transport equation assimilating field and laboratory measurements. Journal of Geophysical Research: Earth Surface 115(F1).

Fathel, S., Furbish, D., Schmeeckle, M., 2016. Parsing anomalous versus normal diffusive behavior of bedload sediment particles. Earth Surface Processes and Landforms 41(12), 1797-1803.

Furbish, D.J., Fathel, S.L., Schmeeckle, M.W., Jerolmack, D.J., Schumer, R., 2017. The elements and richness of particle diffusion during sediment transport at small timescales. Earth Surface Processes and Landforms 42(1), 214-237.

Hairsine, P., Rose, C., 1991. Rainfall detachment and deposition: Sediment transport in the absence of flow-driven processes. Soil Science Society of America Journal Erosion, conservation 55(2), 320-324.

Hairsine, P., Sander, G., Rose, C., Parlange, J.-Y., Hogarth, W., Lisle, I., Rouhipour, H., 1999. Unsteady soil erosion due to rainfall impact: a model of sediment sorting on the hillslope. Journal of Hydrology 220(3-4), 115-128.

Harshbarger, C., Swanson, E., 1964. Soil Loss Tolerance and the Economics of Soil Conservation on Swygert Soils. Illinois Agricultural Economics 4(2), 18-29.

Hassan, M.A., Church, M., Schick, A.P., 1991. Distance of movement of coarse particles in gravel bed streams. Water Resources Research 27(4), 503-511.

Heimsath, A.M., Dietrich, W.E., Nishiizumi, K., Finkel, R.C., 1997. The soil production function and landscape equilibrium. Nature 388(6640), 358-361.

Heng, B.C.P., Sander, G.C., Armstrong, A., Quinton, J.N., Chandler, J.H., Scott, C.F., 2011. Modeling the dynamics of soil erosion and size-selective sediment transport over nonuniform topography in flume-scale experiments. Water Resources Research 47(2).

Hu, Y., Berhe, A.A., Fogel, M.L., Heckrath, G.J., Kuhn, N.J., 2016. Transport-distance specific SOC distribution: Does it skew erosion induced C fluxes? Biogeochemistry 128(3), 339-351.

Hu, Y., Kuhn, N., 2014. Aggregates reduce transport distance of soil organic carbon: are our balances correct? Biogeosciences 11, 6209-6219.

Hu, Y., Kuhn, N.J., 2016. Erosion-induced exposure of SOC to mineralization in aggregated sediment. CATENA 137, 517-525.

Kirkby, M.J., 2010. Distance, time and scale in soil erosion processes. Earth Surface Processes and Landforms 35(13), 1621-1623.

Kirkels, F.M.S.A., Cammeraat, L.H., Kuhn, N.J., 2014. The fate of soil organic carbon upon erosion, transport and deposition in agricultural landscapes — A review of different concepts. Geomorphology 226, 94-105.

Kuhn, N.J., Hoffmann, T., Schwanghart, W., Dotterweich, M., 2009. Agricultural soil erosion and global carbon cycle: controversy over? Earth Surface Processes and Landforms 34(7), 1033-1038.

Lajeunesse, E., Devauchelle, O., James, F., 2018. Advection and dispersion of bed load tracers. Earth Surface Dynamics 6(2), 389-399.

Lei, T.W., Zhang, Q.W., Zhao, J., Nearing, M.A., 2006. Tracing sediment dynamics and sources in eroding rills with rare earth elements. European Journal of Soil Science 57(3), 287-294.

Li, X., McCarty, G.W., Karlen, D.L., Cambardella, C.A., Effland, W., 2018. Soil Organic Carbon and Isotope Composition Response to Topography and Erosion in Iowa. Journal of Geophysical Research: Biogeosciences 123(12), 3649-3667.

Liu, L., Li, Z., Xiao, H., Wang, B., Nie, X., Liu, C., Ni, L., Wang, D., 2019. The transport of aggregates associated with soil organic carbon under the rain-induced overland flow on the Chinese Loess Plateau. 44(10), 1895-1909.

Liu, P.-L., Tian, J.-L., Zhou, P.-H., Yang, M.-Y., Shi, H., 2004. Stable rare earth element tracers to evaluate soil erosion. Soil and Tillage Research 76(2), 147-155.

Matisoff, G., Ketterer, M.E., Wilson, C.G., Layman, R., Whiting, P.J., 2001. Transport of Rare Earth Element-Tagged Soil Particles in Response to Thunderstorm Runoff. Environmental Science & Technology 35(16), 3356-3362.

McKean, J.A., Dietrich, W.E., Finkel, R.C., Southon, J.R., Caffee, M., 1993. Quantification of soil production and downslope creep rates from cosmogenic 10Be accumulations on a hillslope profile. Geology 21(4), 343-346.

Nie, X., Li, Z., Huang, J., Huang, B., Zhang, Y., Ma, W., Hu, Y., Zeng, G., 2014. Soil organic carbon loss and selective transportation under field simulated rainfall events. PloS one 9(8).

Oades, J.M., 1984. Soil organic matter and structural stability: mechanisms and implications for management. Plant and Soil 76(1-3), 319-337.

Papanicolaou, A.N., Abban, B.K.B., Dermisis, D.C., Giannopoulos, C.P., Flanagan, D.C., Frankenberger, J.R., Wacha, K.M., 2018. Flow Resistance Interactions on Hillslopes With Heterogeneous Attributes: Effects on Runoff Hydrograph Characteristics. Water Resources Research 54(1), 359-380.

Papanicolaou, A.N.T., Wacha, K.M., Abban, B.K., Wilson, C.G., Hatfield, J.L., Stanier, C.O., Filley, T.R., 2015. From soilscapes to landscapes: A landscape-oriented approach to simulate soil organic carbon dynamics in intensively managed landscapes. Journal of Geophysical Research: Biogeosciences 120(11), 2375-2401.

Parsons, A.J., Stromberg, S.G.L., 1998. Experimental analysis of size and distance of travel of unconstrained particles in interrill flow. Water Resources Research 34(9), 2377-2381.

Parsons, A.J., Stromberg, S.G.L., Greener, M., 1998. Sediment-transport competence of rain-impacted interrill overland flow. Earth Surface Processes and Landforms 23(4), 365-375.

Parsons, A.J., Wainwright, J., Mark Powell, D., Kaduk, J., Brazier, R.E., 2004. A conceptual model for determining soil erosion by water. Earth Surface Processes and Landforms 29(10), 1293-1302.

Polyakov, V., Kimoto, A., Nearing, M., Nichols, M., 2009. Tracing sediment movement on a semiarid watershed using rare earth elements. Soil Science Society of America Journal 73(5), 1559-1565.

Polyakov, V., Nearing, M., 2003. Sediment transport in rill flow under deposition and detachment conditions. Catena 51(1), 33-43.

Polyakov, V., Nearing, M., 2004. Rare earth element oxides for tracing sediment movement. Catena 55(3), 255-276.

Polyakov, V., Nearing, M., Shipitalo, M., 2004. Tracking sediment redistribution in a small watershed: implications for agro-landscape evolution. Earth Surface Processes and Landforms: The Journal of the British Geomorphological Research Group 29(10), 1275-1291.

Roering, J.J., Kirchner, J.W., Dietrich, W.E., 1999. Evidence for nonlinear, diffusive sediment transport on hillslopes and implications for landscape morphology. Water Resources Research 35(3), 853-870.

Ruehlmann, J., Körschens, M., 2009. Calculating the Effect of Soil Organic Matter Concentration on Soil Bulk Density. Soil Science Society of America Journal 73(3), 876-885.

Schiettecatte, W., Gabriels, D., Cornelis, W.M., Hofman, G., 2008. Enrichment of organic carbon in sediment transport by interrill and rill erosion processes. Soil Science Society of America Journal 72(1), 50-55.

Shi, Z., Fang, N., Wu, F., Wang, L., Yue, B., Wu, G., 2012. Soil erosion processes and sediment sorting associated with transport mechanisms on steep slopes. Journal of Hydrology 454, 123-130.

Schumer, R., Meerschaert, M.M., Baeumer, B., 2009. Fractional advection-dispersion equations for modeling transport at the Earth surface. Journal of Geophysical Research: Earth Surface 114(F4).

Six, J., Paustian, K., Elliott, E.T., Combrink, C., 2000. Soil Structure and Organic Matter I. Distribution of Aggregate-Size Classes and Aggregate-Associated Carbon. Soil Science Society of America Journal 64(2), 681-689.

Stevens, C.J., Quinton, J.N., 2008. Investigating source areas of eroded sediments transported in concentrated overland flow using rare earth element tracers. Catena 74(1), 31-36.

Sutherland, R., Wan, Y., Lee, C.-T., Ziegler, A., 1996. Aggregate enrichment ratios for splash and wash transported sediment from an Oxisol. Catena 26(3-4), 187-208.

Szabó, J.A., Király, C., Karlik, M., Tóth, A., Szalai, Z., Jakab, G., 2020. Rare earth oxide tracking coupled with 3D soil surface modelling: an opportunity to study small-scale soil redistribution. Journal of Soils and Sediments, 1-13.

USEPA, 1996. Method 3050B Acid Digestion of Sediments, Sludges, and Soils 1.0 Scope and Application. Washington DC, USA.

Van Dijk, A., Bruijnzeel, L.A., Eisma, E.H., 2003. A methodology to study rain splash and wash processes under natural rainfall. Hydrological Processes 17(1), 153-167.

Van Dijk, A., Meesters, A., Bruijnzeel, L., 2002. Exponential distribution theory and the interpretation of splash detachment and transport experiments. Soil Science Society of America Journal 66(5), 1466-1474.

Wacha, K., Papanicolaou, A., Giannopoulos, C., Abban, B., Wilson, C., Zhou, S., Hatfield, J., Filley, T., Hou, T., 2018. The Role of Hydraulic Connectivity and Management on Soil Aggregate Size and Stability in the Clear Creek Watershed, Iowa. Geosciences 8(12), 470.

Wainwright, J., Parsons, A.J., Müller, E.N., Brazier, R.E., Powell, D.M., Fenti, B., 2008a. A transport-distance approach to scaling erosion rates: 1. Background and model development. Earth Surface Processes and Landforms 33(5), 813-826.

Wainwright, J., Parsons, A.J., Müller, E.N., Brazier, R.E., Powell, D.M., Fenti, B., 2008b. A transport-distance approach to scaling erosion rates: 2. Sensitivity and evaluation of MAHLERAN. Earth Surface Processes and Landforms: The Journal of the British Geomorphological Research Group 33(6), 962-984.

Yoo, K., Amundson, R., Heimsath, A.M., Dietrich, W.E., 2006. Spatial patterns of soil organic carbon on hillslopes: Integrating geomorphic processes and the biological C cycle. Geoderma 130(1-2), 47-65.

Zhang, J., Quine, T.A., Ni, S., Ge, F., 2006. Stocks and dynamics of SOC in relation to soil redistribution by water and tillage erosion. Global Change Biology 12(10), 1834-1841.

Zhang, Q., Lei, T., Zhao, J., 2008. Estimation of the detachment rate in eroding rills in flume experiments using an REE tracing method. Geoderma 147(1-2), 8-15.

Zhang, X., Friedrich, J., Nearing, M.A., Norton, L., 2001. Potential use of rare earth oxides as tracers for soil erosion and aggregation studies. Soil Science Society of America Journal 65(5), 1508-1515.

Zhang, X., Nearing, M., Polyakov, V., Friedrich, J., 2003. Using rare-earth oxide tracers for studying soil erosion dynamics. Soil Science Society of America Journal 67(1), 279-288.

Zhou, S., Wilson, C., Hathaway, J., In preparation. Tracking aggregate turnover in situ under raindrop impact and wetting-drying cycles using rare earth elements.

Zhu, M., Tan, S., Dang, H., Zhang, Q., 2011. Rare earth elements tracing the soil erosion processes on slope surface under natural rainfall. Journal of Environmental Radioactivity 102(12), 1078-1084.

CHAPTER SIX

CONCLUSIONS AND FUTURE WORK

Conclusions

This dissertation investigated the SOC spatial variability and soil redistribution in a low-gradient agricultural watershed in the Midwestern US as functions of topography, aggregate dynamics, transport selectivity, and transport distances of soil aggregates. The visible and near-infrared spectroscopy (Vis-NIR) and partial least squares regression (PLSR) were used to determine SOC concentrations, while a rare earth elements (REE) tracing approach was used to track the interactive breakdown and formation of four aggregate size fractions *in situ* under raindrop impact and weather-driven wetting-drying cycles. Then, simulated rainfall experiments were conducted on field plots to investigate the soil transport characteristics by surface runoff in terms of size selectivity and SOC enrichment in eroded sediments under various tillage and residue cover treatments. Finally, the REE tracing approach was used to assess the transport distances of each aggregate size fractions for the upper-, mid-, and toe-slopes by incorporating REE concentrations into existing diffusion and exponential models. The following is a summary of the major findings of the dissertation:

(1) In the higher-gradient landscape, lower SOC variability occurred vertically and laterally (unimodal, homogeneous) due to accelerated mass mobilization and mixing under high surface runoff. In contrast, SOC in the lower-gradient system had 25% higher concentrations and two times higher spatial variability (multimodal, heterogeneous) as more carbon accumulated in the local depressions than surrounding areas.

(2) A net breakdown occurred in the larger aggregate size fractions following an initial series of rain events due to raindrop impact, which led to a decreased amount of larger macroaggregates and increased amounts of small macroaggregates and fines. After a subsequent drying-wetting cycle, there was a net formation of extra-large and large macroaggregates due to increased particle binding by clay shrinkage upon drying and microbial activity flushes upon rewetting.

(3) The aggregate turnover times increased as the time frame increased from 3 days to 26 days (3-8 *vs.* 53-110 days). Over the entire experiment, small macroaggregates turned over most rapidly (0.019 day^{-1}), and extra-large macroaggregates and fines turned over most slowly (0.009 day^{-1}).

(4) Simulated rainfall-induced runoff from the field plots was within the laminar and subcritical flow regimes. The fine particles accounted for 97% of the total lost soil showing high size selectivity of aggregate transport in the low-gradient environment. The measured ER_{SOC} was in the range of 1.3-8.1, which increased as the total soil loss decreased.

(5) High amounts of residue cover (i.e., no-till with 65% corn residue) are best for reducing runoff erosive power and soil loss, by more than two orders of magnitude compared to those obtained with conventional tillage practices. While the no-till with low amounts of residue cover (i.e., no-till with 5% soybean residue) was the worst

alternative to control erosion, which produced 20% higher runoff and 7% higher soil loss than those under conventional tillage practices.

(6) In the upper slope, the REE concentration profiles were represented by the exponential model, with shorter transport distances of aggregates (0.97-1.46 cm). In the toe-slopes, the REE concentration profiles were described by the diffusion model with longer aggregate transport distances (15-117 cm).

(7) The transport distances at given slope positions varied with aggregate size. The longest distances of transport were found for small macroaggregates (1.33-117 cm) and the shortest transport distances existed in extra-large macroaggregates (0.97-36 cm).

Future Work

Based on the findings reported in this dissertation, the following recommendations are suggested for future work:

(1) The Vis-NIR technique was shown to save considerable time and labor when analyzing large numbers of soil samples to support watershed-scale SOC modeling or developing high-resolution SOC maps for field-scale precision farming. Future studies should refine this method and focus on the variability in the shapes of Vis-NIR spectra to better define relationships between site characteristics and dominant spectra spikes.

(2) SOC concentration varies across aggregate size fractions, which could be responsible for the varied turnover rates observed for different aggregate size fractions. This knowledge can be used to improve the design of modeling aggregate turnover and carbon cycling in different pools. Future work should tease out the cycling and turnover rates of aggregate associated SOC and how this process affects carbon budgets.

(3) The simulated rainfall experiments were confined to the low-gradient system where soil erosion is relatively mild compared to those in steep environments. Future studies should explore the effects of residue cover on selective transport of aggregates and erosion control in steep environments where erosion is inherently severe.

(4) The transport distances of all aggregate size fractions are generally short in the agricultural field over the monitored time period. Due to the relatively short experimental timeframe, we are not certain if any particles transported through the grass buffer strips and eventually entered the stream that was next to the field. Future study should explore the time for the applied material to travel into neighboring streams through rills and gullies, the impact of traveled sediments on water quality, and the upland-river connectivity. This would require longer-term studies that were not feasible in this project.

APPENDICES

Appendix A: Aggregate Turnover Model

This study tracked the mass flow out of X, L, and S fractions following six potential breakdown pathways (a-f) and the mass flow into X, L, and F fractions following six potential aggregation pathways (g-l; Figure C-3).

The transfers between time t_1 and t_2 can be described in a discrete transfer matrix $K_{(t_2-t_1)}$ according to Peng et al. 2017:

$$K_{(t_2-t_1)} = \begin{bmatrix} X \\ L \\ S \\ F \end{bmatrix} \tag{A-1}$$

$$K_{(t_2-t_1)} = \begin{bmatrix} 1-a-d-f & i & k & l \\ a & 1-i-b-e & h & j \\ d & b & 1-k-h-c & g \\ f & e & c & 1-l-j-g \end{bmatrix} \tag{A-2}$$

where a to l are the changes of proportions of aggregates (% of the initial mass of each aggregate fraction) falling into sizes X, L, S, and F between time t_1 and t_2; t_1 represents the initial time Day 0, t_2 represents Day 3 or Day 26.

The mass of aggregates in the plot at time t_1 and t_2 can be described by vectors $M_{AGG.(t_1)}$ and $M_{AGG.(t_2)}$:

$$M_{AGG.(t_1)} = \begin{bmatrix} X_{t_1} \\ L_{t_1} \\ S_{t_1} \\ F_{t_1} \end{bmatrix} \tag{A-3}$$

$$M_{AGG.(t_2)} = \begin{bmatrix} X_{t_2} \\ L_{t_2} \\ S_{t_2} \\ F_{t_2} \end{bmatrix} \tag{A-4}$$

where X, L, S, and F represent the mass of extra-large macroaggregates (8-19 mm), large macroaggregates (2-8 mm), small macroaggregates (0.075-2 mm), and fines (<0.075 mm), respectively. When the mass conservation of aggregates is assumed during transfer between time t_1 and t_2, their relationship can be described as follows:

$$M_{AGG.(t_2)} = K_{(t_2-t_1)} M_{AGG.(t_1)} \tag{A-5}$$

We assume that the four aggregate fractions were labeled homogeneously by different REEs, and there was no loss of REEs during the dry sieving, the transfer matrix $K_{(t_2-t_1)}$ in aggregates can be determined from the changes of REE mass between time

t_1 and t_2. First, the REE concentrations in different aggregate fractions at time t are presented as:

$$C_{REE(t)} = \begin{bmatrix} [Yb_X] & [Er_X] & [Gd_X] & [Sm_X] \\ [Yb_L] & [Er_L] & [Gd_L] & [Sm_L] \\ [Yb_S] & [Er_S] & [Gd_S] & [Sm_S] \\ [Yb_F] & [Er_F] & [Gd_F] & [Sm_F] \end{bmatrix} \quad \text{A-6}$$

where, e.g., $[Yb_X]$ is the concentration of Yb in extra-large macroaggregates. The mass of REEs in the four aggregate fractions are:

$$M_{REE(t)} = M_{AGG.(t)} C_{REE(t)} = \begin{bmatrix} X_t[Yb_X] & X_t[Er_X] & X_t[Gd_X] & X_t[Sm_X] \\ L_t[Yb_L] & L_t[Er_L] & L_t[Gd_L] & L_t[Sm_L] \\ S_t[Yb_S] & S_t[Er_S] & S_t[Gd_S] & S_t[Sm_S] \\ F_t[Yb_F] & F_t[Er_F] & F_t[Gd_F] & F_t[Sm_F] \end{bmatrix} \quad \text{A-7}$$

When the mass of REEs is assumed to follow the mass conservation during aggregate transfers, Eq. A-7 can be written as follows:

$$M_{REE(t_2)} = K_{(t_2-t_1)} M_{REE(t_1)} \quad \text{A-8}$$

Consequently, the transfer matrix $K_{(t_2-t_1)}$ can be calculated:

$$K_{(t_2-t_1)} = M_{REE(t_2)} M_{REE(t_1)}^{-1} \quad \text{A-9}$$

Since the soil is the mixture of four different aggregate fractions, aggregate transfer may happen during the recombination process at time t_1(Peng et al., 2017). Here, we assume that the aggregate transfer through recombination is negligible because the aggregates were recombined very gently.

In the aggregate breakdown (BD) direction, the changes in aggregate proportion of X, L, and S fractions during the experiment from time t_1 to t_2 are expressed as follows:

$$BD(X) = \left(a_{t_2} - a_{t_1}\right) + \left(d_{t_2} - d_{t_1}\right) + (f_{t_2} - f_{t_1}) \quad \text{A-10}$$

$$BD(L) = \left(b_{t_2} - b_{t_1}\right) + \left(e_{t_2} - e_{t_1}\right) \quad \text{A-11}$$

$$BD(S) = c_{t_2} - c_{t_1} \quad \text{A-12}$$

In the aggregate reformation (RF) direction, the changes in aggregate proportion of newly formed aggregates in X, L, and S fractions during the experiment from time t_1 to t_2 are expressed as follows:

$$RF(X) = \frac{(i_{t_2} - i_{t_1})L_{t_1} + (k_{t_2} - k_{t_1})S_{t_1} + (l_{t_2} - l_{t_1})F_{t_1}}{X_{t_1}} \quad \text{A-13}$$

$$RF(L) = \frac{(h_{t_2} - h_{t_1})S_{t_1} + (j_{t_2} - j_{t_1})F_{t_1}}{L_{t_1}} \quad \text{A-14}$$

$$RF(S) = \frac{(g_{t_2} - g_{t_1})F_{t_1}}{S_{t_1}} \quad \text{A-15}$$

In the aggregate breakdown direction, if BD>0, this fraction undergoes a destabilization process over time; if BD<0, this fraction undergoes a stabilization process time. In the aggregate formation process, RF is always greater than 0. The F fraction (<0.075 mm) could not be considered in the aggregate breakdown and formation processes given that no fractions smaller than F were investigated in this study.

The turnover rate (TR, day^{-1}) of each aggregate fraction during the experiment from time t_1 to t_2 is expressed as following:

$$TR(X) = \frac{|a_{t_1} + d_{t_1} + f_{t_1} - (a_{t_2} + d_{t_2} + f_{t_2})|}{t_2 - t_1} \quad \text{A-16}$$

$$TR(L) = \frac{|i_{t_1} + b_{t_1} + e_{t_1} - (i_{t_2} + b_{t_2} + e_{t_2})|}{t_2 - t_1} \quad \text{A-17}$$

$$TR(S) = \frac{|k_{t_1} + h_{t_1} + c_{t_1} - (k_{t_2} + h_{t_2} + c_{t_2})|}{t_2 - t_1} \quad \text{A-18}$$

$$TR(F) = \frac{|l_{t_1} + j_{t_1} + g_{t_1} - (l_{t_2} + j_{t_2} + g_{t_2})|}{t_2 - t_1} \quad \text{A-19}$$

The turnover time of each aggregate fraction is the reciprocal of its turnover rate.

To test the efficacy of REEs as tracers for aggregate transfer, the mass of each aggregate fraction was predicted using Eq. A-7.

Appendix B: Tables

Table B-1. Rainfall events and their characteristics over the study period.

Event	Date	Exp. time (d)	Duration (h)	Rainfall amount (mm)	Max. intensity (mm h^{-1})	Corn cover (%)	Max. rain power (W m^{-2})
R1	5/29	0	4.00	9.91	18.29	0.00	0.020
R2	5/30	1	1.00	1.78	3.05	0.57	0.003
R3	5/31	2	1.00	2.54	6.10	1.46	0.006
R4	6/12	14	5.25	19.05	34.56	20.78	0.033
R5	6/13	15	0.25	0.25	1.02	22.83	0.001
R6	6/19	21	3.75	13.46	12.19	36.13	0.008
R7	6/20	22	1.25	4.83	8.13	38.50	0.005
R8	6/22	24	1.25	1.52	2.03	43.36	0.001
R9	6/23	25	0.75	3.81	11.18	45.84	0.006
R10	6/24	26	0.75	1.52	4.06	48.36	0.002

Table B-2. Mass of REEs inside the tagged source plot and its downslope untagged area on Day 0 and Day 26 and its net changes between Day 0 and Day 26.

REE	Tagged source (g)		Loss from source (g)	Untagged downslope (g)
	D0	D26	D0-D26	D26
Yb	191	113	78	75
Er	311	158	154	176
Gd	91	49	42	30
Sm	11	5	6	41

Appendix C: Figures

Figure C-1. (a) Front view of the rainfall simulator setup for the aggregate stability tests; (b) the retained, (c) wet slaked, and (d) dry slaked material after simulated rainfall on the aggregate samples.

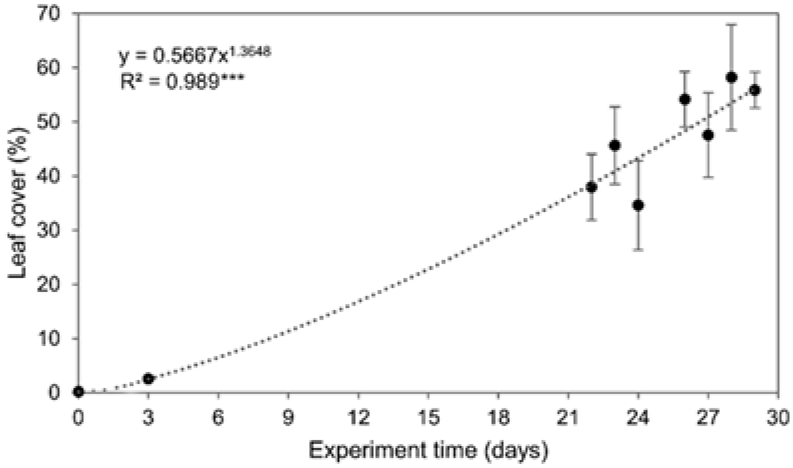

Figure C-2. The relationship between the experiment days and the proportion of the plot surface covered by corn plants.

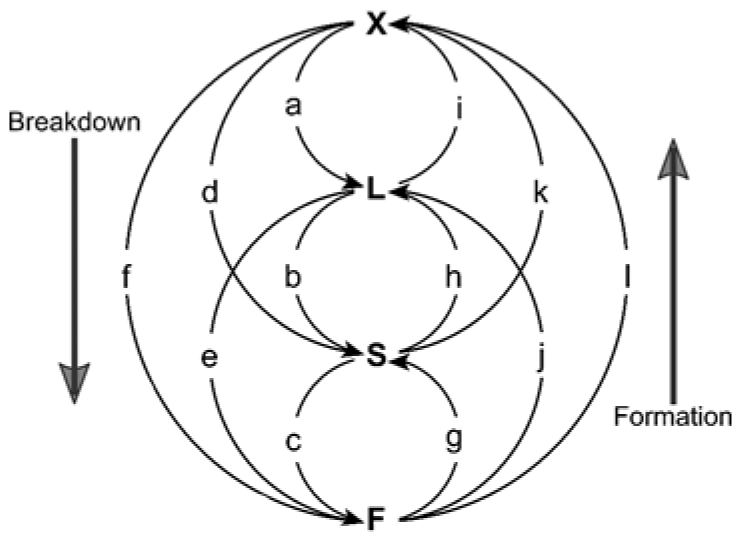

Figure C-3. The 12 possible transfer pathways among four different aggregate size fractions. a-f denotes aggregate breakdown directions, g-l denotes aggregate formation directions. X, L, S, and F indicate aggregates in 8-19 mm, 2-8 mm, 0.075-2 mm, and <0.075 mm, respectively.

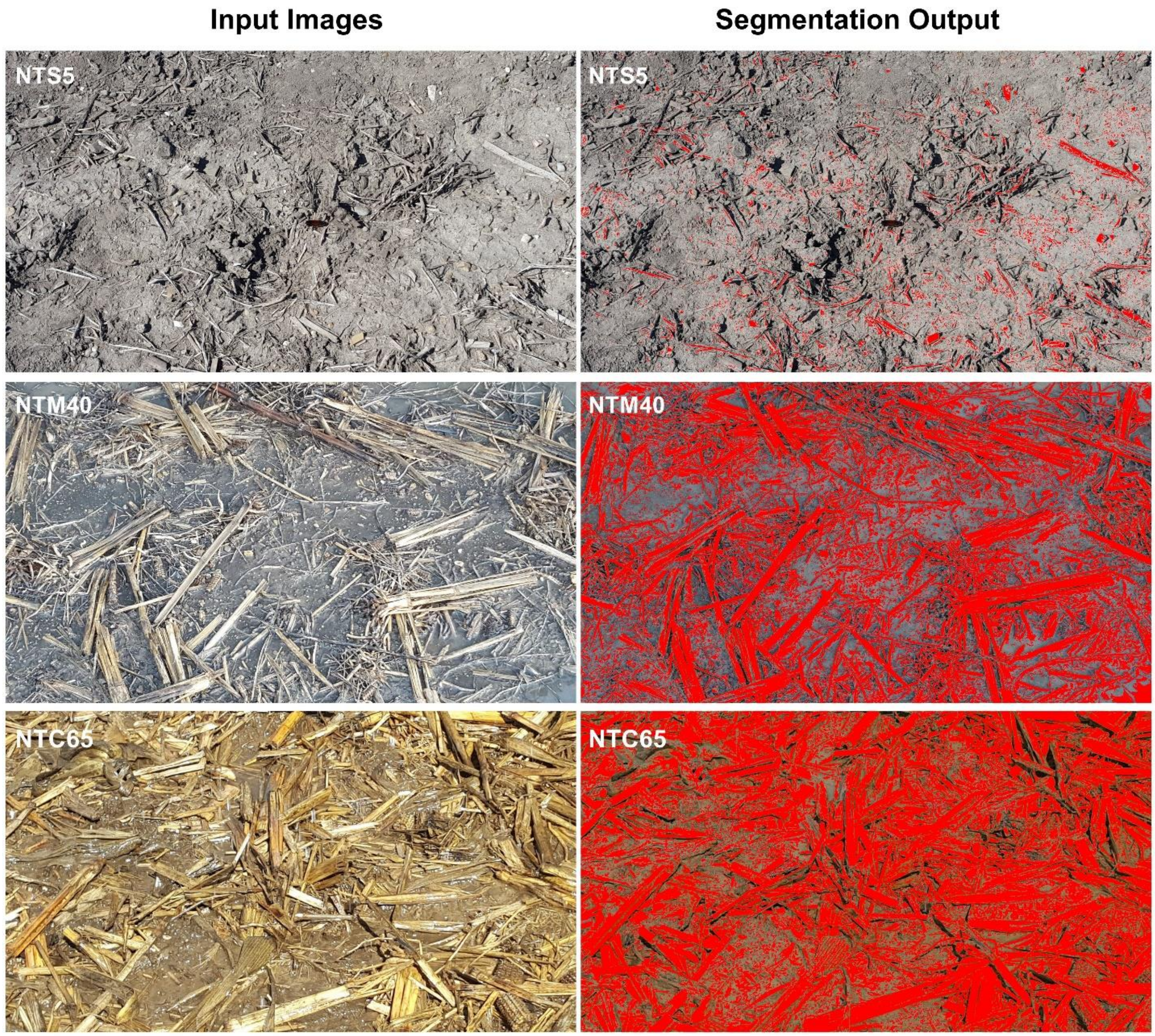

Figure C-4. Segmentation of residue cover for the no-till plots using the ImageJ software. The red color denotes the identified crop residues.

VITA

Shengnan Zhou, a Ph.D. student in the Department of Civil and Environmental Engineering at the University of Tennessee, Knoxville, studied Geographic Sciences at Hubei Normal University from 2009 to 2013. She received her Master of Science degree from the Institute of Applied Ecology, Chinese Academy of Sciences in 2016. Afterwards, she worked as a research assistant in her master research group (Landscape Process Group) for six months. In December 2016, Ms. Zhou traveled to the United States to pursue her doctoral degree after earning the China-UT EcoPatnership Scholarship funded by the China Scholarship Council. Her current research focuses on understanding underlying physical processes of aggregates dynamics, aggregate transport, and carbon redistribution across scales of the agricultural landscapes.